University of California
Santa Barbara

Search for new physics with a same-sign dilepton pair at a center-of-mass energy of 13 TeV at the CMS detector

A dissertation submitted in partial satisfaction
of the requirements for the degree

Doctor of Philosophy
in
Physics

by

Christopher Alexandre George

Committee in charge:

Professor Claudio Campagnari, Chair
Professor David Stuart
Professor Mark Srednicki

June 2016

The Dissertation of Christopher Alexandre George is approved.

Professor David Stuart

Professor Mark Srednicki

Professor Claudio Campagnari, Committee Chair

June 2016

Search for new physics with a same-sign dilepton pair at a center-of-mass energy of 13 TeV at the CMS detector

by

Christopher Alexandre George

This dissertation is dedicated to the memory of Grandma Bukie.

1924-2011

Acknowledgements

I would like to acknowledge my dissertation advisor, Prof. Claudio Campagnari, for his mentorship and help with the physics aspects of my work for the past six years. I always felt like I won the grad school lottery with my admission to UCSB and opportunity to work with Claudio.

I would also like to thank Prof. Frank Würthwein for his help with my computing work in our research group. I similarly extend my thanks to Prof. Avi Yagil for faithfully attending the same-sign meetings for several years. Further, I am grateful to Prof. David Stuart and Prof. Mark Srednicki for serving on my committee.

My thanks also go to Dr. Frank Golf and Dr. Giuseppe Cerati for their friendship and help; I am impressed in equal measure by Giuseppe's extreme calmness and Golf's lack thereof.

I would like to acknowledge Jason Gran, Nick Amin, Ben LaRoque, Sicheng Wang, Bennett Marsh, Dr. Indara Suárez, Dr. Guido Magazzù, Dr. Derek Barge, Dr. Ricardo Magaña, Dr. Verena Martinez, and Dr. Tom Danielson. I already miss working with this great collection of people.

In particular, I thank Claudio Campagnari, Rheanna George, and Sicheng Wang for reading and providing thoughtful comments and many corrections for this manuscript.

Finally, I would like to thank my parents, grandparents, and beautiful wife for their support during this long process.

Curriculum Vitæ

Christopher Alexandre George

Education

2016 Ph.D. (expected), Physics, University of California, Santa Barbara

2010 B.S. *magna cum laude*, Physics and Mathematics, University of Pittsburgh

Selected Publications

CMS Collaboration. **Search for new physics in same-sign dilepton events in proton-proton collisions at sqrt(s)=13 TeV**. To be published in *European Physics Journal C* in Spring 2016.

CMS Collaboration. **Search for new physics in events with same-sign dileptons and jets in pp collisions at sqrt(s)=8 TeV**. Journal of High Energy Physics 01 (2014) 163.

CMS Collaboration. **Search for direct top squark pair production in the single lepton channel with transverse mass at 8 TeV**. European Physics Journal 73 (2013) 2677.

MINERvA Collaboration. **Design, Calibration, and Performance of the MINERvA Detector**. Nuclear Instruments and Methods A743 (2014) 130-159.

Abstract

Search for new physics with a same-sign dilepton pair at a center-of-mass energy of 13 TeV at the CMS detector

by

Christopher Alexandre George

An inclusive search for new physics is performed with a 13 TeV dataset from the CMS detector (May-November 2015, corresponding to 2.32 fb^{-1}) using events with at least two leptons with the same electrical charge, missing transverse energy, and significant hadronic activity. No significant excesses are reported above the Standard Model background predictions. Constraints are set on a number of new physics models. As motivation, a thorough pedagogical review of the Standard Model and its shortcomings is presented in the first two chapters.

Contents

Chapter 1

The Standard Model

The universe and everything in it – as far as we know – is made up of sixty-one elementary particles that interact through four distinct forces. The Standard Model (SM) attempts to mathematically describe the nature of these particles and their interactions. In principle, the SM explains all known phenomena; however, there are some serious shortcomings (for example, only three of the four forces are accounted for). The first chapter of this dissertation will describe the SM in considerable detail at a level appropriate for a reader who has completed an undergraduate physics degree; the second chapter will then turn to the shortcomings of this model and the need for future research.

We will begin by stating a set of axioms – experimental results – from which we can mathematically derive the Lagrangian for the SM. We will then proceed carefully through this derivation. Once we have the Lagrangian, we can draw diagrams of all allowed processes, and physical quantities such as cross-sections and decay rates can be predicted. We will then conclude the chapter by discussing the experimental validation of these predictions.

1.1 Axioms to construct the SM

We will begin by accepting the experimental evidence for the existence of the 48 (spin-$\frac{1}{2}$) fermions.[1] These include the 12 leptons (electron, muon, tau, electron neutrino, muon neutrino, and tau neutrino, and the corresponding antileptons) and the 36 quarks (up, down, charm, strange, top, bottom, each in three colors, and their corresponding antiparticles). We will similarly accept the evidence for the 13 bosons: 8 gluons, the photon, and the W^+, W^-, Z, and Higgs particles.[2]

Second, we will accept the premise of quantum field theory, that each particle is a manifestation of a corresponding field that obeys commutation operators (fermions) or anticommutation operators (bosons). We will therefore construct a Lagrangian ($\mathcal{L}$) written in terms of fields: these fields will have the same name as the particle (for example, h refers to the Higgs field). The details of this Lagrangian will completely and uniquely specify the properties of every particle and so also of the Standard Model.

As we will show, the SM Lagrangian will have two types of terms: kinetic terms, which describe the behavior of free particles, and interaction terms. The kinetic terms require free particles to follow their characteristic equation of motion. As a third axiom, we will accept the equations of motion as follows[3]:

- Bosons obey the Klein-Gordon Equation.
- Fermions obey the Dirac Equation.

[1] This experimental evidence is presented in great detail elsewhere, see for example [1].

[2] It is not strictly necessary to assume the existence of these particles – they are a prediction, not an input – but it is perhaps disingenous to claim that the Standard Model could have been developed and accepted as correct with no knowledge of these particles.

[3] This is entirely analogous to requiring all particles to follow the Schrödinger Equation in quantum mechanics

Fourth, we accept the experimental results for allowed, suppressed, and forbidden weak processes. In particular, this means accepting parity-violation in the weak sector: weak interactions affect left-handed particles (handedness refers to chirality, the projection of a particle's spin onto the momentum axis in the limit $v \to c$) far more than right-handed particles. For example, in the decay of cobalt ($^{60}\mathrm{Co} \to\ ^{60}\mathrm{Ni} + e^- + \bar{\nu}_e$), the electrons are preferentially emitted with a right-handedness. Similarly, experimental results indicate that all neutrinos are left-handed and all anti-neutrinos are right-handed.[4] Further, this preference is absolute (maximal violation: weak processes affect only left-handed particles) in some processes, but not in others.

Our fifth axiom is that the resulting Lagrangian must be invariant under the transformations $q \to SO3(x)q$, $f^L \to SU2(x)f^L$, and $c \to e^{i\theta(x)}c$, where q is any quark (represented as a 3-vector of the three colors), f^L is any left-handed fermion (represented as a spinor), and c is any charged particle. Further, SO3(x) refers to any 3x3 matrix in an orthonormal basis with determinant 1, SU2(x) refers to any unitary 2x2 matrix in an orthonormal basis with determinant 1, and $\theta(x)$ is any arbitrary function of x (multiplied by an identity matrix of the appropriate dimension, if necessary). Note that these matrices and functions may depend on the position vector. This axiom can be summarized by saying that the SM must be locally gauge invariant under a transformation of the form SU(3) $\times$ SU(2)$_L\times$ U(1). It is from this requirement that most of the familiar behavior of the strong, electromagnetic, and weak forces can be derived.

Sixth, we will accept the experimentally-accepted measurements for the mass of each particle. The one exception to this is the neutrino mass, which we will assume to be

[4]It is curious that this observation persists even though the neutrino mass is now known to be nonzero.

massless despite the experimental results; we will discuss this in section 2.1.

1.2 Quantum Chromodynamics

Global U(3) Symmetry

Quarks are fermions, so our third axiom tells us that a free quark must obey the Dirac equation. Thus, a particular free quark may have a Lagrangian of the form:

$$\mathcal{L}_Q = i\bar{q}_r\gamma^\mu\partial_\mu q_r - m_q\bar{q}_r q_r \tag{1.1}$$

where q_r is the quark *field* – a Dirac spinor in this case (r represents the color – we have arbitrarily chosen this particular quark to be red). We have not specified the flavor (top, bottom, etc.) but any flavor will do – in fact, we will use a convention similar to index notation in which terms involving q are assumed to be summed over all six flavors. In this way, equation (1.1) is sufficient for all 12 red quarks and antiquarks.

Each quark comes in one of three colors, so we can write one Lagrangian that accounts for all three colors of a particular quark flavor as follows:

$$\mathcal{L}_Q = i\bar{q}_r\gamma^\mu\partial_\mu q_r - m_q\bar{q}_r q_r + i\bar{q}_b\gamma^\mu\partial_\mu q_b - m_q\bar{q}_b q_b + i\bar{q}_g\gamma^\mu\partial_\mu q_g - m_q\bar{q}_g q_g \tag{1.2}$$

This notation is not convenient, so we define a vector of Dirac spinors:

$$q = \begin{pmatrix} q_r \\ q_b \\ q_g \end{pmatrix} \tag{1.3}$$

In this way, we can write the full Lagrangian for all 36 quarks as:

$$\mathcal{L}_Q = i\bar{q}\gamma^\mu \partial_\mu q - m_q \bar{q} q \tag{1.4}$$

Notice that this admits a global gauge symmetry: it is manifestly invariant under the transformation given by:

$$q \to Uq \tag{1.5}$$

where U is any unitary 3x3 matrix (this is dubbed a "global U(3) symmetry").

Group theory tells us that we can write any unitary matrix as $U = e^{iH}$, where H is an Hermitian matrix.[5] Further, a (complex) 3x3 Hermitian matrix has only nine degrees of freedom, and so there exists some basis of 9 orthonormal 3x3 matrices in which H can be decomposed. It can be shown[6] that $H = I\theta + \vec{\lambda} \cdot \vec{a}$, where $\vec{\lambda}$ is the vector of Gell-Mann matrices, and a is a vector of real numbers, is a valid choice. Putting all this together, we can write:

$$U = e^{i\theta} e^{i\vec{\lambda}\cdot\vec{a}} \tag{1.6}$$

Now we have two exponentials, which allows us to factorize the global symmetries to U(1) and SU(3).[7] Our axioms, however, require chromodynamics to be invariant under *local* symmetries: the next step is therefore to insist that these global symmetries be held locally. We will handle these one at a time, beginning with U(1).

[5] See for example Chevalley, C. *Theory of Lie Groups*, Princeton: Princeton University Press, 1946.

[6] by explicit calculation, see for example problem 10.16 of [1]

[7] You may be concerned that our SU(2) symmetry is nowhere to be found. Don't be – here we consider only QCD; the SU(2) symmetry arises when we consider our quarks interacting via the electroweak force.

Local U(1) symmetry

Imposing the local U(1) symmetry means requiring that our Lagrangian (equation (1.4)) be invariant under a transformation of the form:

$$q \to e^{-iQ\alpha(x)}q \tag{1.7}$$

where Q is a scalar and $\alpha(x)$ is a scalar function. Doing exactly this at first order, equation (1.4) becomes:

$$\mathcal{L}_Q = i\bar{q}\gamma^\mu\partial_\mu q - m\bar{q}q + Q\bar{q}\gamma^\mu q\partial_\mu\alpha \tag{1.8}$$

This is unacceptable: the Lagrangian is manifestly *not* invariant under this local gauge transformation, and so violates our axiom. The problem is this new term that includes a derivative acting on $\alpha(x)$. Our only recourse is to add a new term to the proposed Lagrangian that will cancel this problematic derivative. In particular, we'll choose to add the term $-Q\bar{q}\gamma^\mu q A_\mu$, where A_μ represents a new, spin-1 field with the following local gauge transformation:

$$A_\mu \to A_\mu + \partial_\mu\alpha(x) \tag{1.9}$$

After adding this term, our Lagrangian becomes:

$$\mathcal{L}_Q = i\bar{q}\gamma^\mu\partial_\mu q - m\bar{q}q - Q\bar{q}\gamma^\mu q A_\mu \tag{1.10}$$

Repeating our test, we find that this Lagrangian is now invariant under a local U(1) gauge transformations: the derivative term is generated as previously, but this is cancelled by the new term generated from the transformation of A^μ. The cost is that we've added a new field (A_μ).

This new field must itself satisfy the Klein-Gordon equation, so we must add terms to the Lagrangian that facilitate this. Our result is that:

$$\mathcal{L} = i\bar{q}\gamma^{\mu}\partial_{\mu}q - m_q\bar{q}q - Q\bar{q}\gamma^{\mu}qA_{\mu} - \frac{1}{4}F^{\mu\nu}F_{\mu\nu} + m_A^2A^{\nu}A_{\nu} \tag{1.11}$$

where

$$F^{\mu\nu} = \partial^{\mu}A^{\nu} - \partial^{\nu}A^{\mu} \tag{1.12}$$

Now we have added two new terms to the Lagrangian, and we must verify that these two new terms do not spoil our local gauge invariance. As before, we apply equations (1.7) and (1.9) to the Lagrangian. The result is that the first four terms remain unchanged under this transformation, but the mass term ($m_AA^{\mu}A_{\mu}$) does not. We therefore simply set $m_A = 0$, and arrive at our full quark Lagrangian that respects a local U(1) symmetry. We will label this as $\mathcal{L}_{QCD}^{U1}$.

$$\mathcal{L}_{QCD}^{U1} = i\bar{q}\gamma^{\mu}\partial_{\mu}q - m\bar{q}q - Q\bar{q}\gamma^{\mu}qA_{\mu} - \frac{1}{4}F^{\mu\nu}F_{\mu\nu} \tag{1.13}$$

How should we physically interpret the A_{μ} field? Our second axiom tells us that this field is a particle – a boson, since we chose it to have spin-1, and apparently a massless one. Further, this particle seems to interact with the quarks, as the third term of equation (1.13) involves $\bar{q}qA_{\mu}$, but not with itself, since there are no terms in (1.13) involving more than two factors of A_{μ}. This describes perfectly the photon. Therefore, we interpret A_{μ} as the photon and Q (the coupling constant) as the electric charge. Indeed, A_{μ} can be interpreted as the quantum analog of the electromagnetic 4-potential.[8]

[8]The procedure for expressing A_{μ} as a solution of the Klein-Gordon equation and quantizing the field is beyond the scope of this dissertation; a good and reasonably modular treatment is given in chapter 55 of [3].

Local SU(3) symmetry

Now back to equation (1.4). This time we want to impose the local SU(3) symmetry, which means that we must require our Lagrangian to be invariant under a transformation of the form:

$$q \to e^{-ig_s\vec{\lambda}\cdot\vec{a}(x)}q \tag{1.14}$$

where λ are the Gell-Mann matrices. To avoid complications inherent with the matrix exponential, we shall expand and keep only the first-order terms.[9]

$$q \to q - ig_s\vec{\lambda}\cdot\vec{a}(x)q \tag{1.15}$$

Applying this transformation to equation (1.4) and dropping the terms higher than first order in $\vec{a}(x)$ leads us to the following:

$$\mathcal{L}_Q = i\bar{q}\gamma^\mu\partial_\mu q - m_q\left(\bar{q} + ig_s\bar{q}\vec{\lambda}\cdot\vec{a}(x)\right)\left(q - ig_s\vec{\lambda}\cdot\vec{a}(x)q\right) + g_s\bar{q}\gamma^\mu\partial_\mu\left(\vec{\lambda}\cdot\vec{a}(x)\right)q \tag{1.16}$$

Just as in the U(1) case, this shows that our Lagrangian is not invariant under this local transformation, which is unacceptable. We must therefore set $m_q = 0$. With our mass terms removed, our theory predicts massless quarks! This is of course a serious problem (in fact, it violates our sixth axiom!), but we will proceed without the mass terms for the moment, hoping to solve the problem later.

[9] This induces no (further) loss of generality – recall that the kinetic terms for each particle assume that the particle follows its free-field equation. This assumption is only valid in the limit where the couplings are relatively weak. We can therefore view the coupling as a perturbation around the vacuum.

Without the mass term, our transformed Lagrangian is:

$$\mathcal{L}_Q = i\bar{q}\gamma^\mu\partial_\mu q + g_s\bar{q}\gamma^\mu\partial_\mu\left(\vec{\lambda}\cdot\vec{a}(x)\right)q \tag{1.17}$$

This still has an extra term (the second one). In fact, the extra term in this case involves the dot product of two eight-dimensional vectors ($\vec{\lambda}\cdot\vec{a}(x)$), so there are in fact eight extra terms in this transformed Lagrangian! As in the U(1) case, our recourse is to add another term (technically, another eight terms) to equation (1.4). Specifically, we will chooose to rewrite equation (1.4) as:

$$\mathcal{L}_Q = i\bar{q}\gamma^\mu\partial_\mu q + g_s\bar{q}\gamma^\mu\left(\vec{\lambda}\cdot\vec{G}_\mu\right)q \tag{1.18}$$

As before, by adding this new term, we are predicting a new spin-1 particle G^μ – in fact, this time we have added a vector of eight new particles. Proceeding in analogy to the U(1) case, we postulate that our Lagrangian will be invariant if the a^{th} particle G^a_μ transforms as follows:

$$G^a_\mu \to G^a_\mu - \frac{1}{g_s}\partial_\mu a^a(x) \tag{1.19}$$

To summarize, we have rewritten equation (1.4) as (1.18), which we claim will be invariant under local gauge transformations given by (1.15) and (1.19). Now we must verify that this works out. The transformation gives us:

$$\begin{aligned} &i\bar{q}\gamma^\mu\partial_\mu q + \bar{q}\gamma^\mu\left(\vec{\lambda}\cdot\vec{G}_\mu\right)q \to i\left[\bar{q} - i(\vec{\lambda}\cdot\vec{a})\bar{q}\right]\gamma^\mu\partial_\mu\left[q + i(\vec{\lambda}\cdot\vec{a})q\right] \\ &+g_s\left[\bar{q} - i\vec{\lambda}\cdot\vec{a}(x)\bar{q}\right]\gamma^\mu\left[\vec{\lambda}\cdot\left(\vec{G}_\mu - \frac{1}{g_s}\partial_\mu\vec{a}(x)\right)\right]\left[q + i(\vec{\lambda}\cdot\vec{a}(x))q\right] \end{aligned} \tag{1.20}$$

Multiplying this out, and discarding terms higher than first order, we are left with:

$$\mathcal{L}_Q \to \mathcal{L}_Q + ig_s G^a a^b \bar{q}\gamma^\mu q(\lambda^a\lambda^b - \lambda^b\lambda^a) \tag{1.21}$$

Using the commutator for Gell-Mann matrices, we can rewrite this as:

$$\mathcal{L}_Q \to \mathcal{L}_Q - f^{abc} g_s G^a a^b \bar{q}\gamma^\mu q\lambda^c \tag{1.22}$$

So $\mathcal{L}_Q$ is still not invariant! Apparently equation (1.19) (which we wrote in analogy with QED) is not sufficient; QCD requires an additional term because it is non-Abelian. We therefore rewrite our gluon transformation law as:

$$G^a_\mu \to G^a_\mu - \frac{1}{g_s}\partial_\mu a^a(x) + f^{abc} G^a_\mu a^b(x)\lambda^c \tag{1.23}$$

Now equation (1.22) is locally gauge invariant. However, we must add the kinetic terms for these new particles that we have introduced. Our final QCD Lagrangian is therefore:

$$\boxed{\mathcal{L}^{SU3}_{QCD} = i\bar{q}\gamma^\mu\partial_\mu q - g_s\bar{q}\gamma^\mu\left(\vec{\lambda}\cdot\vec{G}_\mu\right)q - \frac{1}{4}G^a_{\mu\nu}G^{\mu\nu}_a} \tag{1.24}$$

with

$$G^a_{\mu\nu} = \partial_\mu G^a_\nu - \partial_\nu G^a_\mu - g_s f^{abc} G^b_\mu G^c_\nu \tag{1.25}$$

The form of (1.25) arose by requiring the new spin-1 gauge bosons G^a_μ to follow the Klein-Gordon equation.[10]

We now have the correct Lagrangian, but perhaps not much physical intuition. To

[10]This is shown by simply evaluating the Euler-Lagrange equation for the G^a_μ fields. This can be done explicitly by taking a lot of partial derivatives, or by considering the group algebra. For the latter approach, see the solution to problem 14.10 in [2].

that end, let us now expand the second term of equation (1.24):

$$\begin{aligned}\mathcal{L}_{QCD} &= i\bar{q}\gamma^\mu\partial_\mu q - \tfrac{1}{4}G^a_{\mu\nu}G^{\mu\nu}_a \\ &\quad -g_s\gamma^\mu \begin{pmatrix} \bar{q}_r & \bar{q}_b & \bar{q}_g \end{pmatrix} \begin{pmatrix} G^3_\mu + \frac{1}{\sqrt{3}}G^8_\mu & G^1_\mu - iG^2_\mu & G^4_\mu - iG^5_\mu \\ G^1_\mu + iG^2_\mu & -G^3_\mu + \frac{1}{\sqrt{3}}G^8_\mu & G^6_\mu - iG^7_\mu \\ G^4_\mu + iG^5_\mu & G^6_\mu + iG^7_\mu & -\frac{2}{\sqrt{3}}G^8_\mu \end{pmatrix} \begin{pmatrix} q_r \\ q_b \\ q_g \end{pmatrix}\end{aligned}$$

Doing the matrix multiplication:

$$\begin{aligned}\mathcal{L}_{QCD} &= i\bar{q}\partial_\mu q - \tfrac{1}{4}G^a_{\mu\nu}G^{\mu\nu}_a \\ &\quad -g_s\gamma^\mu(G^3_\mu + \tfrac{1}{\sqrt{3}}G^8_\mu)\bar{q}_r q_r + -g_s\gamma^\mu(G^1_\mu - iG^2_\mu)\bar{q}_r q_b - g_s\gamma^\mu\bar{q}_r(G^4_\mu - iG^5_\mu)q_g \\ &\quad -g_s\gamma^\mu\bar{q}_b(G^1_\mu + iG^2_\mu)q_r - g_s\gamma^\mu\bar{q}_b(-G^3_\mu + \tfrac{1}{\sqrt{3}}G^8_\mu)q_b - g_s\gamma^\mu\bar{q}_b(G^6_\mu - iG^7_\mu)q_g \\ &\quad -g_s\gamma^\mu\bar{q}_g(G^4_\mu + iG^5_\mu)q_r - g_s\gamma^\mu\bar{q}_b(G^6_\mu + iG^7_\mu)q_g + g_s\gamma^\mu\bar{q}_g(\tfrac{2}{\sqrt{3}}G^8_\mu)q_g\end{aligned}$$

Notice that all eight of the gluons carry one unit of color and one unit of anticolor. Further, each gluon is a superposition of color-anticolor pairings. The exact assignment of gluons to superpositions will vary depending on the representation of the Gell-Mann matrices, but the physical result is the same.

Finally, let us expand out the second term of this equation and simplify slightly.[11]

$$\begin{aligned}
\mathcal{L}_{QCD}^{SU3} &= i\bar{q}\gamma^\mu\partial_\mu q - \tfrac{1}{4}(\partial^\mu G^\nu - \partial^\nu G^\mu)(\partial_\mu G_\nu - \partial_\nu G_\mu) + \tfrac{1}{2}g f_{abc} G_b^\mu G_c^\nu \partial_\mu G_\nu \\
&\quad -\tfrac{1}{2}g f_{abc} G_b^\mu G_c^\nu \partial_\nu G_\mu - \tfrac{1}{4}g^2 f_{abc} G_b^\mu G_c^\nu f_{ade} G_d^\mu G_e^\nu \\
&\quad -g_s\gamma^\mu(G_\mu^3 + \tfrac{1}{\sqrt{3}}G_\mu^8)\bar{q}_r q_r + -g_s\gamma^\mu(G_\mu^1 - iG_\mu^2)\bar{q}_r q_b - g_s\gamma^\mu\bar{q}_r(G_\mu^4 - iG_\mu^5)q_g \\
&\quad -g_s\gamma^\mu\bar{q}_b(G_\mu^1 + iG_\mu^2)q_r - g_s\gamma^\mu\bar{q}_b(-G_\mu^3 + \tfrac{1}{\sqrt{3}}G_\mu^8)q_b - g_s\gamma^\mu\bar{q}_b(G_\mu^6 - iG_\mu^7)q_g \\
&\quad -g_s\gamma^\mu\bar{q}_g(G_\mu^4 + iG_\mu^5)q_r - g_s\gamma^\mu\bar{q}_b(G_\mu^6 + iG_\mu^7)q_g + g_s\gamma^\mu\bar{q}_g(\tfrac{2}{\sqrt{3}}G_\mu^8)q_g
\end{aligned} \tag{1.26}$$

The first two terms are the usual kinetic terms for the quarks and gluons, respectively, and the last three lines show the allowed quark-gluon couplings. However, the third and fourth terms represent a tri-gluon interactions, while the fifth term represents a four-gluon interaction (a so-called glueball). Notice that if $f^{abc} = 0$, then these gluon-gluon interactions vanish; it is thus the non-Abelian nature of the gluon gauge transformation law (required to get the local gauge invariance to work out) that leads to the gluon-gluon interactions.

The last step would be to expand the terms of f^{abc} in order to explicitly identify the gluon combinations permitted in the three-gluon and four-gluon interactions. However, we will not perform this step – since there are 8 types of gluons, there would be $8^3 = 512$ different terms in the expansion of the three-gluon interaction and 32,768 terms in the expansion of the four-gluon vertex! Fortunately, this is not necessary; we can read off the allowed interactions from the Lagrangian as written. For example, $f^{147} = 1/2$, so the four-gluon vertex is given by $\frac{g^2}{8}G_4^\mu G_7^\nu G_\mu^4 G_\nu^7$, but all permutations of f^{aab} are zero, so no gluon can appear more than once in the three-gluon vertex or more than twice in the

[11] The two boxed results in this section are fully equivalent. The first emphasizes the Gauge-Invariance, while the second explicitely shows the behavior of the particles involved. We will discuss how to "read" the more verbose version shortly.

four-gluon vertex.

QCD Lagrangian

Recall that we broke our SO(3) symmetry into two parts: the U(1) symmetry and the SU(3) symmetry, and we derived an acceptable Lagrangian for each. It turned out that our SU(3) Lagrangian explained the strong force, while the U(1) Lagrangian explained the electromagnetic force as applied to quarks. For the strong force, we are done; equation (1.26) will appear in the final Lagrangian. As for equation (1.13), this is fully correct for the quarks, but we will later be able to recognize this equation as a special case of a more general result that applies to all charged particles. We turn to this now.

1.3 Electroweak Interactions

Electromagnetic Charge Current

Recall that a free quark (of any flavor) must follow the Dirac Equation in a vacuum:

$$(\gamma_\mu p^\mu - m)q_i = 0 \tag{1.27}$$

As already discussed, we have taken all our fermions to be massless in order to preserve the Gauge Invariance. Thus,

$$\gamma_\mu p^\mu q_i = 0 \tag{1.28}$$

Let us now consider this quark in a classical electromagnetic field. How does our Dirac equation change? The classical Lagrangian for the quark-field interaction is given by $\mathcal{L} \sim q\partial_\mu q_i A^\mu$, where A^μ is the classical 4-potential. Taking the canonical momentum, we find that $p^\mu = \frac{\partial \mathcal{L}}{\partial(\partial_\mu q_i)} = qA^\mu$. Therefore, our expression for the Dirac eqation remains valid in a nonzero classical electromagnetic field if we make the substitution $p^\mu \to p^\mu + qA^\mu$.

Thus, our Dirac Equation becomes:

$$(i\gamma^\mu \partial_\mu + q\gamma^\mu A_\mu)q_i = 0$$

This is:

$$i\gamma^\mu \partial_\mu q_i = -q\gamma^\mu A_\mu q_i$$

Analogously to the Schrödinger Equation, we can then interpret $-q\gamma^\mu A_\mu$ as a potential energy.

Now remember that there is no reason to expect a non-free Fermion to obey the Dirac Equation. Our work above is therefore valid only in the perturbative limit of weak coupling. For that matter, we can interpret the electromagnetic potential energy as a perturbation around the vacuum, and use the formula for the transition amplitude between two states:

$$\begin{aligned} T_{fi} &= -i\int (q_i)^\dagger_f(x)V(x)q_i(x)d^4x \\ &= iq\int \bar{q}_f\gamma_\mu A^\mu q_i d^4x \\ &= -iq\int j_\mu A^\mu d^4x \end{aligned} \tag{1.29}$$

We define

$$j^{EM}_\mu = -\bar{q}_i\gamma_\mu q_i \tag{1.30}$$

We interpret j_μ as the electromagnetic transition current. Further, it is easy to show that $\partial_\mu j^\mu = 0$, so this current is a conserved quantity.[12] We then recognize j^μ as the classical electromagnetic 4-current density.

Now back to quantum fields: let us return to equation (1.13). Setting the quark mass to

[12]To show this, just act on the Dirac Equation with $\bar{q}_i$ on the left, act on the Hermitian Conjugate of the Dirac Equation with q_i on the right, then add the two equations.

zero and substituting in our expression for the electromagnetic current, we arrive at:

$$\mathcal{L}_{QCD}^{U1} = i\bar{q}\gamma^{\mu}\partial_{\mu}q + Qj_{\mu}^{EM}A^{\mu} - \frac{1}{4}F^{\mu\nu}F_{\mu\nu} \tag{1.31}$$

The interesting piece here is the second term: the Lagrangian is apparently directly proportional to terms with the conserved current contracted with the field mediator. Now if we can find conserved currents for the weak force, it will be a simple matter to add the weak sector into our Lagrangian.

Weak Isospin

We now define weak isospin to be $+1/2$ for left-handed particles and 0 for right-handed particles. The left-handed particles can then be arranged into generational doublets; the upper member of the doublet (neutrinos or up-type quarks) are said to have the z-component of weak isospin (T_3) equal to $+1/2$, whereas the lower member of the doublet (charged leptons and down-type quarks) have $T_3 = -1/2$. Aside from organizing the particles and enforcing gauge invariance, weak isospin is a useful concept because T_3 is conserved even in weak interactions.

The doublets and singlets are defined as follows:

$$\chi_L = \begin{pmatrix} f_u \\ f_d \end{pmatrix} = \begin{pmatrix} \nu_e \\ e_L \end{pmatrix}, \begin{pmatrix} \nu_\mu \\ \mu_L \end{pmatrix}, \begin{pmatrix} \nu_\tau \\ \tau_L \end{pmatrix}, \begin{pmatrix} u_L \\ d_L \end{pmatrix}, \begin{pmatrix} c_L \\ s_L \end{pmatrix}, \begin{pmatrix} t_L \\ b_L \end{pmatrix} \tag{1.32}$$

$$\chi_R = e_R, \mu_R, \tau_R, u_R, d_R, c_R, s_R, t_R, d_R$$

Projection Operators

Recall that the axioms differentiate between charged-current interactions (which allow, and require, the fermion's T_3 to change), and neutral-current interactions (which require the fermion's T_3 to be constant). The challenge of the electroweak theory is that it violates parity: the charged-current weak interactions couples only to left-handed particles, while the neutral-current weak interactions couple more strongly (but not exclusively) to left-handed particles.[13] We will have to build this into our theory.

To do this, we write the fermions, represented by Dirac 4-spinors, in the Weyl Representation as:

$$f = \begin{pmatrix} f_L \\ \bar{f}_R \end{pmatrix} \tag{1.33}$$

where the top field is the left-handed version of a given fermion spinor, and the bottom field is the right-handed antifermion spinor. We can project out the left-handed fermion (right-handed antifermion) by using the projection operator P_L (P_R), where:

$$P_L = \frac{1-\gamma^5}{2};\ P_R = \frac{1+\gamma^5}{2} \tag{1.34}$$

For future convenience, we note the following useful identities[14] involving these equations:

$$\left(\frac{1+\gamma^5}{2}\right)\gamma^\mu\left(\frac{1-\gamma^5}{2}\right) = \gamma^\mu\left(\frac{1-\gamma^5}{2}\right) \tag{1.35}$$

$$P_L^2 = P_L; P_R^2 = P_R \tag{1.36}$$

[13] Note that this is partially accounted for by the T_3 conservation: right-handed particles have $T_3 = 0$, and therefore cannot undergo charged-current weak interactions. However, this does not explain why right-handed particles behaving differently under neutral-current weak interations.

[14] These are easy to prove; see for example eq. 9.126-9.128. of [1].

Electroweak Physical Currents

We have already derived the electromagnetic current for quarks (equation (1.30)). Generalizing this result for all fermions, we have:

$$J_\mu^{EM} = -\bar{f}\gamma_\mu f \tag{1.37}$$

and the Lagrangian from this current is (in analogy with equation (1.31)):

$$\mathcal{L}_{EM}^{int} = Q J_\mu^{EM} A^\mu \tag{1.38}$$

Note that $\mathcal{L}_{EM}^{int}$ is only the interaction part of equation (1.31); we neglect for the moment the kinetic terms for the fermions or the photon.

We postulate that the charged-current weak interaction must have a similar form, with Q replaced by T_3. For an incoming fermion f_u ($T_3 = 1/2$) and an outgoing fermion f_ℓ ($T_3 = -1/2$), for example, we might imagine the (positive) charged-current to be of the form $J_{CC+}^\mu = -\bar{f}_u \gamma_\mu T_3 f_\ell$. However, we need to build in the parity violation: this charged-current interaction can only affect the left handed particles. We simply insert the projection operator:

$$J_{CC+}^\mu = -\bar{f}_u \gamma^\mu T_3 P_L f_\ell \tag{1.39}$$

and then use the identity from equation (1.35):

$$J_{CC+}^\mu = -\bar{f}_u \left(\frac{1+\gamma^5}{2}\right) \gamma^\mu T_3 \left(\frac{1-\gamma^5}{2}\right) f_\ell \tag{1.40}$$

This properly separates out the left-handed parts of the field, leaving us with:

$$J^{\mu}_{CC+} = -\bar{f}^{L}_{u} T_3 \gamma^{\mu} f^{L}_{\ell} \tag{1.41}$$

Further, $T_3 f^L_\ell = -\frac{1}{2} f^L_\ell$, so:

$$J^{\mu}_{CC+} = \frac{1}{2} \bar{f}^{L}_{u} \gamma^{\mu} f^{L}_{\ell} \tag{1.42}$$

The doublet and siglet notation of equation (1.32) allows us to write equation (1.42) as:

$$J^{\mu}_{CC+} = \frac{1}{2} \bar{\chi}_L \gamma^{\mu} \begin{pmatrix} 0 & 1 \\ 0 & 0 \end{pmatrix} \chi_L \tag{1.43}$$

By the same argument, the negative charged-current interaction is given by:

$$J^{\mu}_{CC-} = -\frac{1}{2} \bar{\chi}_L \gamma^{\mu} \begin{pmatrix} 0 & 0 \\ 1 & 0 \end{pmatrix} \chi_L \tag{1.44}$$

Now for the neutral currents. These are a bit more challenging because the parity violation is not absolute: there is a preference but not a requirement for left-handed particles. We can require this if we generalize equation (1.40) as follows:

$$J^{\mu}_{NC} = \bar{f} \gamma^{\mu} (c_V - c_A \gamma^5) f \tag{1.45}$$

Notice that $c_V = 1, c_A = 0$ means parity symmetry, while $c_V = c_A = \frac{1}{2}$ means maximal parity violation, as with the charged currents. Our axioms tell us that the actual values must be somewhere between these extremes.[15]

[15] As previously, T_3 has acted upon f to return $\pm 1/2$; this factor was then absorbed into the coefficients c_V and c_A.

We now have four electroweak currents: J^μ_{CC+}, J^μ_{CC-}, J^μ_{NC}, and J^μ_{EM}. These handle parity properly and seem consistent with our observations about T_3 conservation. We could therefore build a Lagrangian out of these currents analogous to equation (1.31), and declare victory. The problem is the gauge invariance, if this "electroweak" theory has any $SU(2)_L \times U(1)$ symmetry, it is not at all manifest, either locally or globally. We turn to this now.

Electroweak Gauge Currents

Looking at the charged currents of equations (1.43) and (1.44), we recognize the matrices as the SU(2) raising operator [$\tau_\pm = \frac{1}{2}(\tau_1 \pm i\tau_2)$], where τ_i are the Pauli matrices. Given this, it would be nice to rewrite our currents using the Pauli matrices – this would give us a manifest SU(2) symmetry. In other words, we want to rewrite the three weak currents as (we can call these the gauge currents):

$$J^i_\mu = -\frac{1}{2}\bar{\chi}_L \gamma^\mu \tau_i \chi_L \tag{1.46}$$

For the first two currents, this seems like a good idea; we can easily relate the physical charged currents in terms of the gauge currents:

$$\begin{pmatrix} J^\mu_{CC+} \\ J^\mu_{CC-} \end{pmatrix} = \frac{1}{2}\begin{pmatrix} 1 & i \\ 1 & -i \end{pmatrix}\begin{pmatrix} J^\mu_1 \\ J^\mu_2 \end{pmatrix} \tag{1.47}$$

The advantage to this notation is that the weak gauge currents are manifestly invariant under a global SU(2) symmetry; the disadvantage is that now the physical charged currents are obfuscated.

But there is a problem: since the first two gauge currents correspond to the charged

physical currents, it follows that J_3^μ must be the neutral current. This is not possible: J_3^μ is not consistent with equation (1.45). The only way to make J_3^μ consistent with equation (1.45) would be to set $c_V = c_A = \frac{1}{2}$, which would disallow all right-handed coupling; this would contradict our axioms. To rescue this theory, we must introduce a *second* neutral weak gauge current. Just as the J_1^μ and J_2^μ combine in different ways to form $J_{CC\pm}^\mu$, so we anticipate that J_3^μ and the new current J_Y^μ must combine in different ways to form J_{NC}^μ and J_{EM}^μ. In this way, we will have unified the electromagnetic and weak forces.

Noting that J_{EM}^μ is based on Q while J_3^μ is based on T_3, it follows that this new current must be based on that component of Q which is orthogonal to T_3. We therefore define the hypercharge Y as:

$$Q = T_3 + \frac{1}{2}Y \tag{1.48}$$

where the factor of $\frac{1}{2}$ is inserted for later convenience. Given this, our fourth conserved current is simply:

$$J_\mu^Y = \bar{f}\gamma_\mu \frac{Y}{2} f \tag{1.49}$$

And by construction, it must be possible to represent our four physical currents in terms of our four gauge currents.

Electroweak Interaction Lagrangian

Now we have our conserved currents (gauge and physical) are so we are ready to build an electroweak Lagrangian. We postulate that the form of this Lagrangian will have the same structure that it did in the purely electromagnetic case (equation 1.38): a coupling constant, a conserved current, and a boson. We will therefore write a Lagrangian with four terms: the four currents, four bosons, and four coupling constants. Should we use the gauge currents or the physical currents? In principle, we can use *either*, the resulting

Lagrangian must be *exactly the same*. But it's easier to use the gauge currents because we know that to preserve our SU(2) symmetry, the triplet of gauge currents J_i^μ must have the same coupling constant. Thus,

$$\mathcal{L}_{EW}^{int} = -igJ_\mu^i W_i^\mu - ig' j_\mu^Y B^\mu \tag{1.50}$$

This is the electroweak Lagrangian written with a manifest SU(2) $\times$ U(1) symmetry.

Now this meets all of our axioms! However, we don't get much physical intuition from equation (1.50). To that end we will plug in the definition of the gauge currents and gauge fields so that we can express this same Lagrangian in terms of the physical fields.

We begin with the charged currents. Equating the Lagrangian with the gauge currents with that of the physical currents, we have:

$$-igJ^1W^1 - igJ^2W^2 = -igJ_{CC}^+W^+ - igJ_{CC}^-W^- \tag{1.51}$$

Then we plug in equation (1.47) and do the linear algebra to determine:

$$\begin{pmatrix} W_+^\mu \\ W_-^\mu \end{pmatrix} = \begin{pmatrix} 1 & -i \\ 1 & i \end{pmatrix} \begin{pmatrix} W_1^\mu \\ W_2^\mu \end{pmatrix} \tag{1.52}$$

For the neutral currents, the unknown factors of c_V and c_A make it impossible to know which combination of the gauge fields is the correct one. Instead, we will simply define

θ_W to be the proper rotation of the fields, and then we have.

$$\begin{pmatrix} Z_0^\mu \\ A^\mu \end{pmatrix} = \begin{pmatrix} \cos\theta_W & -\sin\theta_W \\ \sin\theta_W & \cos\theta_W \end{pmatrix} \begin{pmatrix} W_3^\mu \\ B^\mu \end{pmatrix} \tag{1.53}$$

Now we have what we need to calculate the entire physical Lagrangian. Let's start by considering the neutral-current part of the Lagrangian, written with the gauge currents:

$$\mathcal{L}_{EW}^{neut} = igJ_\mu^3 W_3^\mu + ig' j_\mu^Y B^\mu \tag{1.54}$$

Now we plug in equation (1.53). This gives:

$$\mathcal{L}_{EW}^{neut} = i\left[gJ_\mu^3 \sin\theta_W + g' j_\mu^Y \cos\theta_W\right] A^\mu + i\left[gJ_\mu^3 \cos\theta_W - g' j_\mu^Y \sin\theta_W\right] Z_0^\mu \tag{1.55}$$

Comparing this with equation (1.31), we see that the first term in brackets must be equal to j_{EM}^μ for all fermions. As an example, we consider the case of the electron, with $Q = -1$, $T_3 = -1/2$ and (by (1.48)) $Y = -1$. This gives:

$$g\sin\theta_W = g'\cos\theta_W = e \tag{1.56}$$

where e is the electron charge. This allows us to express g' in terms of g and the weak mixing angle:

$$g' = g\tan\theta_W \tag{1.57}$$

With this, (1.50) is rewritten:

$$\boxed{\mathcal{L}_{EW}^{int} = -igJ_\mu^i W_i^\mu - ig\tan\theta_W j_\mu^Y B^\mu} \tag{1.58}$$

We can also use this relationship on equation (1.55):

$$\mathcal{L}_{EW}^{neut} = ig\left[J_\mu^3 \sin\theta_W + \tan\theta j_\mu^Y \cos\theta_W\right] A^\mu + ig\left[J_\mu^3 \cos\theta_W - \tan\theta j_\mu^Y \sin\theta_W\right] Z_0^\mu \quad (1.59)$$

Now we simply substitute in the currents and simplify.

$$\mathcal{L}_{EW}^{neut} = -\frac{ig}{2}\left(\bar{f}_u^L \gamma^\mu f_u^L \sin\theta A - \bar{f}_\ell^L \gamma^\mu f_\ell^L \sin\theta A + \tan\theta \cos\theta \bar{f}\gamma^\mu Y f A\right) \quad (1.60)$$

And now we write out the terms for the diferent left- and right-handed leptons and quarks, inserting the proper value of the hypercharge for each. The result is:

$$\begin{aligned}
\mathcal{L}_{EW}^{neut} \;=\;& ig\bar{\ell}\gamma^\mu \ell \sin\theta_W A - \tfrac{2ig}{3}\sin\theta_W \bar{u}\gamma^\mu u A + \tfrac{ig}{3}\sin\theta_W \bar{d}\gamma^\mu d A - \tfrac{ig}{2}\bar{\nu}\gamma^\mu \nu Z \sec\theta_W \\
& -\tfrac{ig}{4}\bar{\ell}\gamma^\mu \ell Z \sec\theta_W (4\sin^2\theta_W - 1) - \tfrac{ig}{4}\bar{\ell}\gamma^\mu\gamma_5 \ell Z \sec\theta_W \\
& +\tfrac{ig}{2}\bar{u}\gamma^\mu u Z\left(\tfrac{1}{2} - \tfrac{4}{3}\sin^2\theta_W\right)\sec\theta_W + \tfrac{ig}{4}\bar{u}\gamma^\mu\gamma_5 u Z \sec\theta_W + \\
& \tfrac{ig}{4}\bar{d}\gamma^\mu d Z \sec\theta_W\left(\tfrac{4}{3}\cos^2\theta_W - \tfrac{1}{3}\right) - \tfrac{ig}{4}\bar{d}\gamma^\mu d\gamma_5 \sec\theta_W Z
\end{aligned} \quad (1.61)$$

A note on our notation. We implicitly sum over $\ell = e,\ \mu,\ \tau$. We further define ν (no subscript) to be a sum over the three (left-handed) neutrino flavors, u and d to be a sum over the up-type and down-type quark flavors, and q (no subscript) to be a sum over all the quark flavors.

Notice how nicely this works out. There is no neutrino-photon coupling, but there is lepton- and quark-photon coupling. The photon coupling does not violate parity, and is everywhere dependent on charge. Further, we can read off c_V and c_A from equation (1.45) for the different types of Z-coupling.

For the charged-current couplings, the procedure is similar, but much simpler since we

can use equation (1.52). The result is:

$$\boxed{\mathcal{L}_{EW}^{charged} = \frac{ig}{2}\left(\bar{\nu}\gamma^{\mu}\ell W^{-} + V_{ud}\bar{u}\gamma^{\mu}dW^{-} + \bar{\ell}\gamma^{\mu}\nu W^{+} + V_{ud}^{*}\bar{d}\gamma^{\mu}uW^{+}\right)} \tag{1.62}$$

We have added a factor of V_{ud} to account for the probability that a given up-type quark will decay into a given down-type quark (this would be unity if there were only two quarks; as it is, it is a 3x3 matrix with four degrees of freedom).

Kinetic Energy and Self-Interaction

Recall that the $\mathcal{L}_{EW}^{int}$ that we identified in the previous section is only the interaction term; we have not yet addressed the kinetic or mass terms. The SU(2) symmetry, just like the SU(3) symmetry, is non-Abelian, and so we must again set all of our particle masses to zero to get a local SU(2) gauge invariance. But we do need the kinetic terms. We begin with the kinetic terms for the leptons; this is easy enough:

$$\boxed{\mathcal{L}_{K} = i\bar{\chi}\gamma^{\mu}\partial_{\mu}\chi} \tag{1.63}$$

And we can expand this in terms of the physical fields:

$$\boxed{\mathcal{L}_{K} = i\bar{\nu}\gamma^{\mu}\partial_{\mu}\nu + i\bar{\ell}\gamma^{\mu}\partial_{\mu}\ell + i\bar{u}\gamma^{\mu}\partial_{\mu}u + i\bar{d}\gamma^{\mu}\partial_{\mu}d} \tag{1.64}$$

Next we do the kinetic terms for the electroweak bosons. As in the QCD case, these are non-abelian and therefore require self-interaction terms in order to follow their equations of motion without breaking the gauge invariance. We will write this in a separate piece of the Lagrangian which we will call $\mathcal{L}_{EW}^{KESI}$, for "kinetic energy and self-interaction." This

is:

$$\boxed{\mathcal{L}_{KESI} = \frac{1}{4}W_{\mu\nu}W^{\mu\nu} + \frac{1}{4}B_{\mu\nu}B^{\mu\nu}} \tag{1.65}$$

where:

$$\begin{aligned} W^{\mu\nu} &= \partial^\mu W^\nu - \partial^\nu W^\mu - ig\varepsilon^{abc}W^b_\mu W^c_\nu \\ B^{\mu\nu} &= \partial^\mu B^\nu - \partial^\nu B^\mu \end{aligned} \tag{1.66}$$

First, we do our usual test to see whether this is gauge-invariant. We take:

$$\begin{aligned} f &\rightarrow f - ig\vec{\tau}\cdot\vec{a}(x) - ig\tan\theta\ b(x) \\ W^a_\mu &\rightarrow W^a_\mu - \tfrac{1}{g}\partial_\mu a(x)^a - g\varepsilon^{abc}W^a_\mu a(x)^b\tau^c \\ B_\mu &\rightarrow B_\mu - \tfrac{1}{g\tan\theta}\partial_\mu b(x) \end{aligned} \tag{1.67}$$

The form of these transformations was determined in analogy with the process in the SU(3) theory. The result is that the Lagrangian is indeed invariant under these transformations; predictable since we constructed this theory in analogy with another locally-invariant theory.

Finally, we expand this out in terms of the physical fields (1.66):

$$\begin{aligned} \mathcal{L}_{KESI} &= \tfrac{1}{4}(\partial^\mu W_1^\nu - \partial^\nu W_1^\mu)(\partial_\mu W_\nu^1 - \partial_\nu W_\mu^1) + \tfrac{1}{4}(\partial^\mu W_2^\nu - \partial^\nu W_2^\mu)(\partial_\mu W_\nu^2 - \partial_\nu W_\mu^2) \\ &+\tfrac{1}{4}(\partial^\mu W_3^\nu - \partial^\nu W_3^\mu)(\partial_\mu W_\nu^3 - \partial_\nu W_\mu^3) + \tfrac{1}{4}(\partial^\mu B^\nu - \partial^\nu B^\mu)(\partial_\mu B_\nu - \partial_\nu B_\mu) \\ &+\tfrac{ig}{2}\left[\partial_\mu W_\nu^1 W_2^\nu W_3^\mu - \partial_\mu W_\nu^1 W_3^\nu W_2^\mu\right] + \tfrac{ig}{2}\left[\partial_\mu W_\nu^2 W_3^\nu W_1^\mu - \partial_\mu W_\nu^2 W_1^\nu W_3^\mu\right] \\ &+\tfrac{ig}{2}\left[\partial_\mu W_\nu^3 W_1^\nu W_2^\mu - \partial_\mu W_\nu^3 W_2^\nu W_1^\mu\right] - \tfrac{g^2}{4}W_2^\mu W_\mu^2 W_3^\nu W_\nu^3 - \tfrac{g^2}{4}W_3^\mu W_\mu^3 W_1^\nu W_\nu^1 \\ &-\tfrac{g^2}{4}W_1^\mu W_\mu^1 W_2^\nu W_\nu^2 \end{aligned} \tag{1.68}$$

Now we can transform the gauge fields into the physical fields using equations (1.53). This process is very long and painful; the result is:

$$
\begin{aligned}
\mathcal{L}_{KESI} \;=\; & \tfrac{1}{4}(\partial^\mu W_+^\nu - \partial^\nu W_+^\mu)(\partial_\mu W_\nu^+ - \partial_\nu W_\mu^+) + \tfrac{1}{4}(\partial^\mu W_-^\nu - \partial^\nu W_-^\mu)(\partial_\mu W_\nu^- - \partial_\nu W_\mu^-) \\
& \tfrac{1}{4}(\partial^\mu Z^\nu - \partial^\nu Z^\mu)(\partial_\mu Z_\nu - \partial_\nu Z_\mu) + \tfrac{1}{4}(\partial^\mu A^\nu - \partial^\nu A^\mu)(\partial_\mu A_\nu - \partial_\nu A_\mu) \\
& + g\cos\theta_W Z^\nu W_-^\mu \partial_\mu W_\nu^+ + g\sin\theta_W A^\nu W_-^\mu \partial_\mu W_\nu^+ - g\cos\theta_W Z^\nu W_+^\mu \partial_\mu W_\nu^- \\
& - g\sin\theta_W A^\nu W_+^\mu \partial_\mu W_\nu^- - g\cos\theta_W Z^\mu W_-^\nu \partial_\mu W_\nu^+ - g\sin\theta_W A^\mu W_-^\nu \partial_\mu W_\nu^+ \\
& + g\cos\theta_W Z^\mu W_+^\nu \partial_\mu W_\nu^- + g\sin\theta_W A^\mu W_+^\nu \partial_\mu W_\nu^- - g\cos\theta_W W_+^\nu W_-^\mu \partial_\mu Z_\nu \\
& - g\sin\theta_W W_+^\nu W_-^\mu \partial_\mu A_\nu + g\cos\theta_W W_-^\nu W_+^\mu \partial_\mu Z_\nu + g\sin\theta_W W_+^\mu W_-^\nu \partial_\mu A_\nu \\
& - g^2\sin^2\theta_W A_\nu A^\nu W_\mu^+ W_-^\mu + \tfrac{1}{2}g^2\sin^2\theta_W A_\mu A^\nu W_+^\mu W_\nu^- + \tfrac{1}{2}g^2\sin^2\theta_W A_\mu A^\nu W_-^\nu W_\mu^+ \\
& - \tfrac{1}{4}g^2 W_\mu^+ W_+^\mu W_\nu^- W_-^\nu - \tfrac{1}{4}g^2 W_\mu^- W_+^\mu W_\nu^+ W_-^\nu + \tfrac{1}{2}g^2 W_\mu^- W_+^\mu W_\nu^+ W_-^\nu \\
& + g^2\cos\theta_W \sin\theta_W A^\nu W_+^\mu W_\nu^- Z_\mu + g^2\cos\theta_W \sin\theta_W A^\nu W_-^\mu W_\nu^+ Z_\mu \\
& - 2g^2\cos\theta_W \sin\theta_W A^\mu W_-^\nu W_\nu^+ Z_\mu - g^2\cos^2\theta_W W_\nu^- W_+^\nu Z_\mu Z^\mu \\
& + \tfrac{1}{2}g^2\cos^2\theta_W W_\mu^+ W_-^\nu Z^\mu Z_\nu + \tfrac{1}{2}g^2\cos^2\theta_W W_\mu^- W_+^\nu Z^\mu Z_\nu
\end{aligned}
\tag{1.69}
$$

There are a few features of this ridiculous equation worth noting. First, it is the $\mathcal{L}_{KESI}$ that provides the kinetic terms for all four gauge bosons, as well as the three-boson and four-boson couplings. If it were not for the non-Abelian nature of the transformations, there would be no self-interactions. Second, it is interesting to notice that the $W^+W^-W^+W^-$ term appears but no $ZZZZ$ vertex does. There's no conservation law that excludes a 4-Z coupling; it's just that the pieces apparently don't fit together that way in the Standard Model.

We have now constructed a theory of 36 quarks and 12 leptons, mediated by 12 bosons. The only problem with what we have done is the masses: this Lagrangian predicts that every particle should be massless. As we have seen, directly adding mass terms of the

form $\frac{1}{2}M_f^2 f^2$ would spoil the local gauge invariance under the non-Abelian transformations. We will solve this problem by using the Higgs Mechanism.

1.4 The Higgs Mechanism

To make the W and Z massive, we will need three additional degrees of freedom (corresponding to the longitudinal polarization on each boson). We further want this term to affect both the SU(2) and the U(1) component of the Lagrangian, so we need something that is charged with a nonzero weak hypercharge as well as a weak isospin. The simplest field meeting these criteria is a complex doublet:

$$\phi = \frac{1}{\sqrt{2}} \begin{pmatrix} \phi_1 + i\phi_2 \\ \phi_3 + i\phi_4 \end{pmatrix} \tag{1.70}$$

Just as in the leptonic doublet, we will take the top component to be electrically charged (positively) and the bottom component to be electrically neutral. Further, the upper component of the doublet always has $T^3 = +1/2$ while the lower component has $T^3 = -1/2$. Given this, the hypercharge for the doublet is $+1$.

We now want this to enter the Lagrangian. The kinetic term needs to respect the $SU(2) \times U(1)$ symmetry we found above. Thus:

$$\mathcal{L}_H = \left| \left(i\partial_\mu - gT \cdot W_\mu - \frac{g'}{2} Y B_\mu \right) \phi \right|^2 - V(\phi) \tag{1.71}$$

Let's further postulate that this scalar field has a potential energy of the form:

$$V(\phi) = \mu^2 \phi^\dagger \phi + \lambda (\phi^\dagger \phi)^2 \tag{1.72}$$

where $\mu^2 < 0$ and $\lambda > 0$. Thus, our proposed Higgs Lagrangian is given by:

$$\boxed{\mathcal{L}_H = \left| \left(i\partial_\mu - gT \cdot W_\mu - \frac{g'}{2} Y B_\mu \right) \phi \right|^2 - \mu^2 \phi^\dagger \phi - \lambda (\phi^\dagger \phi)^2} \tag{1.73}$$

The minimum of this is not zero, as in all the other fields we have considered, but is rather given by:

$$|v| = \sqrt{\frac{-\mu^2}{\lambda}} \tag{1.74}$$

Now we must recall that our calculations above are based on the free equations of motion, and so are only valid as a perturbation around the vacuum. Up until now, the minimum value of every field (the vacuum expectation value) has been zero, and so this worked out naturally. In this case, however, the vacuum expectation value (VEV) is nonzero, and so we must perturb the field around the v.

However, the system is still underconstrained – there are many combinations of the fields that would give this minimum magnitude. No matter what we choose, our system will still be locally gauge-invariant. However, it would be nice to choose the vacuum as:

$$\text{vacuum} = \frac{1}{\sqrt{2}} \begin{pmatrix} 0 \\ v \end{pmatrix} \tag{1.75}$$

The advantage here is that $Q = T^3 + \frac{1}{2}Y = -\frac{1}{2} + \frac{1}{2} = 0$, so that the vacuum is electrically neutral. The physical vacuum (and only the physical vacuum, not all the fields in our Lagrangian) are thus not invariant under SU(2), but only under $U(1)_{EM}$.

At any rate, let us expand the kinetic terms in our Lagrangian in the vacuum. We

have:

$$\mathcal{L}_H = \frac{1}{2}\left|\left(-iT^2W_\mu^1 - gT^2W_m u^2 - gT^3W_\mu^3 - \frac{g'}{2}YB_\mu\right)\begin{pmatrix}0\\ v\end{pmatrix}\right|^2 - \mu^2\phi^\dagger\phi - \lambda(\phi^\dagger\phi)^2 \quad (1.76)$$

For notational convenience, let's consider only the kinetic part of $\mathcal{L}_H$, $\mathcal{L}_{H,K}$:

$$\mathcal{L}_{H,K} = \frac{1}{2}\left|\left(-iT^2W_\mu^1 - gT^2W_m u^2 - gT^3W_\mu^3 - \frac{g'}{2}YB_\mu\right)\begin{pmatrix}0\\ v\end{pmatrix}\right|^2 \quad (1.77)$$

Expanding this, and recalling that $T^i = \frac{1}{2}\tau^i$:

$$\mathcal{L}_{H,K} = \frac{1}{2}\left|\begin{pmatrix}-\frac{g}{2}W_\mu^3 - \frac{g'}{2}YB_\mu & -\frac{g}{2}W_\mu^1 + \frac{ig}{2}W_\mu^2\\ -\frac{g}{2}W_\mu^1 - \frac{ig}{2}W_\mu^2 & \frac{g}{2}W_\mu^3 - \frac{g'}{2}YB_\mu\end{pmatrix}\begin{pmatrix}0\\ v\end{pmatrix}\right|^2 \quad (1.78)$$

Multiplying, and recalling that this doublet has hypercharge +1:

$$\mathcal{L}_{H,K} = \frac{1}{2}\left|\begin{pmatrix}-\frac{gv}{2}W_\mu^1 + \frac{igv}{2}W_\mu^2\\ \frac{vg}{2}W_\mu^3 - \frac{vg'}{2}B_\mu\end{pmatrix}\right|^2 \quad (1.79)$$

which is:

$$\mathcal{L}_{H,K} = \frac{1}{2}\left|\begin{pmatrix}-\frac{gv}{2}\left(W_\mu^1 - iW_\mu^2\right)\\ \frac{vg}{2}\left(W_\mu^3 - \frac{g'}{g}B_\mu\right)\end{pmatrix}\right|^2 \quad (1.80)$$

We evaluate this. Further, we write the last term in a suggestive notation:

$$\begin{aligned}\mathcal{L}_{H,K} &= \tfrac{1}{2}\left(\tfrac{gv}{2}\right)^2(W_1 - iW_2)_\mu(W_1 + iW_2)^\mu \\ &\quad + \tfrac{1}{2}\left(\tfrac{gv}{2}\right)^2\left[1 + (g'/g)^2\right]\left(\frac{W_3 - \frac{g'}{g}B}{\sqrt{1+(g'/g)^2}}\right)_\mu\left(\frac{W_3 - \frac{g'}{g}B}{\sqrt{1+(g'/g)^2}}\right)^\mu\end{aligned}$$

These are mass terms! We therefore identify $W_\mu^\pm = W_\mu^1 \mp iW_\mu^2$ and $Z_\mu = \frac{W_\mu^3 - (g'/g)B_\mu}{\sqrt{1+(g'/g)^2}}$ as the massive bosons. The orthogonal combination of the W_3 and B fields – the photon – has no such term and is therefore massless (this motivated our choice of the vacuum breaking). This gives:

$$\mathcal{L}_{H,K} = \frac{1}{2}\left(\frac{gv}{2}\right)^2 W_\mu^- W_+^\mu + \frac{1}{2}\left(\frac{gv}{2}\right)^2 [1 + \tan^2\theta_W] Z_\mu Z^\mu \tag{1.81}$$

Notice that the fields worked out in exactly the way we predicted from the currents: $W^\pm$ is a combination of W^1 and W^2, whereas the electromagnetic and neutral-currents are combinations of W^3 and Y.

We can now read off the values of the boson masses:

$$\begin{aligned} M_W &= \tfrac{gv}{2} \\ M_Z &= \tfrac{gv}{2\cos\theta_W} \end{aligned} \tag{1.82}$$

We have therefore predicted that the Z boson is heavier than the W boson; we can further calculate v and $\tan\theta_W$ by experimentally measuring the boson masses.

Let us also consider the potential energy part of the Lagrangian. We have a term of the form:

$$V(\phi) = -\mu^2\phi^2 - \frac{1}{4}\lambda\phi^4 \tag{1.83}$$

Now that we are perturbing around the minimum, we can write the ϕ field as:

$$\phi = \begin{pmatrix} a(x) + ib(x) \\ v + h(x) + ic(x) \end{pmatrix} \tag{1.84}$$

There is a problem. Here we have four degrees of freedom (the value of each of the four fields), exactly as we had before we broke the symmetry. But by breaking the symmetry, we generated a mass for each boson. Massive particles can be longitudinally polarized, and so we somehow gained three degrees of freedom! This is not appropriate: relabeling our field variables should not create degrees of freedom.

The solution is in choosing a particular gauge. To reiterate: up until now, we have required our Lagrangian to respect a local SU(2) gauge invariance, so our Lagrangian is invariant under:

$$\begin{aligned} \phi &\rightarrow e^{i\alpha_a \tau_a/2}\phi \\ A^\mu &\rightarrow A^\mu - \tfrac{ig}{2}\tau_a W_a^\mu \end{aligned} \tag{1.85}$$

for any (numeric) α_a – three degrees of freedom. By choosing a particular gauge, then, we will lose the extra three degrees of freedom.[16]. We choose to select a gauge such that only h(x) is nonzero.

It may seem counter-intuitive to break the gauge invariance, considering that we constructed the entire theory based on the idea of gauge invariance! However, the gauge invariance is not "really" broken, just hidden by our decision to expand around a particular ground state and choose a particular gauge.

With this broken, we have:

$$\phi = \frac{1}{\sqrt{2}} \begin{pmatrix} 0 \\ v+h \end{pmatrix} \tag{1.86}$$

[16]It is worth mentioning that if we had failed to do this, our perturbation fields would have masses!

Now let us consider the potential energy term of the Lagrangian:

$$V(\phi) = \mu^2\phi^2 + \lambda\phi^4 \tag{1.87}$$

Plugging in our expression for ϕ, we have:

$$V(\phi) = \frac{\mu^2}{2}(v+h)^2 + \frac{\lambda}{4}(v+h)^4 \tag{1.88}$$

By explicit calculation, and dropping the terms with no factors of h, we find that the first-order (in h) terms cancel. Plugging in further our expression for v, we find:

$$V(\phi) = \frac{\lambda}{4}h^4 + \lambda v h^3 + v^2\lambda h^2 \tag{1.89}$$

This last term is a mass term! The Higgs mass is therefore:

$$m_H = 2v^2\lambda \tag{1.90}$$

Recall that the experimental values for the masses of the W and Z particles allowed us to solve for v. However, we have no way of knowing what λ is, and so we cannot predict the Higgs mass; it must be measured experimentally. On the other hand, we have predicted a tri-higgs and four-higgs coupling; given the Higgs mass, we could calculate the strength of those coupling constants.

The last step is to go back to equation (1.81) and update it with the new version of

ϕ – specifically, we take $v \to v + h$

$$\begin{aligned}\mathcal{L}_{H,K} &= \tfrac{1}{2}\left(\tfrac{gv}{2}\right)^2 W_\mu^- W_+^\mu + \tfrac{1}{2}(\tfrac{gv}{2})^2[1+\tan^2\theta_W]Z_\mu Z^\mu \\ &+\tfrac{1}{2}\left(\tfrac{2gvh}{2}\right)^2 W_\mu^- W_+^\mu + \tfrac{1}{2}(\tfrac{2gvh}{2})^2[1+\tan^2\theta_W]Z_\mu Z^\mu \\ &+\tfrac{1}{2}\left(\tfrac{gh}{2}\right)^2 W_\mu^- W_+^\mu + \tfrac{1}{2}(\tfrac{gh}{2})^2[1+\tan^2\theta_W]Z_\mu Z^\mu\end{aligned} \tag{1.91}$$

Combining this kinetic term with our potential term, we have our full Higgs Lagrangian:

$$\boxed{\begin{aligned}\mathcal{L}_H &= \tfrac{g^2v^2}{8}W_\mu^- W_+^\mu + \tfrac{g^2v^2}{8\cos\theta_W}Z_\mu Z^\mu + \tfrac{g^2v}{2}hW_\mu^- W_+^\mu + \tfrac{g^2v}{2\cos\theta_W}hZ_\mu Z^\mu \\ &+\tfrac{g^2}{8}h^2W_\mu^- W_+^\mu + \tfrac{g^2}{8\cos\theta_W}h^2Z_\mu Z^\mu + \tfrac{\lambda}{4}h^4 + \lambda v h^3 + v^2\lambda h^2\end{aligned}} \tag{1.92}$$

Lepton Masses

All of our gauge bosons now have the proper mass. Our fermions, on the other hand, are still massless, which is manifestly unacceptable. We must therefore include an SU(2) $\times$ U(1) invariant term in the Lagrangian. We'll start with the leptons.

First we note (taking the electrons just as an example):

$$\begin{aligned}m_e\bar{e}e &= m_e\bar{e}\left[\tfrac{1}{2}(1-\gamma^5)+\tfrac{1}{2}(1+\gamma^5)\right]e \\ &= m_e(\bar{e}_R e_L + \bar{e}_L e_R)\end{aligned} \tag{1.93}$$

Then we postulate the following term for our Lagrangian:

$$\boxed{\mathcal{L}^{\ell,d}_{mass} = -G_{\ell,d}\left[\chi_L\phi\bar{\chi}_R + \bar{\chi}_R\phi^\dagger\chi_L\right]} \tag{1.94}$$

Plugging in our expression for ϕ in the case of electrons:

$$\mathcal{L} = -G_e \left[\begin{pmatrix} \bar{\nu}_L^e & e_L \end{pmatrix} \begin{pmatrix} 0 \\ v+h \end{pmatrix} e_R + \bar{e}_R \begin{pmatrix} 0 & v+h \end{pmatrix} \begin{pmatrix} \nu_L^e \\ e_L \end{pmatrix} \right] \tag{1.95}$$

which simplifies to:

$$\mathcal{L}_{LM} = -G_e e_L v e_R - G_e e_L h e_R + G_e \bar{e}_R v e_L + G_e \bar{e}_R h e_L \tag{1.96}$$

We recognize the first and third terms as mass terms: apparently $m_e = 2G_e v$. In fact, the electrons are just an example; this works in the same manner for all fermions. So:

$$m_f = 2G_f v \tag{1.97}$$

Our Lagrangian can thus be written as:

$$\mathcal{L} = -\frac{m_e}{2} e_L e_R - \frac{m_e}{2v} e_L h e_R + \frac{m_e}{2} \bar{e}_R e_L + \frac{m_e}{2v} \bar{e}_R h e_L \tag{1.98}$$

Finally, we restate the left- and right-handed terms using the chirality operators (ex: $e_L = \frac{1-\gamma^5}{2} e$) and simplify using equation (1.93). We find:

$$\mathcal{L}_{LM} = -\frac{m_e}{2} \bar{e} e - \frac{m_e}{2v} \bar{e} h e \tag{1.99}$$

Now our leptons all have masses. Further, we notice that there is some Higgs-lepton coupling, the strength of which depends on the mass of the fermion.

We repeat this procedure for all three lepton doublets:

$$\boxed{\mathcal{L}_{LM} = -\frac{m_\ell}{2}\bar{\ell}\ell - \frac{m_\ell}{2v}\bar{\ell}h\ell} \tag{1.100}$$

where, as usual, we sum over ℓ.

Quark Masses

We can add masses to down-type quarks in the same manner as leptons:

$$\mathcal{L} = -G_d\left[\chi_L\phi\bar{\chi}_R + \bar{\chi}_R\phi^\dagger\chi_L\right] \tag{1.101}$$

Just as above, this will generate a massive down quark and a massless up quark. To make the up quark massive, we must construct a new representation of the Higgs doublet:

$$\phi_c = -i\tau_2\phi^\dagger = \frac{1}{\sqrt{2}}\begin{pmatrix} v+h \\ 0 \end{pmatrix} \tag{1.102}$$

With this, our gauge-invariant Lagrangian for these up-type quarks is:

$$\boxed{\mathcal{L}^u_{mass} = -G_u\left[\chi_L\phi_C\bar{\chi}_R + \bar{\chi}_R\phi^\dagger_C\chi_L\right]} \tag{1.103}$$

and the physical Lagrangian is:

$$\mathcal{L}_{QM} = -G_d\left[\chi_L\phi\bar{\chi}_R + \bar{\chi}_R\phi^\dagger\chi_L\right] - G_u\left[\chi_L\phi_c\bar{\chi}_R + \bar{\chi}_R\phi^\dagger_c\chi_L\right] \tag{1.104}$$

We simplify this in the same manner as the leptons; the result is:

$$\boxed{\mathcal{L}_{QM} = -\frac{m_q}{2}\bar{q}q - \frac{m_q}{2v}\bar{q}hq} \tag{1.105}$$

where q without a subscript, as usual, represents a sum over all the quark flavors.

1.5 The Standard Model Lagrangian

Putting all our results from the previous three sections together, we arrive at last at the full Standard Model Lagrangian.

$$\mathcal{L} = \mathcal{L}_{QCD}^{SU3} + \mathcal{L}_{EW}^{neut} + \mathcal{L}_{EW}^{charged} + \mathcal{L}_K + \mathcal{L}_{KESI} + \mathcal{L}_H + \mathcal{L}_{LM} + \mathcal{L}_{QM} \tag{1.106}$$

We can write this in the compact notation, with manifest gauge invariance:

$$\begin{aligned}\mathcal{L}_{SM} \;=\; & i\bar{q}\gamma^\mu\partial_\mu q - g_s\bar{q}\gamma^\mu\left(\vec{\lambda}\cdot\vec{G}_\mu\right)q - \tfrac{1}{4}G^a_{\mu\nu}G_a^{\mu\nu} - igJ^i_\mu W_i^\mu - ig\tan\theta_W j^Y_\mu B^\mu + i\bar{\chi}\gamma^\mu\partial_\mu\chi \\ & + \tfrac{1}{4}W_{\mu\nu}W^{\mu\nu} + \tfrac{1}{4}B_{\mu\nu}B^{\mu\nu} + \left|\left(i\partial_\mu - gT\cdot W_\mu - \tfrac{g'}{2}YB_\mu\right)\phi\right|^2 - \mu^2\phi^\dagger\phi - \lambda(\phi^\dagger\phi)^2 \\ & - G_{\ell,d}\left[\chi_L\phi\bar{\chi}_R + \bar{\chi}_R\phi^\dagger\chi_L\right] - G_u\left[\chi_L\phi_C\bar{\chi}_R + \bar{\chi}_R\phi_C^\dagger\chi_L\right]\end{aligned} \tag{1.107}$$

Alternatively, we can simplify this as much as possible; this will make the gauge invariance less manifest, but will make it easier to identify the particle-particle interactions.

$$
\begin{aligned}
\mathcal{L}_{SM} \;=\;& i\bar{q}\gamma^\mu\partial_\mu q - \tfrac{1}{4}(\partial^\mu G^\nu - \partial^\nu G^\mu)(\partial_\mu G_\nu - \partial_\nu G_\mu) + \tfrac{1}{2}g f_{abc} G_b^\mu G_c^\nu \partial_\mu G_\nu \\
& -\tfrac{1}{2}g f_{abc} G_b^\mu G_c^\nu \partial_\nu G_\mu - \tfrac{1}{4}g^2 f_{abc} G_b^\mu G_c^\nu f_{ade} G_d^\mu G_e^\nu \\
& -g_s\gamma^\mu(G_\mu^3 + \tfrac{1}{\sqrt{3}}G_\mu^8)\bar{q}_r q_r + -g_s\gamma^\mu(G_\mu^1 - iG_\mu^2)\bar{q}_r q_b - g_s\gamma^\mu\bar{q}_r(G_\mu^4 - iG_\mu^5)q_g \\
& -g_s\gamma^\mu\bar{q}_b(G_\mu^1 + iG_\mu^2)q_r - g_s\gamma^\mu\bar{q}_b(-G_\mu^3 + \tfrac{1}{\sqrt{3}}G_\mu^8)q_b - g_s\gamma^\mu\bar{q}_b(G_\mu^6 - iG_\mu^7)q_g \\
& -g_s\gamma^\mu\bar{q}_g(G_\mu^4 + iG_\mu^5)q_r - g_s\gamma^\mu\bar{q}_b(G_\mu^6 + iG_\mu^7)q_g + g_s\gamma^\mu\bar{q}_g(\tfrac{2}{\sqrt{3}}G_\mu^8)q_g \\
& ig\bar{\ell}\gamma^\mu\ell\sin\theta A - \tfrac{2ig}{3}\sin\theta\bar{u}\gamma^\mu u A + \tfrac{ig}{3}\sin\theta\bar{d}\gamma^\mu d A - \tfrac{ig}{2}\bar{\nu}\gamma^\mu\nu Z\sec\theta \\
& -\tfrac{ig}{4}\bar{\ell}\gamma^\mu\ell Z\sec\theta(4\sin^2\theta - 1) - \tfrac{ig}{4}\bar{\ell}\gamma^\mu\gamma_5\ell Z\sec\theta \\
& +\tfrac{ig}{2}\bar{u}\gamma^\mu u Z\left(\tfrac{1}{2} - \tfrac{4}{3}\sin^2\theta\right)\sec\theta + \tfrac{ig}{4}\bar{u}\gamma^\mu\gamma_5 u Z\sec\theta + \\
& \tfrac{ig}{4}\bar{d}\gamma^\mu d Z\sec\theta\left(\tfrac{4}{3}\cos^2\theta - \tfrac{1}{3}\right) - \tfrac{ig}{4}\bar{d}\gamma^\mu d\gamma_5\sec\theta Z + \tfrac{ig}{2}\left(\bar{\nu}\gamma^\mu\ell W^- + V_{ud}\bar{u}\gamma^\mu d W^-\right. \\
& \left.+\bar{\ell}\gamma^\mu\nu W^+ + V_{ud}^*\bar{d}\gamma^\mu u W^+\right) + i\bar{\nu}\gamma^\mu\partial_\mu\nu + i\bar{\ell}\gamma^\mu\partial_\mu\ell + i\bar{u}\gamma^\mu\partial_\mu u + i\bar{d}\gamma^\mu\partial_\mu d \\
& \tfrac{1}{4}(\partial^\mu W_+^\nu - \partial^\nu W_+^\mu)(\partial_\mu W_\nu^+ - \partial_\nu W_\mu^+) + \tfrac{1}{4}(\partial^\mu W_-^\nu - \partial^\nu W_-^\mu)(\partial_\mu W_\nu^- - \partial_\nu W_\mu^-) \\
& \tfrac{1}{4}(\partial^\mu Z^\nu - \partial^\nu Z^\mu)(\partial_\mu Z_\nu - \partial_\nu Z_\mu) + \tfrac{1}{4}(\partial^\mu A^\nu - \partial^\nu A^\mu)(\partial_\mu A_\nu - \partial_\nu A_\mu) \\
& +g\cos\theta_W Z^\nu W_-^\mu\partial_\mu W_\nu^+ + g\sin\theta_W A^\nu W_-^\mu\partial_\mu W_\nu^+ - g\cos\theta_W Z^\nu W_+^\mu\partial_\mu W_\nu^- \\
& -g\sin\theta_W A^\nu W_+^\mu\partial_\mu W_\nu^- - g\cos\theta_W Z^\mu W_-^\nu\partial_\mu W_\nu^+ - g\sin\theta_W A^\mu W_-^\nu\partial_\mu W_\nu^+ \\
& +g\cos\theta_W Z^\mu W_+^\nu\partial_\mu W_\nu^- + g\sin\theta_W A^\mu W_+^\nu\partial_\mu W_\nu^- - g\cos\theta_W W_+^\nu W_-^\mu\partial_\mu Z_\nu \\
& -g\sin\theta_W W_+^\nu W_-^\mu\partial_\mu A_\nu + g\cos\theta_W W_-^\nu W_+^\mu\partial_\mu Z_\nu + g\sin\theta_W W_+^\mu W_-^\nu\partial_\mu A_\nu \\
& -g^2\sin^2\theta_W A_\nu A^\nu W_\mu^+ W_-^\mu + \tfrac{1}{2}g^2\sin^2\theta_W A_\mu A^\nu W_+^\mu W_\nu^- + \tfrac{1}{2}g^2\sin^2\theta_W A_\mu A^\nu W_-^\nu W_\mu^+ \\
& -\tfrac{1}{4}g^2 W_\mu^+ W_+^\mu W_\nu^- W_-^\nu - \tfrac{1}{4}g^2 W_\mu^- W_+^\mu W_\nu^+ W_-^\nu + \tfrac{1}{2}g^2 W_\mu^- W_+^\mu W_\nu^+ W_-^\nu \\
& +g^2\cos\theta_W\sin\theta_W A^\nu W_+^\mu W_\nu^- Z_\mu + g^2\cos\theta_W\sin\theta_W A^\nu W_-^\mu W_\nu^+ Z_\mu \\
& -2g^2\cos\theta_W\sin\theta_W A^\mu W_-^\nu W_\nu^+ Z_\mu - g^2\cos^2\theta_W W_\nu^- W_+^\nu Z_\mu Z^\mu \\
& +\tfrac{1}{2}g^2\cos^2\theta_W W_\mu^+ W_-^\nu Z^\mu Z_\nu + \tfrac{1}{2}g^2\cos^2\theta_W W_\mu^- W_+^\nu Z^\mu Z_\nu \tfrac{g^2v^2}{8} W_\mu^- W_+^\mu \\
& +\tfrac{g^2v^2}{8\cos\theta_W} Z_\mu Z^\mu + \tfrac{g^2v}{2} h W_\mu^- W_+^\mu + \tfrac{g^2v}{2\cos\theta_W} h Z_\mu Z^\mu + \tfrac{g^2}{8} h^2 W_\mu^- W_+^\mu - \tfrac{m_q}{2v}\bar{q}hq \\
& +\tfrac{g^2}{8\cos\theta_W} h^2 Z_\mu Z^\mu + \tfrac{\lambda}{4}h^4 + \lambda v h^3 + v^2\lambda h^2 - \tfrac{m_\ell}{2}\bar{\ell}\ell - \tfrac{m_\ell}{2v}\bar{\ell}h\ell - \tfrac{m_q}{2}\bar{q}q
\end{aligned}
\tag{1.108}
$$

In any representation, we notice that the Lagrangian has 19 free parameters: 6 quark masses; 3 masses for the charged leptons; 4 free parameters in the CKM matrix; the strong and electroweak coupling constants; the weak mixing angle (equivalently, the Higgs mass); the VEV of the Higgs, v; and the coupling constant of the Higgs field, λ.

Now that we have our Lagrangian, we in principle understand all interactions: collisions (such as $W^+W^- \to Z$), decays (such as $\mu^- \to \bar{\nu}_e e^- \nu_\mu$), and bound states (which are irrelevant for the purposes of this dissertation). In particular, the conclusions we take from equation (1.108) include:

- the list of allowed and disallowed particle interactions. We can therefore draw (Feynman) diagrams for any given process. We will use these diagrams throughout this dissertation.
- that the Standard Model gives mass to all particles except for the neutrinos, gluons, and photon.
- that the Higgs Boson is a requirement for massive fields in the SM, even though the Standard Model predated the discovery of the Higgs.

The next step would be to use equation (1.108) and standard methods from Quantum Field Theory to extract the cross-sections and decay constants for particular processes directly. However, the cross-sections used in this dissertation were calculated at high precision using automated tools, so it is not necessary to discuss the details of these calculations here.

1.6 Tests of the SM

The Standard Model has been rigorously tested over the past decades, and has had many successful predictions. We will discuss those briefly.

First, it successfully predicted several new particles. The Standard Model was proposed in the 1970s and predicted the Higgs boson (as discussed in section 1.4), which was discovered by CMS and ATLAS at CERN in 2012. In addition, the generation pairing of particles (see equation (1.32)) led to the prediction of the top quark and tau neutrino, which were discovered in 1995 by CDF at Fermilab and in 2000 by DONUT at Fermilab, respectively.[17]

Second, the predicted cross-sections and half-lives mentioned earlier provide many quantitative predictions of the Standard Model; these match the experimental observations nearly exactly. One excellent example is the "Stairway to Heaven" plots (figure 1.1) published by the CMS experiment showing excellent agreement between SM theory and experimental observation for various production cross-sections. In section 5.6, we will consider the commissioning plots for this analysis which show excellent agreement between prediction and data; this is a good cross-check for the Standard Model and the simulation software, as well as the detector perfomance.

In addition to recent results at the LHC, a number of electroweak tests were carried out by the ALEPH, DELPHI, L3, and OPAL experiments at the LEP collider. These tests make stringent measurements on the Standard Model free parameters (such as

[17] On the other hand, the 1974 discovery of the charm quark (also necessary for generation pairing) was not fully expected, and the top quark was not predicted until the surprise discovery of the bottom quark at Fermilab in 1977.

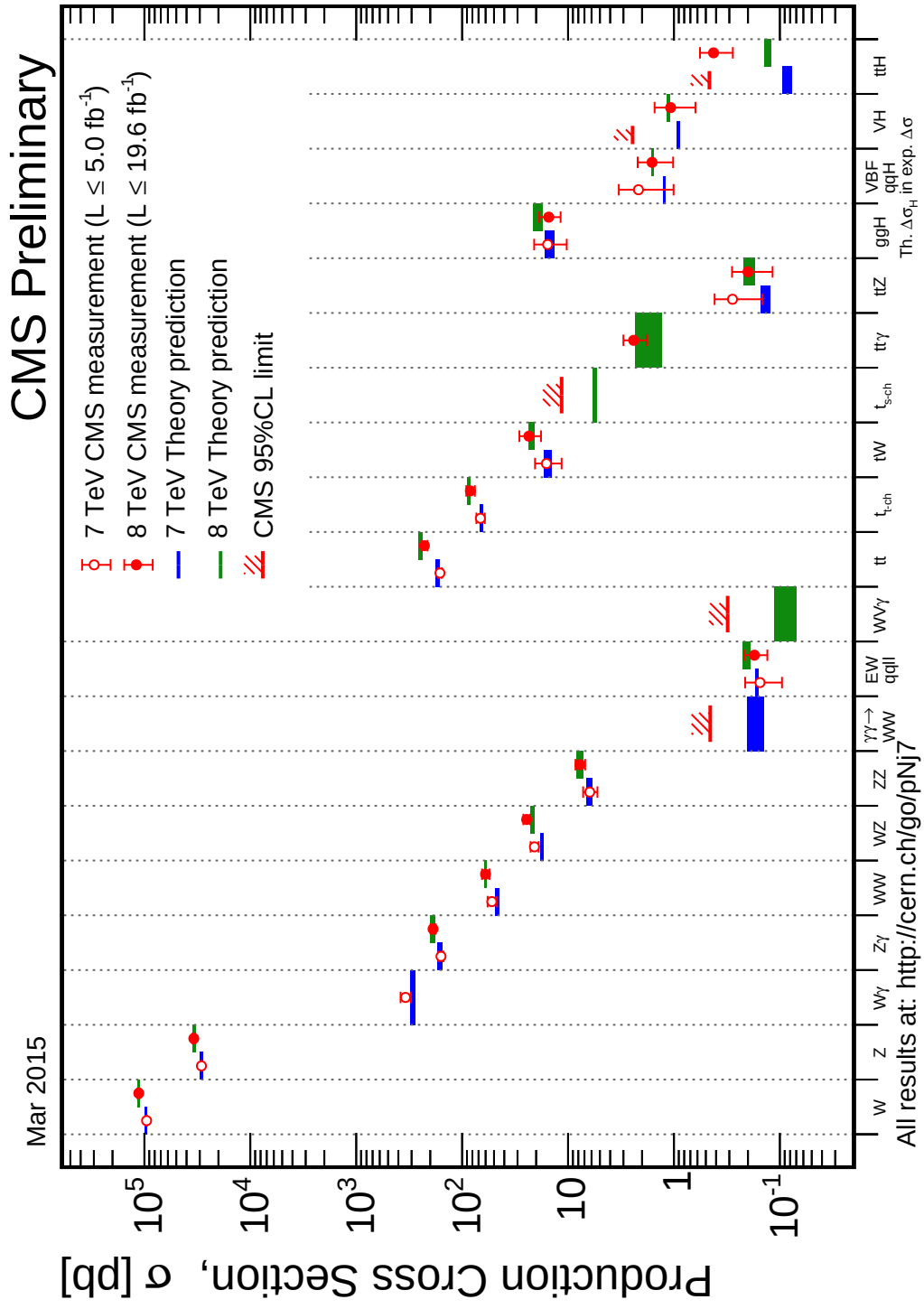

Figure 1.1: Results of CMS tests of SM Production Cross Sections, taken from [7].

$M_W = 80.376 \pm 0.033$ GeV) and derived quantities (such as the diquark production cross-section, $24.599 \pm 0.393 \pm 0.182$ pb, compared to SM prediction of 24.215). A summary of this experimental program is given in [5]. Similarly, the BaBaR and Belle experiments (among others) have performed similar tests on heavy flavor particles; a very complete summary is given in [6].

Perhaps the most impressive success of the Standard Model is in its calculation of the anomalous magnetic moment of the electron, one of the best-measured quantities in physics. For example, Hanneke *et al* published in 2010 a measurement [4] showing $g/2 = 1.00115965218073(28)$, quoting a difference from theory of $|\delta g/2| < 8 \times 10^{-12}$.

Chapter 2

Beyond the Standard Model

In the previous chapter we derived the Standard Model Lagrangian, showed how the Lagrangian can be used to make qualitative and quantitative predictions, and then showed various experimental validations of the Standard Model. Here we will take a somewhat more negative view: we will start by listing the shortcomings of the Standard Model and then discuss some alternative models. One such alternative model in particular, supersymmetry, is a key motivation for the experimental work in this dissertation.

2.1 Unexplained Phenomena

Despite the experimental successes previouly enumerated, it must be recognized that the Standard Model cannot possibly be complete. Here we will list its major shortcomings.

First, gravity. The problem with gravity in the Standard Model is that there isn't any gravity in the Standard Model. The Standard Model does account for particle mass, but it does not predict any innate attraction between massive particles, nor does it predict any curvature in the underlying vacuum. There is a well-developed Theory of General

Relativity that seems to describe gravity correctly, but as yet there is no definitive way to merge General Relativity into the Standard Model. Further, the proposed meditator of the gravitational field, the graviton, has never been observed. Research in gravitational physics continues, but such searches are largely divorced from particle physics, both quantitatively and culturally.

Second, neutrino masses. The Standard Model as written does not account for any neutrino masses, yet is is known that neutrinos do have mass. We can try to add neutrino mass as we did with the other fermions; the trouble is that there are no right-handed neutrinos, so the above procedure still leaves the neutrinos massless. It is not currently clear whether this problem should be solved by introducing non-interacting right-handed neutrinos, or whether neutrinos are Majorana (their own antiparticles) and therefore can have mass without right-handed neutrinos. In either case, introducing neutrino mass would introduce several new free parameters into the Standard Model (in particular, the absolute masses of the neutrino eigenstates and the CP-violating phase factor in the neutrino mixing matrix), which are not currently known.

Third, CP Violations. The universe is generally invariant under the product of charge conjugation (C) inversion, in which all electric charges are reversed, and parity (P) inversion, in which all space-time coordinates are reversed. In the SM, some CP violations are allowed in the quark sector under weak decays (due to the complex phase in the CKM matrix) and in the quark sector under strong interactions (if the quark mass phase, or a similar phase in $F^{\mu\nu}$, is nonzero). It is also possible that the neutrino mixing matrix will allow a third source of CP violations in the leptonic sector. However, there are two concerns. First, the strong interactions show no evidence of CP violation at all, despite it being allowed. Indeed, the neutron's magnetic moment is consistent with zero, which

further suggests that there are no CP violations in the strong sector. This is called the strong CP problem: why are these interactions apparently disallowed? Second, the relative cosmological dominance of matter over antimatter is normally explained by CP violation in the early universe. However, it is not clear that these SM sources are sufficient to explain this asymmetry.

Fourth, dark energy. Astronomical evidence suggests that the universe's expansion is accelerating. This expansion term (the "cosmological constant") can be built into the equations of General Relativity, but there is no way to explain this expansion physically: even General Relativity would predict that gravity, as a long-range attractive force, would cause the initial expansion from the big bang to slow over time. This unknown "force" pulling the universe apart is called dark energy.

A few smaller possible objections result from experiments showing possible deviations from the Standard Model. The muon's magnetic moment has been measured to be high by approximately 0.00023%, or about 3.4σ (as opposed to the remarkable agreement in regards to the electron's magnetic moment discussed previously). [13]. Second, the heavy flavor experiments do show excesses in a few channels, see for example **??**

The final objections to the Standard Model that we will consider here are dark matter and naturalness. Due to these problems' bearing on this thesis, we will examine them with considerable detail in the next two sections.

2.2 Dark Matter

Consider a plot of the average centripetal velocity of a gas or star as a function of its distance from the galactic center. Newtonian physics states that this should fall off as 1/sqrt(r), but astronomical evidence (figure 2.1) disagrees.

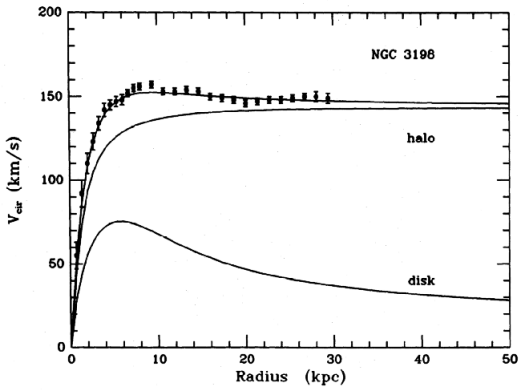

Figure 2.1: Example galactic rotation curve. Figure taken from [9].

Clearly there is some "missing mass" needed to reconcile these results: this is the "halo" plotted in the picture. This halo is not visible, and is therefore named "dark matter."

Though these rotation curves are the most commonly-cited evidence for dark matter, there are many other pieces of evidence. These include gravitational lensing and the Oort discrepency. Mass bends the space around it, modifying the path of photons. This leads to a distortion or "lensing" of the original image. Various lensing patterns can only be explained by the presence of dark matter. The Oort discrepency states that in the Milky Way disc, the gravitational potential cannot be reconciled with the observed presence of stars. Additional evidence comes from the anisotropy of the cosmic microwave background.

The logical candidate for the dark matter is simply neutrinos, but neutrinos are a candidate only for "hot" dark matter (ultra-relativistic velocities in the early universe), whereas "simulations of structure growth from the initial conditions predicted by inflationary models for such a neutrino-dominated universe demonstrated that these ideas lead to a universe quite unlike the one we see around us." [15] The two most likely remaining candidates have been dubbed WIMPs and MACHOs. MACHOs are normal particles arranged into invisible objects; however, standard Big Bang Nucleosynthesis Theory shows that the universe could not produce enough baryons to produce the MACHOs necessary to account for the dark matter without simultaneously producing a spectrum of chemical abundances inconsistent with observation [16]. The remaining likely candidate is therefore a WIMP (a weakly-interacting massive particle). Directly observing a WIMP is an urgent goal of modern particle physics.

2.3 Naturalness

The final objection to the Standard Model that we consider here is naturalness. To first order, the mass of the Higgs Boson is given by equation (1.90). In terms of diagrams, this is one diagram with only the vertex, so:

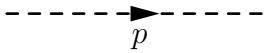

Figure 2.2: Tree-level Higgs Mass

with amplitude:

$$\mathcal{M} = \frac{M_H}{2} \tag{2.1}$$

Let us now consider a loop-level correction to the Higgs Mass, given by the following Feynman Diagram:

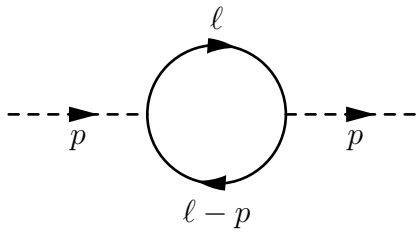

Figure 2.3: Loop-level Higgs mass

Using the Standard Feynman Rules, the amplitude of this diagram is given by:

$$\mathcal{M} = -\int \frac{d^4\ell}{(2\pi)^4} \left(\frac{i\lambda_F}{\sqrt{2}}\right)^2 i^2 \ \mathrm{Tr}\left[\frac{\not{\ell} + m_F}{\ell^2 - m_F^2} \cdot \frac{\not{\ell} + \not{p} + m_F}{(\ell + p)^2 - m_F^2}\right] \tag{2.2}$$

Now we use Feynman's Formula[1] to combine the denominators. This gives:

$$\mathcal{M} = -\frac{\lambda_F^2}{2} \int_0^1 dx \int_0^\Lambda \frac{d^4\ell}{(2\pi)^4} \frac{\mathrm{Tr}\left[(\not{\ell} + m_F)(\not{\ell} + \not{p} + m_F)\right]}{[(\ell + px)^2 - \Delta]^2} \tag{2.3}$$

where $\Delta = p^2x^2 - p^2x - m^2$. Redefine $\ell \to \ell - px$:

$$\mathcal{M} = -\frac{\lambda_F^2}{2} \int_0^1 dx \int_0^\Lambda \frac{d^4\ell}{(2\pi)^4} \frac{\mathrm{Tr}\left[(\not{\ell} - \not{p}x + m_F)(\not{\ell} - \not{p}x + \not{p} + m_F)\right]}{[\ell^2 - \Delta]^2} \tag{2.4}$$

There are many formulas that allow us to simplify the trace[2]; applying these simplifies the amplitude to:

$$\mathcal{M} = -2\lambda_F^2 \int_0^1 dx \int_0^\Lambda \frac{d^4\ell}{(2\pi)^4} \frac{\ell^2 - p^2x(1-x) + m_F^2}{[\ell^2 - \Delta]^2} \tag{2.5}$$

[1] See equations 14.9-14.11 of [3] for an explanation of Feynman's Formula. For a proof, see problem 14.1 of [3].

[2] See section 47 of [3].

Now for the integral over ℓ. Let's do the angular part first[3]:

$$\mathcal{M} = -\lambda_F^2 \int_0^1 dx \int_0^\Lambda \frac{d|\ell|}{(2\pi)^2} \cdot \frac{\ell^5 - p^2 x(1-x)\ell^3 + m_F^2 \ell^3}{[\ell^2 - \Delta]^2} \tag{2.6}$$

Let's keep only the leading term in Λ. This makes the math a lot easier:

$$\mathcal{M} = -\frac{\lambda_F^2}{4\pi^2} \int_0^\Lambda d|\ell|\ell \tag{2.7}$$

which is:

$$\mathcal{M} = -\frac{\lambda_F^2}{8\pi^2}\Lambda^2 \tag{2.8}$$

so the Higgs mass from the tree-level and loop-level diagram is:

$$M_H^{phys} = M_H - \frac{k\lambda_F^2}{4\pi^2}\Lambda^2 \tag{2.9}$$

where k is the number of fermions that can bind (there are additional, smaller corrections from the terms we dropped in equation (2.6)).

Now Λ is the cutoff; the value beyond which we do not expect our Feynman rules to hold because gravity will be nonnegligible. This is normally taken as the Planck mass,[4] the maximum mass for a point particle. Now $M_P = 1.22 \times 10^{19}$ GeV,[5] so this correction to the Higgs mass is on the order of 10^{38} GeV.

The Higgs mass itself is only 125 GeV, so the bare mass must also be of order 10^{38} GeV, and the cancellation is almost perfect (even taking into account the higher order

[3]See equation 14.23 and problem 14.2 of [3].

[4]It could also be taken as the scale of new physics, a few orders of magnitude lower, but the point is the same.

[5]We use natural units here, in which mass and energy are equivalent

terms). It is highly *unnatural* that two enormous quantities should happen to cancel perfectly over 38 orders of magnitude. This is the naturalness problem, and though it could just be a "coincidence," it seems much more likely that there is an underlying, unappreciated symmetry that causes this near-perfect cancellation.

2.4 Supersymmetry

So now that we understand the problems with the Standard Model, we turn to the solution. One possible solution is Supersymmetry.

Theory

Supersymmetry is a theory that posits the existence of a new "superparticle" to partner with every known particle. These partner particles have the same charge and mass; but different spin, such that bosons are mapped to fermions and vice-versa. Since superparticles have not already been observed, the symmetry must be broken, meaning that the masses of the superparticles do not correspond to the mass of their partner. Doubling the number of known particles might seem like an extreme solution, but it may be worth it because supersymmetry is a necessary condition for most theories that add gravity to the Standard Model. Beyond that, supersymmetry could solve the problems of naturalness and dark matter.

For many supersymmetric models, it makes sense to adopt a principle of R-parity conservation, which states that normal particles have $R = 1$, supersymmetric particles have $R = -1$, and the product of the R-parities is conserved. This symmetry, though obviously unproven, is desirable because it maintains baryon and lepton number conservation even in a supersymmetric extension to the SM. If R-parity is conserved, it follows that

the SUSY particle ("sparticle") with the minimum mass must be stable, as no decay could preserve R-parity. We further expect this particle to be electrically neutral, as it would have been observed already if it interacted electromagnetically. This lightest stable particle (LSP) is a candidate for dark matter.

As for naturalness, the inclusion of SUSY vertices would admit corrections to the Higgs Mass as shown in figure 2.4. Now each of these new terms "naturally" cancels with the terms from equation (2.8), and the naturalness problem is solved. In fact, things do not work out so neatly because λ_F (the mass term from the SM Lagrangian) depends on the fermion's mass, and the sparticles do not have the same mass as the corresponding particle. Nonetheless, the degree of naturalness could be significantly reduced if the most significantly unnatural correction (the top loop) could cancel to a significant degree with the corresponding stop loop. Quantizing the "degree of acceptable unnaturalness" is poorly-defined, but it is widely agreed that SUSY will satisfactorily resolve the naturalness problem only if the masses of the stop, higgsino, and gluino are not too far above $\sim$1 TeV ([19]).

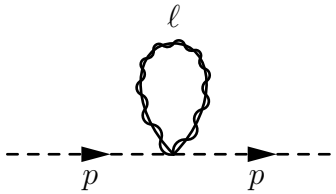

Figure 2.4: SUSY correction to the Higgs mass

Notation

Supersymmetric partners to the fermions are called sfermions (stop squarks, slectrons, etc), while the supersymmetric partners to the bosons are called bosinos (higgsino, wino,

photino, etc). Such "sparticles" are normally marked with a tilde, as the smuon ($\tilde{\mu}$), and the antisparticles are marked with an asterisk, as the anti-sup squark ($\tilde{u}^*$).

It is important to note that in the Higgs doublet (equation (1.70)), there are four degrees of freedom, but three are "eaten" to give the W and Z their mass. In the minimum possible extension to the SM (MSSM), the degrees of freedom double to become 8, but still only three are eaten (remember the wino and zino are fermions and require only two degrees of freedom even when massive). There are therefore five Higgs particles in the MSSM: the SM Higgs (h) and four higgsinos. Of the higgsinos, two give mass to up-type quarks ($\tilde{h}_u^0$ and $\tilde{H}_u^+$) and two give mass to down type quarks ($\tilde{h}_d^0$ and $\tilde{H}_d^-$).

Finally, the charged bosinos ($\tilde{H}^\pm$ and $\tilde{W}^\pm$) have identical quantum numbers, and can mix with each other, forming the "charginos." Similarly, the zino, photino, and neutral higgsinos can mix to form the charginos. These are denoted $\chi^0_{1,2,3,4}$ and $\chi^\pm_{1,2}$, respectively.

Finally, we must note that the partner to the left-handed fermion (ie $\tilde{e}_L$)[6] and the parner to the right-handed fermion (ie $\tilde{e}_R$) are both bosons with the same quantum numbers, and can therefore mix as well. The selectrons, for example, are labelled $\tilde{e}_1$ and $\tilde{e}_2$, where $\tilde{e}_1$ has the lower mass.

Simplified SUSY Models

Even the MSSM increases our number of free parameters to 120. Such a large number makes searches impractical; moreover, a very high fraction of the phase space is already ruled out by current measurements. The pMSSM (p for phenomenological) reduces the

[6]Remember that the L refers to the handedness *of the particle*, not the sparticle. A sfermion has spin-0 and therefore does not have any handedness.

number of additional parameters from 120 to 19. However, it is not easy to interpret search results even in the context of the pMSSM, as any negative result will show only a stricter exclusion band in the 19-dimensional phase space!

The solution is "simplified SUSY models" (see table 2.1) – specific SUSY processes consistent with the MSSM that require only 1-3 free parameters. For example, one popular simplified model (T1tttt) specifies that two gluinos will be produced, each of which decays to two top quarks and an LSP. Such a model has only two free parameters: the masses of the gluino and of the LSP. The trade-off is that many assumptions have been made: in particular, the branching ratio is assumed to be a certain number (usually 100%) and the other sparticles are "decoupled" – their mass is assumed to be so high that they do not affect the process. It is unlikely that any of the simplified models are exactly correct, but it is possible to use enough simplified models that we can span the space of interesting MSSM processes. If a search sees no excess above SM backgrounds, and all simplified models exclude the production of sparticles with a mass below a few TeV, then it is at least unlikely that SUSY exists on any mass scale that can resolve the naturalness problem.

2.5 Alternatives to Supersymmetry

Supersymmetry is perhaps the most widely-accepted of the proposed extensions to the Standard Model, but there are other options. These include (but are not limited to!):

- Extra dimensions. The universe could have a dimensionality larger than four, with the extra dimensions being "compactified" with a radius typicaly taken to be close to the Planck scale. These extra demensions could be "universal", meaning that all fields affect all dimensions symmetrically; alternatively, the Standard Model could

Model	Prod. Mode	Decay
T1	$\tilde{g}\tilde{g}$	$\tilde{g} \to q\bar{q}\ \tilde{\chi}_{LSP}$
T1tttt	$\tilde{g}\tilde{g}$	$\tilde{g} \to t\bar{t}\ \tilde{\chi}_{LSP}$
T1bbbb	$\tilde{g}\tilde{g}$	$\tilde{g} \to b\bar{b}\ \tilde{\chi}_{LSP}$
T2	$\tilde{q}\tilde{q}^*$	$\tilde{q} \to q\tilde{\chi}_{LSP}$
T2tt	$\tilde{t}\tilde{t}^*$	$\tilde{t} \to t\tilde{\chi}_{LSP}$
T2bb	$\tilde{b}\tilde{b}^*$	$\tilde{b} \to b\tilde{\chi}_{LSP}$
T3W	$\tilde{g}\tilde{g}$	$\tilde{g} \to q\bar{q}\tilde{\chi}_{LSP}$
		$\tilde{g} \to q\bar{q}\tilde{\chi}_1^{\pm}$, $\tilde{\chi}_1^{\pm} \to W^{\pm}\tilde{\chi}_{LSP}$
T3ℓH	$\tilde{g}\tilde{g}$	$\tilde{g} \to q\bar{q}\tilde{\chi}_{LSP}$
		$\tilde{g} \to q\bar{q}\tilde{\chi}_2^0$, $\tilde{\chi}_2^0 \to \ell^+\ell^-\tilde{\chi}_{LSP}$
T5ZZ	$\tilde{g}\tilde{g}$	$\tilde{g} \to q\bar{q}\tilde{\chi}_2^0$, $\tilde{\chi}_2^0 \to Z\tilde{\chi}_{LSP}$
T5$\ell\nu$	$\tilde{g}\tilde{g}$	$\tilde{g} \to q\bar{q}\tilde{\chi}_1^{\pm}$, $\tilde{\chi}_1^{\pm} \to \ell\nu\tilde{\chi}_{LSP}$
T5gg	$\tilde{g}\tilde{g}$	$\tilde{g} \to q\bar{q}\tilde{\chi}_2^0$, $\tilde{\chi}_2^0 \to \gamma\tilde{\chi}_{LSP}$
T5Wg	$\tilde{g}\tilde{g}$	$\tilde{g} \to q\bar{q}\tilde{\chi}_2^0$, $\tilde{\chi}_2^0 \to \gamma\tilde{\chi}_{LSP}$
		$\tilde{g} \to q\bar{q}\tilde{\chi}_1^{\pm}$, $\tilde{\chi}_1^{\pm} \to W^{\pm}\tilde{\chi}_{LSP}$
T6ttWW	$\tilde{b}\tilde{b}^*$	$\tilde{b} \to t\tilde{\chi}^-$, $\tilde{\chi}^- \to W^-\tilde{\chi}_{LSP}$
TChiSlepSlep	$\tilde{\chi}_1^{\pm}\tilde{\chi}_2^0$	$\tilde{\chi}_2^0 \to \ell^{\pm}\tilde{\ell}^{\mp}$, $\tilde{\ell} \to \ell\tilde{\chi}_{LSP}$
		$\tilde{\chi}_1^{\pm} \to \nu\tilde{\ell}^{\pm}$, $\tilde{\ell}^{\pm} \to \ell^{\pm}\tilde{\chi}_{LSP}$
TChiWZ	$\tilde{\chi}_1^{\pm}\tilde{\chi}_2^0$	$\tilde{\chi}_1^{\pm} \to W^{\pm}\tilde{\chi}_{LSP}$, $\tilde{\chi}_2^0 \to Z\tilde{\chi}_{LSP}$
TchiZZ	$\tilde{\chi}_2^0\tilde{\chi}_3^0$	$\tilde{\chi}_2^0$,$\tilde{\chi}_3^0 \to Z\tilde{\chi}_{LSP}$

Table 2.1: Partial list of simplified models. This table adapted from [18].

be correct on a physical 4-brane, while gravity and other terms could extend to the alternative dimensions. [20].

- Left-right symmetric models. Rejecting the weak force's apparent preference for left-handed particles, left-right symmetric models predict that right-handed particles can undergo weak decay, but the symmetry is broken at low energies due to the vacuum expectation value of the new particles. Most of these models predict many (as many as 10) additional Higgs Bosons. [21].

- Higgs triplet models. Rather than solving the mass problem with a single Higgs particle, it is possible to solve it by using a triplet of Higgs particles. This has the advantage of allowing violation of lepton number. [22].

- Little Higgs models. A broken SU(5) symmetry provides a large number of Higgs bosons, one of which will naturally have a low mass; the others will solve the naturalness problem. [23].

- Technicolor. A new strong interaction (technicolor) could bind new massless "technifermions" eliminating the need for scalar fields and thereby solving the naturalness problem. [24].

2.6 Searches for New Physics

The unsolved phonemena described in this chapter motivate searches for beyond the Standard Model (BSM) physics. Such searches are divided between the so-called cosmic, intensity, and energy frontiers.

Cosmic Frontier

The questions of dark matter and dark energy are studied on the cosmic frontier. Further, the cosmic frontier studies cosmic rays, which are good natural sources of very high-energy particles. There are many experiments at the cosmic frontier; here we will select only a few examples. As an arbitrary metric, we will describe only those experiments funded by the US Department of Energy (DoE).

The LUX, CDMS, and DarkSide experiments are examples of "direct detection" dark matter searches. The LUX collaboration, for example, maintains a well-shielded xenon tank and searches for photons produced from DM interactions with the xenon. ADMX searches for axions. Axions are hypothetical particles predicted by the Pecci-Quinn Mechanism in order to solve the Strong CP problem. As a massive and invisible particle, the axion is also a dark matter candidate. ADMX operates a resonance cavity at various frequencies in order to stimulate energy deposits from the axions.

On the dark energy side, the strategy involves using telescopes to make maps of the large-scale structure of the universe in order to determine the universe's rate of expansion, both past and present. This is studied independently using several different telescopes in the BOSS, LSST, and DES experiments.

Finally, experiments such as HAWC, AMS, and FGST study gamma rays. Most of the interest in gamma rays is astrophysical, but these experiments are also configured to search for massive new particles.

Intensity Frontier

The intensity frontier is named because of its experiments' requirement for a very high intensity source; the energy is less of a concern, being either relatively low or naturally-provided (ex: solar). In particular, many of the questions at the intensity frontier involve neutrinos: their absolute mass, oscillation parameters, and whether the neutrino is a Majorana or a Dirac particle. We will again consider only those funded by the DoE, except where indicated.

Oscillation experiments normally have a neutrino beam fired through a near detector and a far detector. The flavor composition of the neutrinos are compared between the two detectors, which allows constraints on the parameters of the mixing matrix to be set. This facilitates the determination of the mixing parameters: the mass difference between the different neutrino mass eigenstates, the mixing angles, and the CP-violating phase factor. The DoE is currently funding MINOS, T2K, Super-K, NOvA, MiniBoone, DUNE, and Daya Bay to do this type of research.

The remaining neutrino-related questions are addressed by "direct detection" experiments. The DoE funds EXO-200, which searches for neutrinoless double beta decay: two protons undergoing simultaneous beta decay, with both W^- particles undergoing a t-channel interaction (mediated by a neutrino), to produce two electrons. Observing this process would prove that neutrinos are Majorana particles (to locally conserve lepton number) and prove that global lepton number is not a conserved quantity. Since the process amplitude is proportional to the neutrino mass, this would facilitate the determination of the effective absolute neutrino mass. Katrin pursues an alternative approach, attempting to bound the absolute neutrino mass by studying the tail of the energy spec-

trum of the three-body tritium decay at high-precision[7]. Further, Minerva measures various neutrino-matter cross-sections.

Finally, a few experiments at the intensity frontier search for evidence of very rare phenomena that are predicted by many extensions to the stanard model. This include searches for the $\mu \rightarrow e$ process (Mu2E) as well as CP violations and matter-antimatter asymmetries (Belle and KOTO), and better measurements of the anomolous muon magnetic moment (g-2).

Energy Frontier

On the energy frontier, particle beams are used to produce very high energy collisions in the center of a detector. In this way, the initial state is clearly known (two protons, for example) and the intensity is such that millions of collisions can be generated every second. The term "energy frontier" refers to the challenge: considerable financial resources and technology must be deployed to achieve a sufficiently high energy (13 TeV is the maximum at the present time).

Currently there is only one high-energy particle collider worldwide, the Large Hadron Collider in Geneva.[8] However, the LHC consists of several experiments. These include:

- ALICE studies the quark-gluon plasma (a state of matter where quarks and gluons are not bound to each other), which will allow a more complete theory of QCD.
- LHCb studies b-quark physics, including CP-violations and forward/backward asymmetry in the b-sector.

[7]Katrin, however, is not a DoE experiment and is listed only for completeness.

[8]There are many other colliders used for medicine and research, but these are much lower energy and so are useful only at the intensity frontier. For example, RHIC operates at less than $\sqrt{s} = 1$ TeV per nucleon.

- TOTEM studies the total cross-section from proton-proton collisions.
- LHCf analyzes the very forward part of the collisions in order to simulate cosmic rays (the advantage being that unlike real cosmic rays, we have information on the initial collision).
- MOEDAL searches for magnetic monopoles or other maximally-ionizing charged particles produced by the LHC.

The final two detectors, ATLAS and CMS, are general purpose detectors designed primarily to search for the Higgs boson and for any possible signature of BSM physics. The work for this dissertation was conducted with the CMS detector, so it is worth discussing its properties in some details. We turn to this now.

Chapter 3

The CMS Experiment

We have now considered in detail the motivation for the experimental work presented in this dissertation. However, the data collected for this dissertation were collected as part of the Compact Muon Solenoid (CMS) experiment, which receives its beams from the Large Hadron Collider (LHC). In this chapter we will describe the LHC and the CMS experiment in some detail.

3.1 The Large Hadron Collider

The fundamental idea of the CMS experiment is that proton-proton collisions at a high enough energy can lead to interactions. The interactions derived in chapter 1 have already been seen in similar experiments (except some of the Higgs couplings), but the hope is that new vertices (perhaps involving new particles) can be seen if the energy is increased sufficiently.

The protons used for collisions are initially stored in hydrogen gas, but the first step is to use an electric field to remove the electrons so that only the protons are accelerated.

The protons then enter a chain of accelerators: first a linear accelerator that increases their energy to 50 MeV, then a series of synchotrons which increase their energy to 6.5 TeV.[1] Two identical beams of protons thus accelerated are allowed to interact at the center of the CMS detector (and also at the center of three other detectors), resulting in center of mass ($\sqrt{s}$) energy of 13 TeV.

A synchotron by definition accelerates the particles while providing a centripetal acceleration on each proton sufficient to keep the protons from leaving the synchotron. As the particles reach higher energies, the magnitude of this magnetic field must increase. CMS uses 1,232 dipole magnets to do this steering of the beam. Each dipole magnet is superconducting (and must therefore be kept at a temperature of 1.9 K) and produces a magnetic field as high as 8 T. Note that since the protons move in opposite directions, each beam must have its own set of magnets. An additional 392 quadrupole magnets are used to reduce the transverse size of the beam. To prevent beam-gas collisions, the beam is kept in a near-vacuum of approximately 10^{-13} atm.

The magnets are not themselves responsible for the particle acceleration (magnets do no work; they cannot apply a force in the direction parallel to the motion). The actual acceleration comes from 16 radiofrequency (RF) cavities placed throughout the accelerator. These cavities create a potential difference that oscillates at 400 MHz. In this way, the protons are separated into bunches separated by 25 ns: protons that arrive early or late relative to the center of the bunch receive a slightly different field strength that compensates for their earliness or lateness. The RMS "length" of each bunch is approximately 7 cm (for reference, a 25 ns bunch spacing means that the center of two adjacent

[1] Technically the LHC is only the last (and largest) accelerator in this chain, but in common parlance, it refers also to the entire acceleration complex.

bunches are separated by approximately 7.5 m).

Design Considerations

It is worth considering the motivation of the design choices: in particular: why protons, why colliding beams, and why circular? The choice for circular is simply that a circular design allows the particles to cycle through the same accelerator millions of times prior to collision, while a given particle could only pass through a linear collider once. Circular colliders (synchotrons) therefore dramatically increase the maximum energy that can be reached on a given budget.

As for what to collide, it is necessary to consider the radiative losses that the beam will undergo. The relativistic Larmor formula gives the energy that will be lost by the beam due to radiation (in SI units) as:

$$P = \frac{2Ke^2\gamma^4v^4}{3c^3r^2} \tag{3.1}$$

The power lost to radiation is therefore proportional to the fourth power of $\gamma = E/m$. For a 6.5 TeV proton, gamma is 6930; for an electron of the same energy, it is ∼12.7 million. In one revolution, this formula shows that a proton would lose ∼3.8 keV, while an electron would lose ∼3.3 TeV.[2] This clearly rules out electrons or any other light particle.

Given this, the proton is a logical choice: it is heavy, stable, abundant, electrically charged, and cheap. The one drawback is that it is a composite particle: the actual partons that undergo the interactions will not individually have the entire 6.5 TeV, nor

[2]Of course, the actual power lost would be less than this because the electron's Lorentz factor would decrease as the electron radiated energy, but the point is clear.

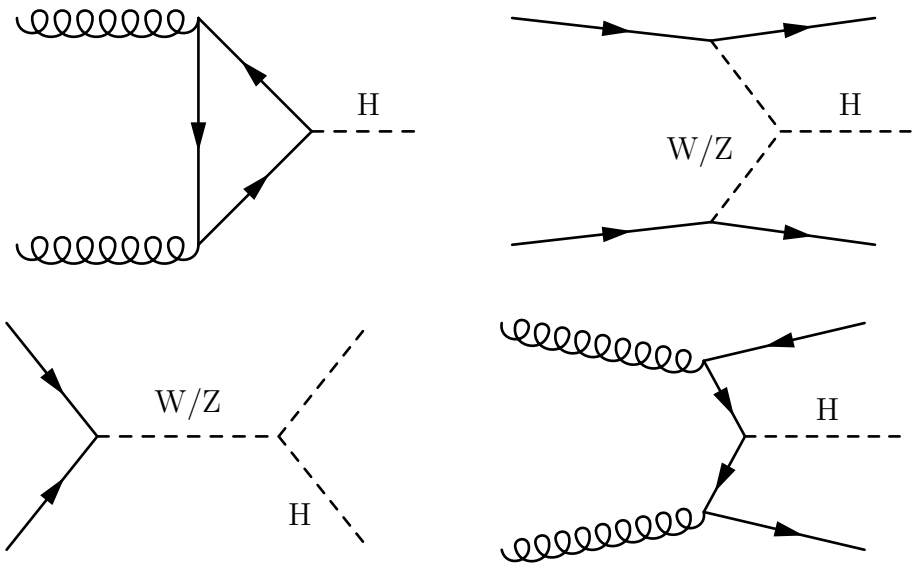

Figure 3.1: Most significant Higgs production modes.

can the exact energy of a given parton be calculated. Given this, the alternative of creating a lepton-based linear collider is attractive: each interacting lepton would have an exactly-known energy equal to the nominal energy. Therefore, the design energy of a linear collider could be considerably lower in order to achieve competitive results. The decision to use a synchotron with protons was motivated by the desire to find the Higgs: the Higgs production modes (figure 3.1) and expected energy scale made such a setup more cost-effective. However, there is some interest in building an "International Linear Collider" in the coming years.

It is also worth noting that the power lost by synchotron radiation is proportional to r^{-2}; this loss is mitigated by the LHC's very large (27 km) circumference.[3]

As for colliding beams, it is purely a question of energy. In a colliding-beam experi-

[3]However, the key advantage of such a size is that magnets need to be used to steer the protons: a smaller radius would require more powerful magnets than could be built at the time of construction.

ment, the center of mass frame is the lab frame. Therefore:

$$p_1 = -p_2 = (E_{cm}, \vec{p}_{cm}) \implies p_1 + p_2 = (2E_{cm}, 0) \implies s = 4E_{cm}^2 \tag{3.2}$$

where p_1 and p_2 are the four-momenta for the two beams. Conversely, in a fixed-target experiment, the center of mass frame is different than the lab frame. In the lab frame, we have:

$$p_1 = (E_1, \vec{p}); p_2 = (M, 0) \implies p_1 + p_2 = (E_1 + m, \sqrt{E_1^2 - M^2}) \implies s = 2E_1 m + 2M^2 \tag{3.3}$$

where M is the mass of the particles being collided. Thus, two colliding beams can reach $\sqrt{s} = 13$ TeV if the beam energy is 6.5 TeV. In contrast, a fixed-target experiment would require a beam energy of nearly 90 PeV to get the same results, which is certainly impossible.

A final design consideration is the location: the LHC is operated by CERN, so it is in Geneva. It was placed underground primarily to minimize costs (the huge circular tunnel already existed from a previous accelerator, whereas buying 58 square kilometers of land near Geneva on which to place the detector would be cost-prohibitive), though there is also a benefit from the natural radiation shielding.

Luminosity

Our discussion until this point has used only one figure of merit, the beam energy. However, there is another important consideration: luminosity, which relates the cross-section to the event rate.

$$\text{event rate} = L\sigma \tag{3.4}$$

From figure 3.2, we quantify the luminosity as:

$$L = \frac{N^2 n_b f}{A_{\text{eff}}} \tag{3.5}$$

Where N is the number of protons in each bunch and n_b is the number of bunches in each beam, f is the frequency of the beam crossings, and A_{eff} is the effective area of the beam: given the beam circumference and a speed of essentially c, the frequency works out to about 11245 hz. The number of particles in each beam is about 1.2×10^{11}, and there are about 2388 bunches per beam.

The "transverse width" of the beam at the interaction point is approximately 17 μm for the LHC. Approximating the beam as a Gaussian, we take the effective area to be $4\pi\sigma_x\sigma_y = 3.63 \times 10^{-5}$ cm^2. The effective area also receives a small correction because the beams are not entirely head on at the collision point, but are separated by approximately 290 μrad. We neglect this correction in this discussion. Given these parameters, the LHC luminosity is approximately 1.06 $\times 10^{34}$ cm^{-2} s^{-1}. These parameters were not constant over the LHC run; the numbers given here are an approximate estimate only.

By integrating the luminosity over time (calculating the "integrated luminosity") and multipyling the result by the cross-section for the process in question, we can quantify the expected number of events for any given process. The total cross-section is approximately 10^{-25}cm^2 (100 mbarn)[4], so we expect approximately a billion events per second.

[4]Number taken from [34] at 7 TeV; the inelastic portion is confirmed by ATLAS to be essentially unchanged at 13 TeV, see [35].

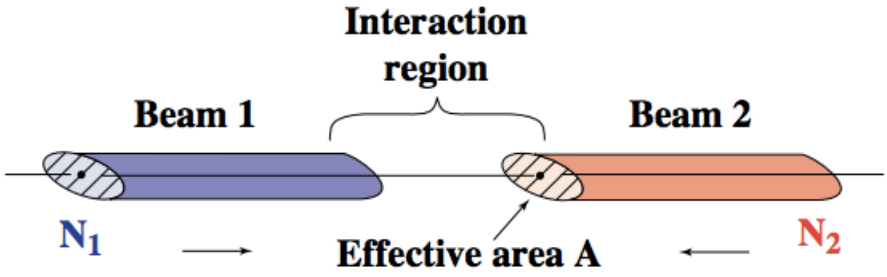

Figure 3.2: Schematic of LHC collisions. Taken from [32].

Beam Width

It is obviously desirable to have a beam that is as small as possible at the collision point. However, the details of the accelerator require that we do not keep the beam at a minimum size at all times. For this reason, focusing and unfocusing quadrupole magnets are applied before and after each of the interaction points.

Beam width is largely quantified through three parameters: β^*, emittivity, and width. β^* gives the distance the beam must travel until its width doubles. For the LHC, this is approximately 60 cm. The (RMS) beam width can be quantified as the size of the beam in the x- or y-direction. The emittivity is related to the other two by the relation:

$$\sigma_{RMS} = \sqrt{\beta^* \varepsilon} \tag{3.6}$$

The physical interpretation of the emittivity is the (constant) size of the beam in the position-momentum parameter space. This is one of the three "Twiss Parameters", which exceed the scope of this discussion.[5]

[5]See [29] for further discussion.

Parton Distribution Functions

We discussed previously the choice to collide protons, and mentioned that the disadvantage of composite particles such as protons is that the fraction of the proton's energy possessed by each of the three quarks is not unity, nor is it simply one-third. Rather, it is determined by the parton distribution function (PDF), a function f(x, Q^2) that gives the probability of finding a parton with momentum fraction x at the parton-parton center of mass energy Q^2. An example PDF for an interaction with Q^2 of 3.3 GeV and 10 GeV is shown in figure 3.3. The PDF shows that most of the momentum is with the up quarks (and therefore most of the interactions will involve the up quark), while the gluons and sea quarks are supressed by an order of magnitude or more. Initial states involving antiquarks or heavy quarks are therefore heavily PDF-supressed. However, these PDFs are taken into account when the cross-sections are calculated, and so do not need to be discussed further here.[6]

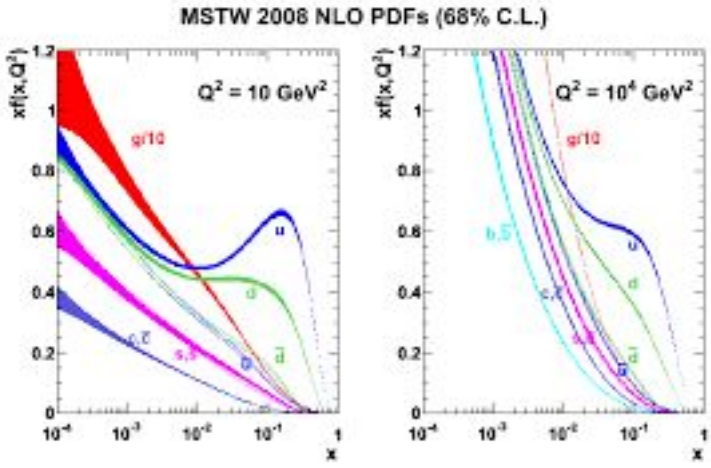

Figure 3.3: Parton distribution function for a proton with $Q^2 = 3.3$ GeV and 10 GeV. Figure taken from [33].

[6]We will, however, discuss the error on these PDFs in section 6.1.

Pileup

We calculated previously that we expect approximately a billion events per second. With 40 million bunch crossings per second, we expect about 25 events on each bunch crossing. This leads to an experimental problem called pile up (PU): how is it possible to separate all the components of each event from the components of other, pileup events? In principle this is not a problem: all the events have different vertices, and the reconstruction software has sufficient granularity to separate the products of each vertex (at least for the charged particles). However, the reconstruction is obviously not perfect and so pileup will be one source of uncertainty at the analysis level.

3.2 Anatomy of the CMS Detector

The CMS detector is composed of several concentric cylindrical components. In the center is the beampipe of the LHC, in which the collisions actually occur. Proceeding outward from the beampipe, we find the tracker, the electromagnetic calorimeter, and the hadronic calorimeter, the magnet, and finally the muon chambers. All of these are subdetectors except for the magnet, whose function is to provide the uniform 3.8 T magnetic field. Due to the cylindrical geometry of the detector, each subdetector has a component along the "barrel" and a component along the "endcap." The design of these two components can be quite different.

CMS uses a right-handed coordinate system in which the counterclockwise proton beam lays along the positive z-direction, the x-axis points from the center of the detector to the center of the LHC, and the y-axis points "up" (perpendicular to the plane of the LHC). This z-component is often called the "longitudinal" direction while the x- and

y-directions are said to make up the "transverse plane." Indeed, since the total momentum of the interacting partons is unknown but the total transverse momentum of the interacting partons is by definition zero, the transverse momentum vector (p_T) is almost always the key variable.

Although the coordinate system described above spans the space, it is more convenient to describe particle momentum vectors using a set of modified cylindrical coordinates. The magnitude of the transverse component is given by p_T, and the angle in the transverse plane is given by ϕ. The remaining variable is θ, the polar angle from the z-axis, but the quantity η ($\eta = -\log\tan\theta/2$), dubbed pseudorapidity, is usually quoted instead.[7]

In the remainder of this section we shall consider the subdetectors individually.

Tracker

The innermost subdetector, the tracker, provides a high-resolution reconstructed trajectory for all charged particles, made completely of silicon. As the charged particles pass through the silicon, they will knock electron-hole pairs loose. This charge is collected and measured at readout electronics, causing the pixel or strip to be "lit." The particle trajectories are reconstructed from the pattern of lit pixels and strips.

There are five main design considerations for the tracker. First, the material used must be low to limit the efects of multiple scattering, bremssstrahlung, photon conversion,

[7]Pseudo-rapidity, $\eta = \text{arctanh}(p_L/|\vec{p}|)$, is an approximation of rapidity, $y = \frac{1}{2}\ln\left(\frac{E+p_L}{E-p_L}\right)$, with the advantage that pseudo-rapidity depends only on the polar angle. Pseudo-rapidity is generally preferred to the polar angle because particle production is essentially constant as a function of η; further, differences in rapidity (and therefore, approximately, under pseudorapidity) are invariant under boosts along the beam axis.

and nuclear interaction. Second, the electronics must offer good resolution so that it is possible to accurately reconstruct the trajectory. Third, the electronics must be fast: both so that the hits can be recorded before the next bunch crossing and passed to the trigger system. Fourth, the tracker will be subject to intense radiation damage: approximately 1000 particles per bunch crossing, and a bunch crossing every 25 ns over a ten year period. Finally, the cost must be affordable.

In view of these goals, an all-silicon design was chosen. Of the materials considered by the PDG [36], silicon has the fastest response time and a good radiation hardness at a reasonable cost.

This silicon tracker is divided into two sections, the inner pixel tracker and the outer strip tracker. The pixel detector has excellent resolution: the pixels are 100x150 μm and a given charged particle should give 2-3 hits, so the hit resolution is on the order of 10-20 μm. The outer tracker offers somewhat lower resolution, but offers 10-14 hits per track and has a much lower amount of material than the pixels.

Once the pattern of lit pixels and strips is obtained, it is then necessary to reconstruct the particle trajectories ("tracks"). The two main algorithms for track reconstruction are the Combinatorial Kalman Filter (CKF) and the Gaussian Sum Filter (GSF). These trajectories can then be compared to the results from the other subsystems.

Electromagnetic Calorimeter

Surrounding the tracker is the electromagnetic calorimeter, a cylindrical section filled with crystals extending 23 cm in the barrel and 22 cm in the endcap. These crystals

have a radiation length of 0.89 cm, allowing virtually all the photons and electrons to be fully absorbed (muons are minimally ionizing and therefore leave almost no track in the ECAL). As the electrons and photons pass through, they undergo various types of particle-matter interactions to create showers of many low-energy electrons and photons. The electrons then lose energy by transferring energy to the material, causing the atoms in the crystal to reach an excited state. When these atoms return to the ground state, they emit scintillation light with a characteristic wavelength of approximately 420 nm. Each crystal is then connected to a photodiode that measures the intensity of this light. The light patterns from 3x3 blocks of crystals ("superclusters") are used to detect electrons. The Molière radius of the crystals chosen is only 2.2 cm (exactly the size of the crystal itself), so most of an electron's energy is captured in one supercluster.

The performance requirements for the ECAL are similar to those of the tracker, and are universally met by the choice of lead tungstate as a material for the crystals. As already mentioned, it has a small Moliere radius and radiation length, allowing fine granularity within a relatively small volume of material. Further, it is naturally somewhat radiation hard and the existing radiation damage can be precisely calibrated by periodically measuring the optical transmission of each crystal. When the ECAL is warmed to room temperature, the chemistry of the crystal causes the atoms to naturally "heal themselves", regaining their well-ordered structures (it is however necessary to keep the ECAL refrigerated during running, as the light yield is strongly dependent on the temperature).

Finally, the ECAL has one additional region, designed to distinguish between electrons and the $\pi \to \gamma\gamma$ decay occuring right in front of the ECAL, as these can give very similar signatures. This "preshower detector" consists of two planes of lead followed by high-

granularity silicon sensors; the planes of lead are two and one radiation lengths thick, respectively. Each collision with the lead creates a shower which is then analyzed in the high-granularity silicon region (using the same principles as the tracker). The pattern of energy deposits in this silicon often shows a distinct separation between diphoton events which otherwise would have been indistinguishable. The trade-off is that the preshower detector is only a sampling calorimeter; the energy lost in the lead sections cannot be detected directly. However, its magnitude can be estimated from the other parts of the detector; the resulting performance is not much worse.

Hadronic Calorimeter

On the outside of the electromagnetic calorimeter is the hadronic calorimeter, optimized to detect and absorb hadrons. The principle is similar to that of the preshower region: layers of brass and steel create showers which then pass through a plastic scintillator, creating blue-violet light. This light is then passed through wavelength-shifting fibers to reach the hybrid photodiode (the fiber shifts the wavelength to green, where the photodiode has optimal efficiency).

Geometrically, the HCAL is split into four sections. The barrel and endcap are positioned inside the magnet and absorb most of the hadrons. In addition, the "HO" region is additional material placed outside the magnet in the barrel. This increases the depth of the HCAL to 8-10 interaction lengths, sufficient to stop most hadrons. Finally, the "HF" region is placed outside the magnet in the endcap, to catch hadrons produced at angles close to the beam pipe. The particle rate in this region is much higher and so the detection technology is based on Cerenkov light rather than scintillation; this reduces the radiation damage in this region.

Muon System

In addition to the tracker, muons are detected in a separate, dedicated muon system which lives outside of the magnet and the iron yoke. Almost all other particles are unable to penetrate the iron of the HCAL, magnet, and yoke, so the muon system has a relatively low background. The backgrounds that do exist include:

- Punch-through: non-muons (usually hadrons) that do manage to penentrate the detector, as well as muons produced by the decay of a heavy particle. The rate of punch-through is approximately 5% at the first muon station and 0.2% at further muon stations.
- Environmental neutrons.
- Cosmic muons. Obviously the sub-terranean location helps to mitigate this.

The tracker provides a separate muon detection system, allowing us to distinguish between "tracker muons" ((muons identified by hits in the tracker and propogated to matching hits in the muon chambers) as opposed to "global muons" (muons reconstructed in both the tracker and the muon system and then fit together).

Three different technologies are used for the muon system. The first is the Drift Tubes (DTs) in the barrel, which consist of a series of drift cells containing Ar/CO_2 gas in a tube with a 50 μm diameter gold-plated stainless steel wire in the middle at a potential of 3.6 kV. The muons ionize the gas, forming an avalanche of electrons that collect at the wire. The DTs give a spatial resolution of 100 μm; further, drift cells are strategically positioned to give positions in r-ϕ and r-z, and to sculpt the drift field. However, the drift time is potentially quite long, so the DTs are not suitable for regions with higher occupancy, or with an uneven magnetic field.

For this reason, cathode strip chambers (CSCs) are used in the endcap. The CSCs are distinguished from the DTs because the single positively-charged wire is replaced by a series of positively-charged wires placed perpendicular to a series of negatively-charged strips. The muon will then break the gas particles into an electron and a positive ion, which are attracted to the wires and the strips, respectively. This provides precise two-dimensional position information for each CSC. Further, the strips are placed very close together (3.2 mm spacing, except in the highest occupancy region where they are even closer), so the overall spatial accuracy is as good as $\sim$100 μm. This close spacing substantially reduces the drift time. Finally, six of these planes are stacked, and a muon must leave a hit on at least four of the planes in order to be reconstructed in the layer.

The third is the resistive plate chambers (RPCs), in both the barrel and endcap, which provide a detection algorithm independent of the first two. An RPC consists of a gas placed between two electrodes at a high potential difference. Muons ionize the gas creating an avalanche of electrons. These electrons pass through the electrode to reach the readout strips. The RPCs provide both a decent spatial resolution (about 1 cm) and a good time resolution ($<$ 3ns). This is suitable for the trigger system.

The redundant system is useful because the different components have different strengths and weaknesses with respect to the backgrounds. The CSCs and DTs require multiple hits on multiple layers and so are able to reject much of the neutron and handronic punch-through background. The RPCs have a tight timing window and therefore is not affected by out-of-time pileup.

Triggers

As discussed in section 3.1, the LHC delivers approximately one billion events per second. Even storing the "raw" readout from the detector requires approximately 470 kB/event, for a total of 470 TB/s. Such a scheme is prohibitive: Fermilab, for example, is one of the largest computing centers in the experiment, and it has approximately 30,000 TB of disk storage; this would be filled in one minute! Even the "tape" storage system at Fermilab would be filled in less than an hour. Even beyond storing this much data long-term, there is also the matter of physically copying that much raw data onto disc in real time.

To avoid these problem, a two-tiered trigger system is used to identify those events which meet the criteria for any in a long "menu" of triggers. The first, electronics-based trigger, called the L1 trigger, holds all the data for only 3.2 μs, at which point only 1 in 10000 events can be passed to the second trigger. This second trigger, called the HLT, is an online processor farm which partially reconstructs each event, eventually "triggering" about 1 in 1000 events.

The definition of the triggers must be chosen to reach these desired rates. For example, the run-1 trigger menu required the L1 to select all events possibly containing an electron with $p_T > 5$ GeV, and then triggered on those events where the HLT agreed that the $p_T > 5$ condition was met. This trigger was given a prescale of 50 (only 1 in 50 events was saved). In parallel, there was a second trigger condition with electron $p_T > 8$ with a prescale of 10, and additional trigger conditions for $p_T > 10$ with no prescale. Similar triggers were designed for the other objects.

The triggers therefore reduced the rate from 1 GHz to 100 Hz. The remaining events

were added to the appropriate dataset and the full reconstruction algorithms were applied at CERN: this bloats the size of each event to approximately 1.2 GB each. The unneeded variables are then stripped to create a MINIAOD format, with a size of approximately 20 kB/event. These MINIAOD files are the source for the data presented in this dissertation.

3.3 Detector Performance

To complete our study of the detector, we must consider its efficacy. Rather than considering the resolution and performance of each component separately, it is perhaps more useful for our purposes to show some examples of the overall reconstruction ability of the detector as a whole.

To this end, we will consider a signal simulation sample[8] and compare the generated leptons and jets to the reconstructed leptons and jets. Of course, the simulation's fidelity in modeling the detector performance has not yet been estabished, but we will assume this for now and prove it by showing commissioning plots in later chapters.

We begin by considering the detector's reconstruction efficiency: if the generator produces an electron, muon, or jet, what are the odds that it is reconstructed? For the purposes of this study, we define a generated lepton (jet) to be "reconstructed" if the nearest reconstructed lepton (jet) lies within an angular distance $\Delta R < 0.1$, where ΔR is defined as:

$$\Delta R = \sqrt{\Delta\phi^2 + \Delta\eta^2} \tag{3.7}$$

[8]We used the simplified SUSY model T1tttt (described in table 2.1) with gluino mass of 1200 and LSP mass of 800.

This reconstruction efficiency is plotted as a function of the generated momentum in the transverse plane in figure 3.4.

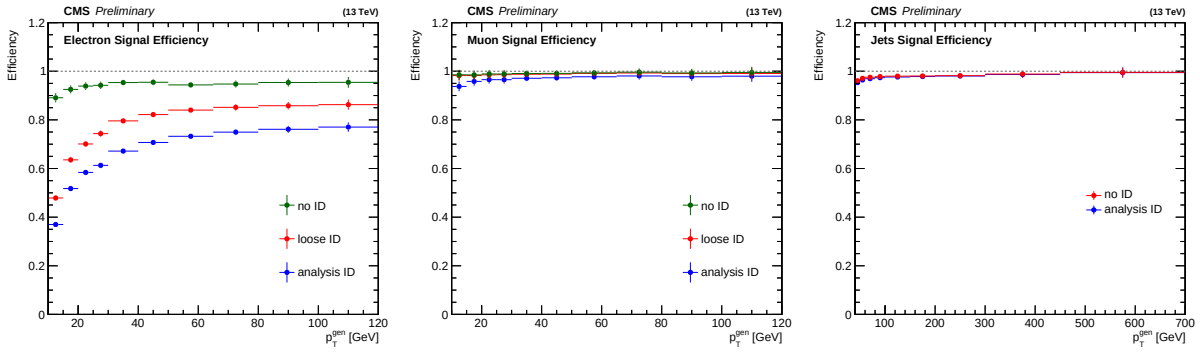

Figure 3.4: Object reconstruction efficiency for electrons, muons, and jets

Each plot is drawn with different ID requirements on the reconstructed objects: "no ID" accepts any reconstructed object added to the appropriate collection, while the "loose ID" accepts only reconstructed objects that pass a mild selection. Similarly the "analysis ID" requires the full identification selection required for the analysis presented in this dissertation (described later); this selection is relatively stringent.

Clearly the detector does excellent work reconstructing muons: they are universally reconstructed correctly more than 90% of the time, and even better at high p_T. This is consistent with our conclusions previously that the detector is well-optimized for muons (due to the tracker and independent muon system). For jets, the results are similar; however we note that the performance improves sharply around 40 GeV. As for the electrons, the agreement is much worse: only 80% of even the high-energy electrons are reconstructed successfully with a loose ID requirement; further, a huge price must be paid for requiring a tighter ID.

The value of the tighter ID becomes clear when examining the mistag rate: the fraction of reconstructed objects that cannot be associated to a generated object (at an angular distance of $\Delta R < 0.1$) of the same flavor, and are therefore "incorrect." This mistag rate is plotted in figure 3.5.

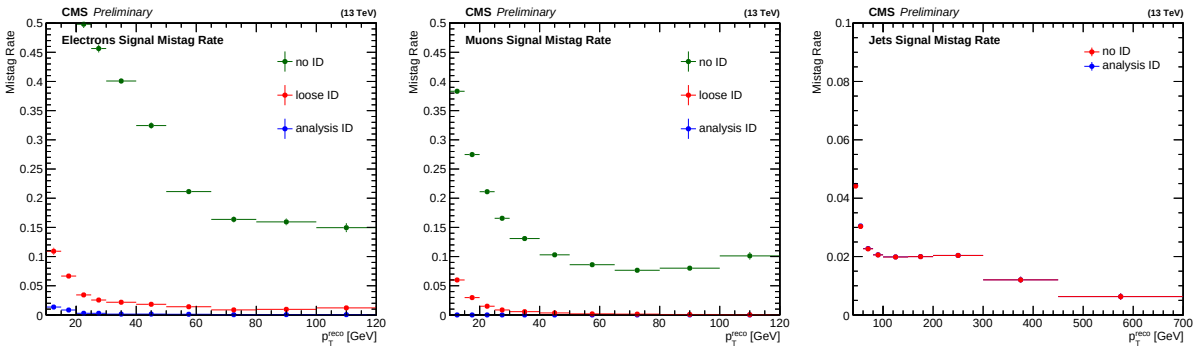

Figure 3.5: Object mistag efficiency for electrons, muons, and jets

The jet mistag rate is low (generally 1-2%); further, both the mistag and efficiency plots show little difference between the "no ID" and "analysis ID"; the analysis jet ID is not very stringent. For electrons and muons, the effect of the ID is clear; the mistag rate falls by over five orders of magnitude in some places.

It is also worth considering the detector's ability to distinguish b-quarks. The detection rate and mistag rate for b-flavored jets is shown below:

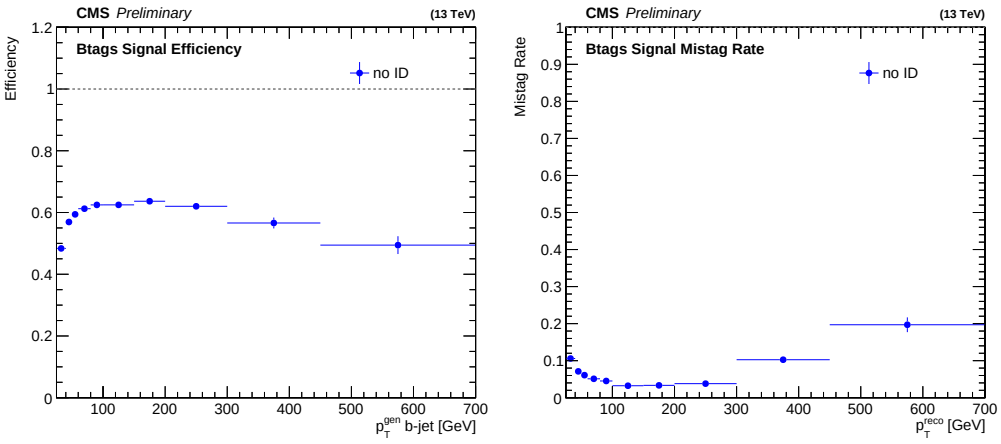

Figure 3.6: B-tagging efficiency and mistag rate

The b-tagging efficiency is defined as the fraction of jets generated within $\Delta R \leq 0.4$ of a b-quark that are reconstructed as a b-tagged jet. This approximately 60%, whereas the mistag rate (the fraction of reconstructed b-tagged jets that do not lie within $\Delta R \leq 0.4$ of a generated b-quark) is approximately 10%.

Finally, we can also consider the momentum resolution: does the reconstructed p_T correspond to the generated p_T? The fractional error in the p_T is shown in figure 3.7:

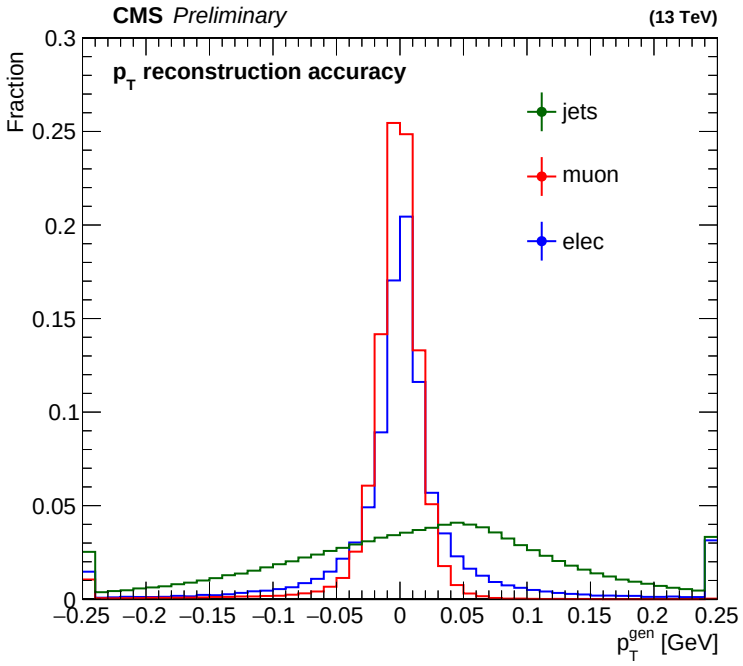

Figure 3.7: p_T reconstruction accuracy for electrons, muons, and jets (these distributions depend on the p_T of the particles being reconstructed; here we use the generated p_T-spectrum for a simplified SUSY model as described previously).

95% of muons and 80% of electrons are reconstructed with a p_T within 5% of the generated value. The jets (even with jet corrections applied) show a much worse energy resolution; however, 81% of jets are reconstructed with a p_T within 20% of the generated value.

We conclude that it is reasonable to do a search that relies on leptons, particularly on muons; the 80+% reconstruction efficiency will give a reasonable acceptance for processes that produce multileptons. Further, the mistag rate is negligible, and the leptonic momentum reconstruction is accurate to approximately 5%. Jets are reconstructed with a high efficiency and with a momentum accurate to approximately 20%; this is sufficient to impose a coarse jet requirement. Similarly, the b-tagging algorithm is certainly sufficient to offer considerable separation between b-tag enriched signals and b-tag de-

pleted backgrounds, but cannot be trusted when a high precision in b-tag multiplicity is required.

3.4 Early Results

We conclude this chapter by briefly summarizing some of the results from the LHC's first run period, in which the beam energy was 8 TeV and the bunch spacing was 50 ns.

The most notable result of course is the observation of the Higgs Boson at a mass of approximately 125 GeV [43]. This is a good confirmation of the Standard Model proposed in chapter 1, as well as a vindication for the experimental design outlined here. Figure 3.8 (left) shows the combined data set showing the level of agreement between the observed Higgs cross-section versus that which would be predicted by theory, given the Higgs mass on the x-axis. The observation and prediction agree only at approximately 125 GeV. Further, figure 3.8 (right) shows that the observed decay modes are not inconsistent with what the Standard Model predicts.

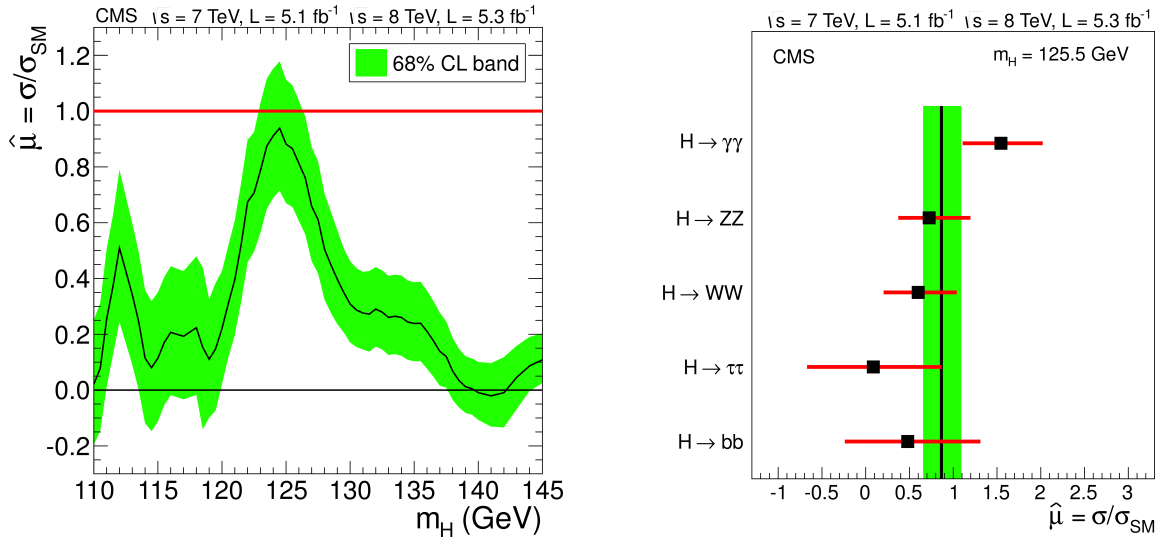

Figure 3.8: State-of-the-art (as of early 2015) Higgs discovery and decay plots from CMS, with all channels and early datasets combined. Figures from [43]

Second, CMS did many searches for new physics, interpreting the results in terms of the SMS models. No non-null results were obtained, but many low-mass SUSY scenarios were excluded. Figure 3.9 summarize the production mass exclued by each search. These negative results motivate the additional data presented here: the argument for SUSY as a solution to the naturalness problem, presented in section 2.4, requires a low-mass partner to the stop quark; if such a partner is not seen in the run-2 dataset at CMS, one of the key motivations for SUSY is greatly weakened.

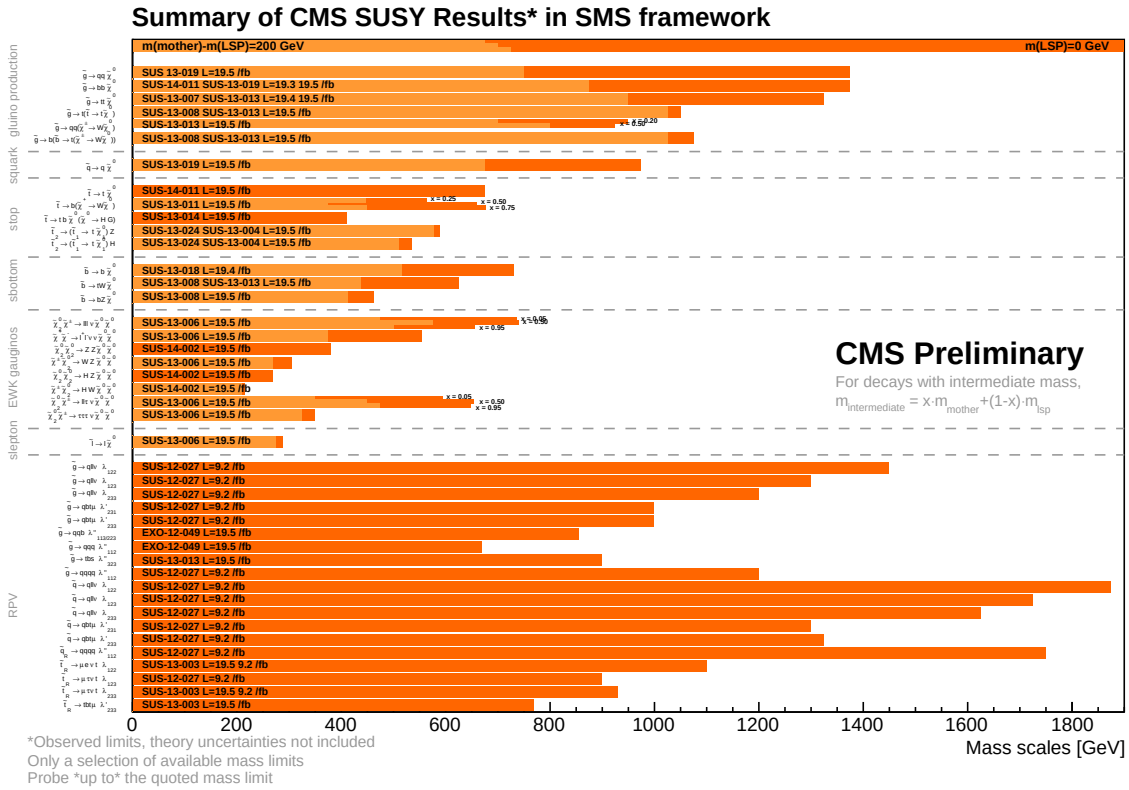

Figure 3.9: Summary of all CMS SUSY results as of late 2014. Figure taken from [42]

.

Finally, CMS has discovered the "tetraquark" and had several interesting discoveries related to a possible quark-gluon plasma. These results will not be discussed here, but references are provided for the curious, see [44] and [45].

Chapter 4

Overview of Searching for New Physics with SS Dileptons

From an experimental point of view, the search for new physics (a supersymmetric particle or any other new particle) is largely a problem of reducing the signal-to-background ratio. The processes we search for are expected to have very small cross-sections. For example, the di-gluino production cross-section for 1200 GeV gluinos, with squarks decoupled, is only 85.6 fb. In contrast, the SM hadronic production cross-section is 68.9 mb, nearly a billion times higher!

Searching for two leptons allows much more sensitivity as the SM cross-sections for processes that produce two leptons are much smaller. By far the largest such background is Z-decay, at about 24.7 nb. By requiring the two leptons to have the same electrical charge (sign), even these backgrounds are largely rejected. Of course, the trade-off is that we reject signal too: this analysis has no sensitivity to SUSY processes that do not produce a same-sign (SS) dilepton pair. Note that this signature does not require supersymmetry specifically: this inclusive search will be sensitive to any process that gives an abnormally

large number of SS dilepton events.

It should be clarified from the beginning that "same-sign dileptons" does not include neutrinos (which are not detectable and have no charge), nor τ leptons (which decay before they can be detected) unless the τ leptons decay immediately to electrons or muons.

In this chapter we will start by reviewing the naturalness-inspired SUSY processes that would appear at the LHC's energy scale and would be detectable with our requirement of two SS dileptons. We will then turn to the SM background processes that would also appear. Third, we will introduce the key variables that allow us to reject the background processes while not rejecting signal. Finally, we will briefly review the previous searches for supersymmetric particles in this channel.

4.1 SUSY signatures in SS Dilepton Events

As was discussed in section 2.4, certain SUSY-inspired "simplified models" have been developed to quantify the search for SUSY. Of those given in table 2.1, a SS dilepton analysis has sensitivity to only certain T1, T5, and T6 models; these models have $W^{\pm}$ bosons that can decay to leptons. Example Feynman diagrams for the models under consideration are given in figures 4.1, 4.2, and 4.3. Note that the model refers only to the decay mode of the SUSY pair; the initial SUSY pair production can happen through any mechanism (the production method specified in the diagram is just one example). Further, other models can be extrapolated from the pictured models in the obvious way; for example, T1tttt becomes T1bbbb if the four top quarks are replaced by bottom quarks.

The diagrams in this chapter show the "hard-scattering" for each process, but most of

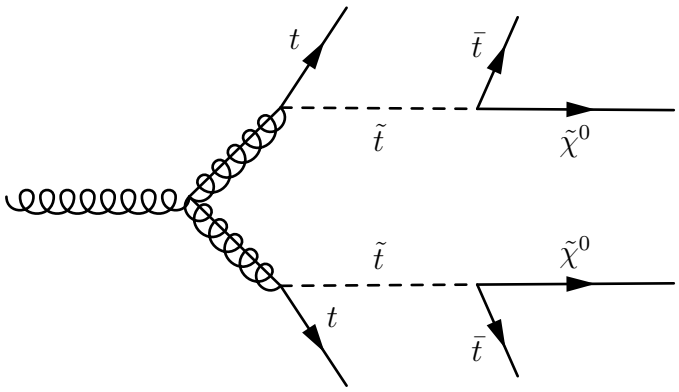

Figure 4.1: Example Feynman Diagrams for T1tttt and T5tttt. In T1tttt, the stop squarks are virtual and so it is a 3-body decay; in T5tttt, the stop squarks are on-shell and so it is a sequence of 2-body decays. Note that the $W^{\pm *}$ produced by the decay of the top quarks will immediately decays to fermions.

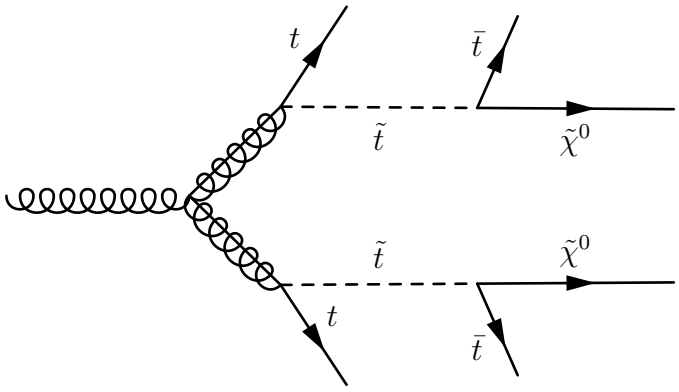

Figure 4.2: Example Feynman Diagrams for T9ttbbffff and T5ttbbffff. In T5ttbbffff, the charginos are virtual and so it is a 3-body decay; in T9ttbbffff, the charginos are on-shell and so it is a sequence of 2-body decays. Note that the $W^{\pm *}$ produced by the decay of the top quarks will immediately decays to fermions.

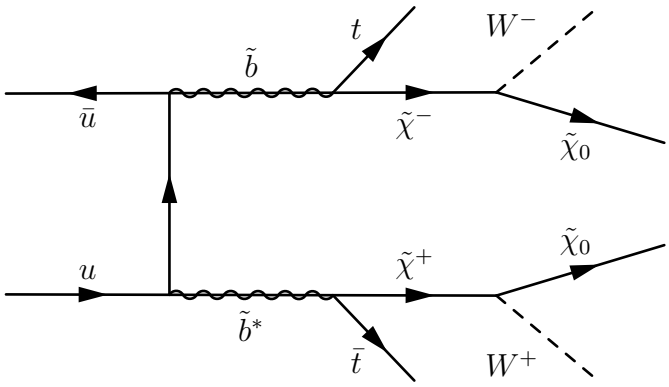

Figure 4.3: Example Feynman Diagrams for T6ttWW.

the "final state" particles pictured will decay before they can be detected. In particular, the top-quarks will decay almost immediately through the process $t \to bW^+$ (with 100% probability), and all Ws, Zs, Hs, and τs will decay according to their usual branching ratios. Quarks other than the top quark will hadronize and form showers (jets); of these, only the b-jet can be reliably distinguised from the others.

Also, note the processes in the Feynman Diagrams do not contain the so-called underlying event: after the collision, the remaining quarks and gluons that did not participate in the process pictured remain, and will have to immediately hadronize to preserve color neutrality.

To quantify the expected backgrounds, we will need both the cross-sections and the branching ratios. The methods for evaluating the cross-sections were discussed in chapter 1, but the actual calculations are typically done to next-to-leading order (NLO) or even to NNLO using software; we shall only quote the results here. For the branching ratios, we begin with the reference values given in table 4.1.

Decay	BR
$\tau \to$ e, μ	35.24%
W $\to$ e, μ	21.32%
W $\to \tau$	11.25%
Z $\to e^+e^-$, $\mu^+\mu^-$	6.73%
Z $\to \tau^+\tau^-$	3.70%
H $\to \tau\tau$	6.32%
H $\to Z\gamma$	0.154%
H $\to WW$	21.5%
H $\to ZZ$	2.64%
H $\to \ell^+\ell^-$	2.34% ($\ell = e, \mu$) 1.06% ($\ell = e, \mu, \tau$)

Table 4.1: Important branching ratios taken from [48] and [47]. The Higgs mass is taken as 125.0 GeV, and BRs below 0.1% are omitted.

From this we can determine the odds that the bosons decay to final states with 1 or 2 leptons. For example, the W boson may reach a final state with an electron or muon by direct decay or through a τ. Thus, the monoleptonic branching ratio is $21.32\% + (.3524) \cdot 11.25\% = 25.28\%$. A similar process must be taken for the Z and the H;[1] the results are given in table 4.1.

Boson	BR to 1 lepton	BR to 2+ leptons	Total BR to leptons
W	25.3%	0	25.3%
Z	1.7%	7.2%	8.9%
H	11.9%	4.0%	15.9%

Table 4.2: Bosonic branching ratios into leptonic final states, where $\ell = e, \mu$.

With these values we can calculate the dileptonic branching ratios for our signal processes. These branching ratios, along with the cross-sections, are given in table 4.3 for signal. Multiplying the cross-section, the branching ratio, and the integrated luminosity gives the number of events we would expect to see produced for any given background. Note that this is only the number produced; the number detected will be lower than this due

[1]For the Higgs calculation one must approximate from the last entry in the table that the odds of the $\ell^+\ell^-\nu_\ell\bar{\nu}_\ell$ final state having 0, 1, or 2 τs is 1.06%, 1.03%, and 0.03%, respectively.

Model	Mass	cross-section	branching ratio	eff. cross-section
T1tttt, T5tttt	800 GeV	1489.1 fb	19.51%	290.5 fb
	1000 GeV	325.4 fb		63.5 fb
	1200 GeV	85.6 fb		16.7 fb
	1500 GeV	14.2 fb		2.8 fb
T6ttWW	600 GeV	174.6 fb	19.51%	34.1 fb
	650 GeV	107.0 fb		20.9 fb

Table 4.3: Cross-Sections and dileptonic branching ratios for simplified models. Mass refers to the gluino mass for T1 and T5, and stop/sbottom mass for T6.

to trigger inefficiencies and analysis cuts. We will examine the acceptance in subseqent chapters.

4.2 Sources of Background

Rares

Though our analysis signature (SS dileptons) was specifically chosen because of the relatively small cross-section of the SM processes bearing this signature, there are nontheless several SM processes that must be accounted for. The most important rare processes are shown in figure 4.4: the combination of their cross-section, branching ratio to SS dileptons, and topology (resemblance to signal events) is such that these are the dominant rare backgrounds for the analysis. Less important rare processes are shown in figure 4.5.

Fakes

When we refer to a "dileptonic" signature, it is implied that the leptons come from the signal or background process; in other words, the collision produces a boson which immediately decays to leptons. However, leptons can also be produced in other ways: in particular, a b-quark undergoing decay might produce a lepton, or a heavy particle such

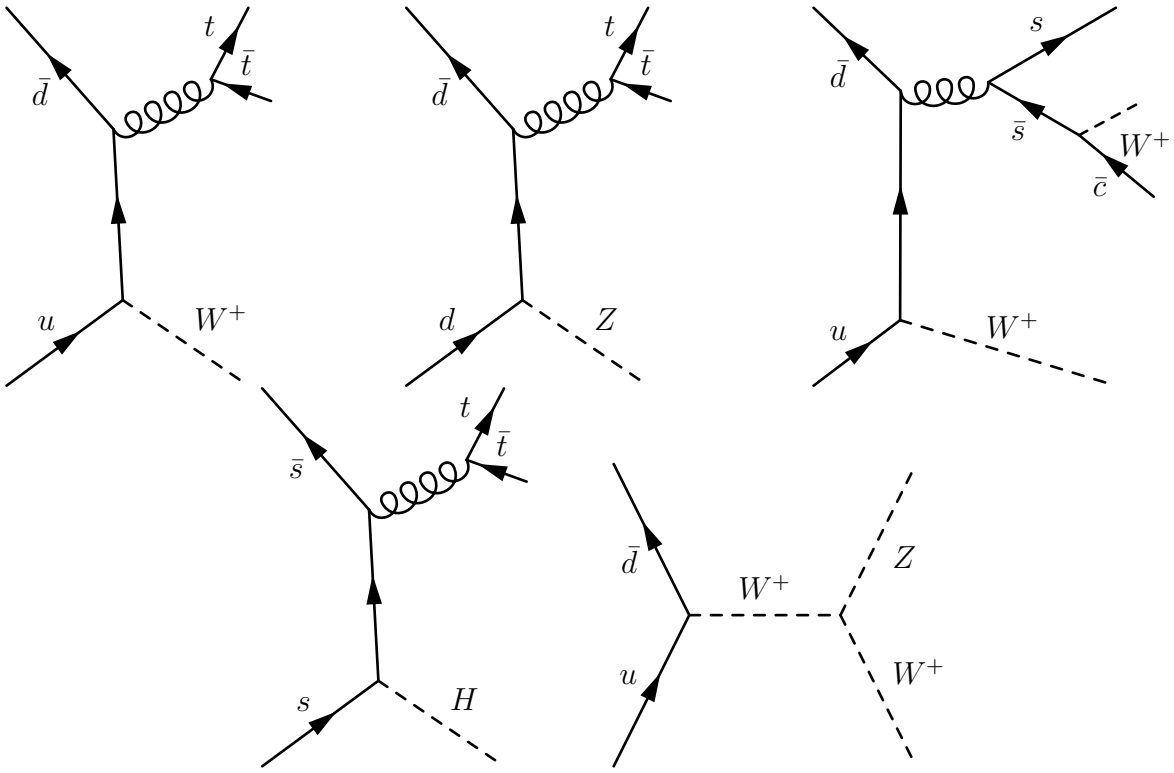

Figure 4.4: Example Feynman Diagrams for ttW, ttZ, qqW$^{\pm}$W$^{\pm}$, ttH, and WZ.

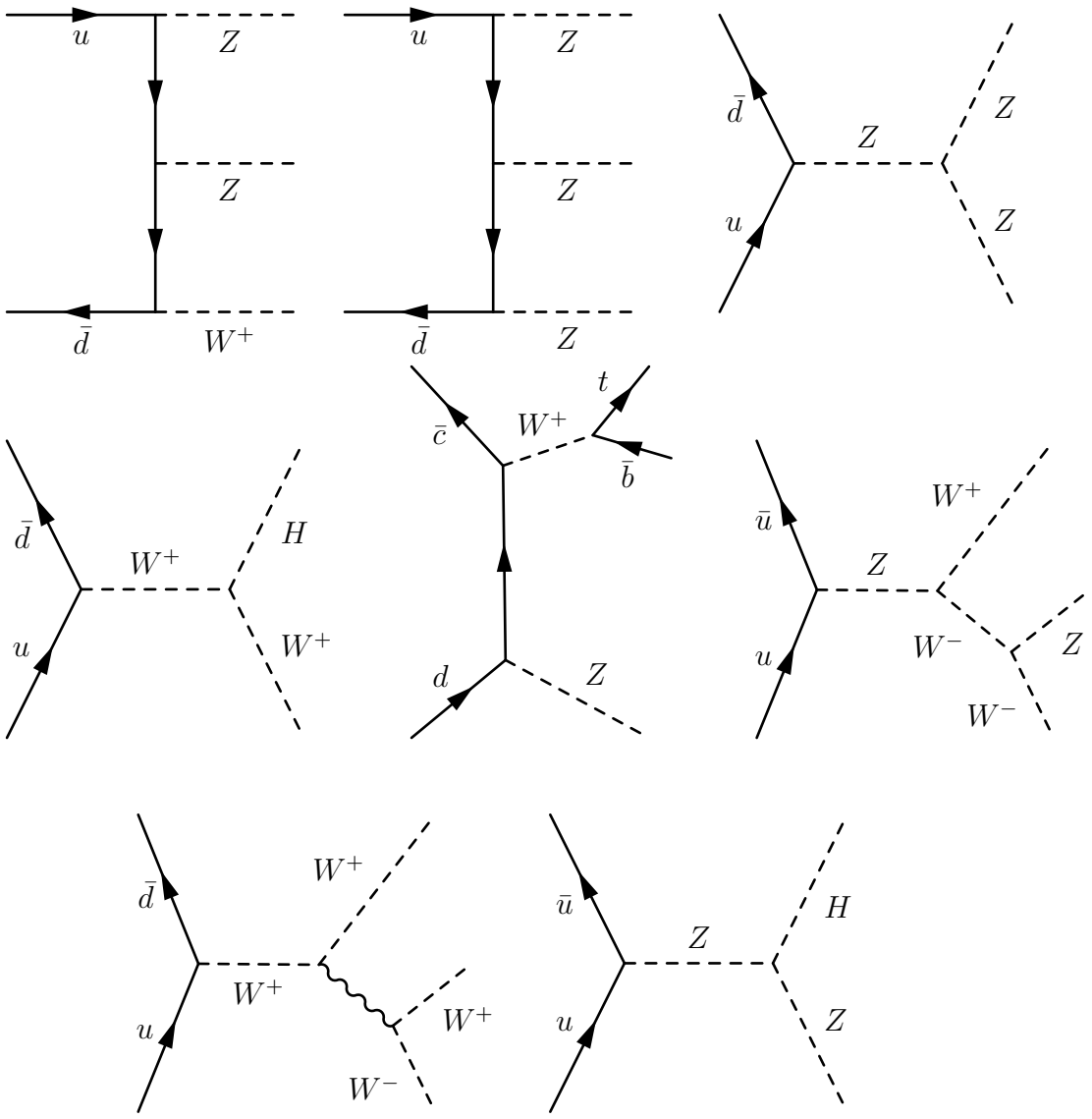

Figure 4.5: Example Feynman Diagrams for tbZ, WWZ, WWW, and ZH, WZZ, ZZZ, ZZ, and WH.

as a pion or kaon might decay to a muon, or a hadron might be misidentified. In all cases except the last, the lepton is a "real lepton" and so will pass all of our identification requirements, but it is considered "non-prompt" or "fake" since it was not produced as an immediate consequence of the collision. It is important to note that in this case, "fake" is a misnomer – it really is a lepton, just not a lepton that was produced as an immediate result of the collision.

Unlike the rares, which cannot be mitigated, most fake leptons can be rejected during the reconstruction. Non-prompt leptons are normally in the middle of a jet (not isolated), while non-leptons can behave quite differently than leptons in the detector. The reconstruction algorithm exploits these differences to reject fakes wherever possible. However, the relatively large cross-sections of some processes that can produce fakes (such as ttbar) cause fakes to remain a significant background that must be accounted for at the analysis level.

Figure 4.6 shows the diagrams for many processes that do not give real SS dileptons, but can give fakes or flips.

Flips

There is another mechanism by which real, prompt leptons can be improperly counted as SS events: when the charge is incorrectly reconstructed (a charge flip). For example, a high-energy electron will not bend very much in the magnetic field, increasing the chances that its charge will be incorrectly reconstructed. This is a serious problem for electrons, but not a problem for muons, as muons reconstructed with the opposite sign in the tracker will not be detected in the expected location in the muon chambers.

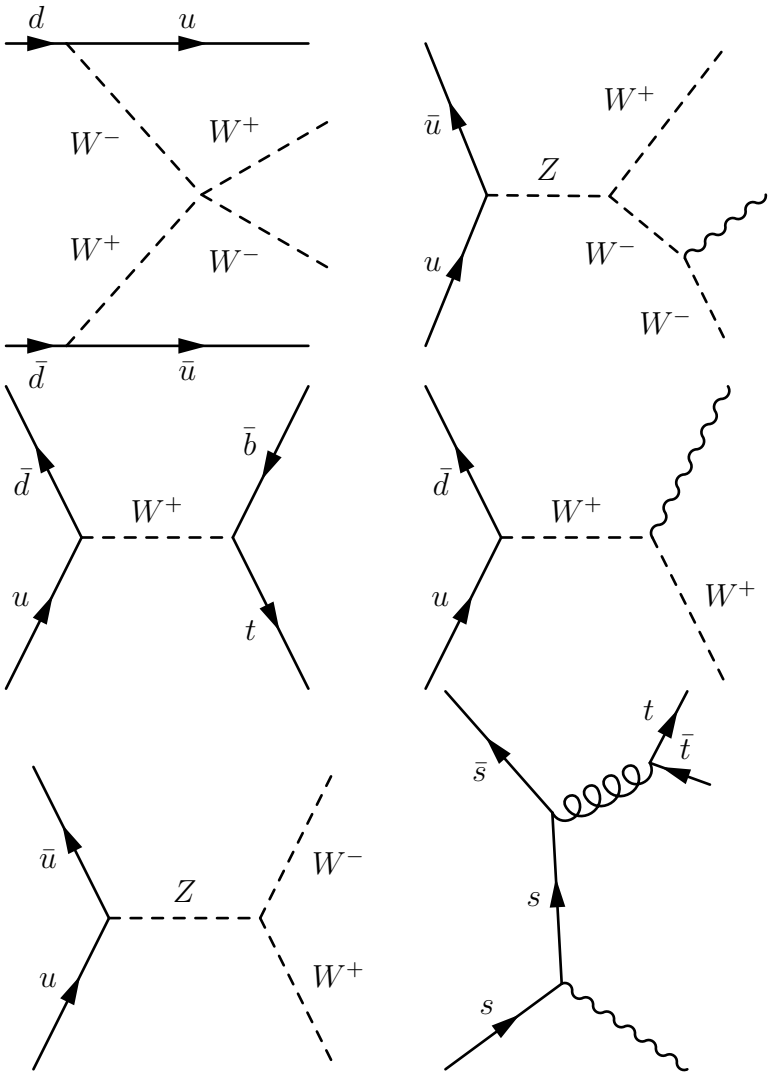

Figure 4.6: Example Feynman Diagrams for processes that give SS dileptons only through fakes or flips: DPS, WWγ, single top, Wγ, W^+W^-, ttγ.

Electrons can also undergo a charge flip due to a conversion: in the course of Bremsstrahlung, the electron will emit a very energetic photon, leaving the original electron without enough energy to be reconstructed. The photon will pair-produce, but may give most of the energy to the positron, so only the positron is reconstructed (of course, this could also happen with the signs reversed). The result is that the charge really does flip sign along the electron's trajectory. This background must be accounted for at analysis level.

Again, muons are much less susceptible to these physical charge flips. Figure 4.8 shows that even at only 1 GeV, the electron's energy loss as it passes through the detector will be dominated by Bremsstrahlung, a form of photon radiation. Conversely, figure 4.7 shows that at these energies, muons lose most of their energy through ionization, not radiation, and the magnitude of this energy loss is much smaller (this is why muons are often referred to as minimally-ionizing particles).

4.3 Key Variables

Several variables are used at the analysis level in order to mitigate these backgrounds. We give a brief overview of each kinematic variable here.

MET. Conservation of momentum requires that the sum of the transverse momentum vectors must be zero (the longitudinal components of the momentum vectors are ignored). If summing the vectors of all the reconstructed particles in the transverse plane gives a nonzero resultant, the negative of this resultant can be defined as the missing transverse energy, or MET (it is really momentum rather than energy, but it is called MET for historical reasons). "Real MET" comes from the particles that cannot be reconstructed,

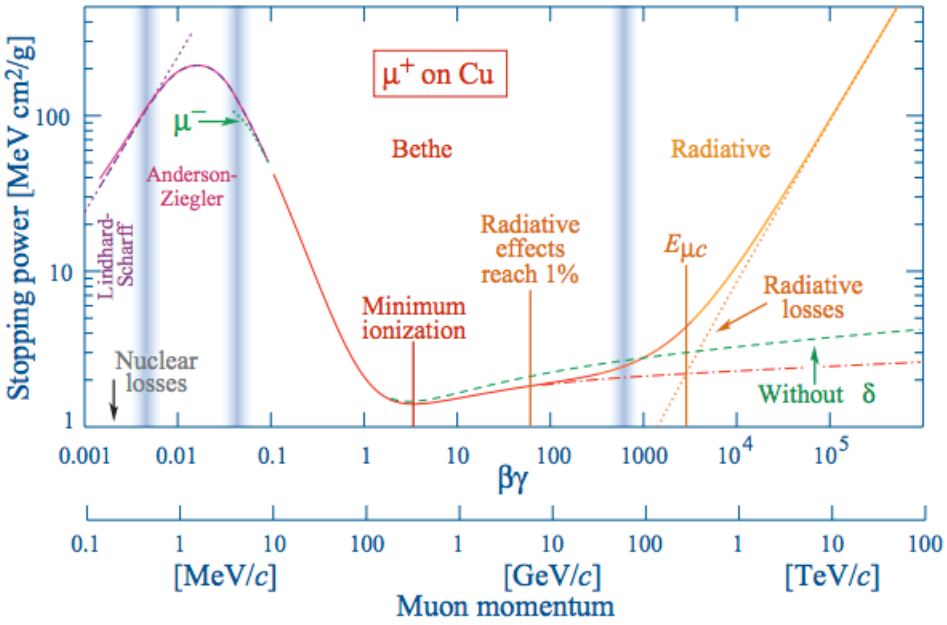

Figure 4.7: Sources of muonic energy loss as a function of muon energy (in copper). Figure from [49].

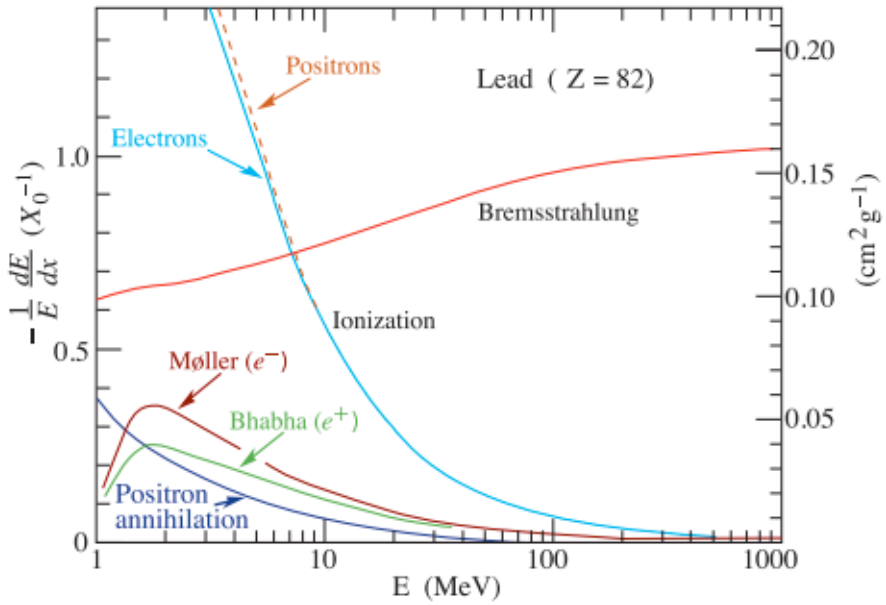

Figure 4.8: Sources of electronic energy loss as a function of electron energy (in lead). Figure from [49].

such as neutrinos and the $\tilde{\chi}^0$ in the SUSY models. However, it is also affected by detector effects, in particular jet mismeasurement, pileup and the underlying event.

H_T and **nJets**. Many signal models produce a considerable number of jets; T1tttt, for example, can produce up to 6 jets while producing SS dileptons. H_T, the scalar sum of the transverse momentum of all of these jets, as well as the number of jets, are useful variables to reject events inconsistent with these models.

nBtags. As discussed in section 2.4, third-generation sparticles are preferred; this leads us to expect that our signal will produce many b-quarks. A b-tagging algorithm uses the displacement between the b-quark production and decay and the energy of the decay products to "tag" jets as being likely from a bottom quark. The number of b-tags is then useful to reject events that have too few (or too many) b-quarks to be consistent with a particular model.

M_T^{min}. As discussed in the previous section, one of our dominant backgrounds is when a W decays leptonically (producing MET from the neutrino, and one lepton), and the second lepton is a fake. To reduce this background, we use the minimum invariant transverse mass: we add each transverse lepton vector to the MET vector and take the invariant mass (this will give something smaller than the W mass for the real lepton, and some random value for the fake), and then choose the minimum. By requiring $M_T^{\min} < M_W$, we can reject virtually all events with a leptonic W decay and a fake lepton. However, such an $M_T^{\min}$ cut cannot be indiscriminanatly applied: although it gives an excellent signal-to-background ratio, it also reduces our expected number of signal events significantly. This variable must therefore be applied only in carefully-constructed SRs.

Baseline Region

We use these key variables to define both the search regions (SRs) and a baseline region. For the baseline region, we require at least two jets: this is expected to significantly reduce the background from Z-decay events with a fake or flipped lepton. We further require MET > 30 || $H_T > 500$ GeV; this is a way to reduce our background significantly without rejecting events that could be consistent with an undetected, stable final-state particle (such as a SUSY LSP) or that show unusually high hadronic activity. The SRs are defined in section 5.7, and are a proper subset of the baseline region.

4.4 Previous Searches for New Physics with Dileptons

In 1993, Barnett *et al* published "Discovering Supersymmetry with like-sign dileptons," [52] which described the "remarkable sensitivity" that this signature could provide "at both the Fermilab Tevatron Collider and at the Superconducting Super Collider." Since then, this search has been conducted several times, starting at the Tevatron [53], which reported an insignificant excess (of 44 events, compared to the 33.2 ± 4.7 predicted), and more recently at the LHC at 7 TeV (ATLAS and CMS) and 8 TeV (CMS only). This dissertation is thus the fourth generation of this analysis. In the next chapters, we will describe the strategy and results of this search; however, it is first worth reviewing the results of the previous generation. We will confine ourselves here to discussing the 8 TeV search at CMS.

The 8 TeV analysis defined search regions as follows:

$N_{b\text{-jets}}$	MET (GeV)	N_{jets}	$200 < H_T < 400$ (GeV)	$H_T > 400$ (GeV)
$= 0$	50 - 120	2-3	SR01	SR02
		≥ 4	SR03	SR04
	≥ 120	2-3	SR05	SR06
		≥ 4	SR07	SR08
$= 1$	50 - 120	2-3	SR11	SR12
		≥ 4	SR13	SR14
	≥ 120	2-3	SR15	SR16
		≥ 4	SR17	SR18
≥ 2	50 - 120	2-3	SR21	SR22
		≥ 4	SR23	SR24
	≥ 120	2-3	SR25	SR26
		≥ 4	SR27	SR28

Table 4.4: Search regions for the 8 TeV analysis

The background predictions and yields for each of these search regions are given in table (4.5). There is clearly no statistically-significant excess, so we turn to the SUSY exclusions. Here we will list each SUSY model's approximate upper-limit for the excluded production mass. The stated exclusion is of course only (approximately) accurate for the case with a large mass-splitting (ie the LSP is much lighter than the produced SUSY particle); analyses have less sensitivity in the region with low mass-splitting (the "diagonal") because the decay products have less energy.

As a final metric of the 8 TeV analysis's sensitivity, it is worth considering this analysis's sensitivity relative to that of other analyses. Figure 4.9 shows the excluded mass points for the T1tttt process as a function of gluino and LSP mass. It is clear that the same-sign signature by itself (labeled in the figure as SUS-13-013) has only an average exclusion, but when combined with the orthogonal channels (labeled as SUS-14-010), the exclusion is dramatically improved.

Region	Low-p_T		High-p_T	
	Expected	Observed	Expected	Observed
SR01	44 ± 16	50	51 ± 18	48
SR02	12 ± 4	17	9.0 ± 3.5	11
SR03	12 ± 5	13	8.0 ± 3.1	5
SR04	9.1 ± 3.4	4	5.6 ± 2.1	2
SR05	21 ± 8	22	20 ± 7	12
SR06	13 ± 5	18	9 ± 4	11
SR07	3.5 ± 1.4	2	2.4 ± 1.0	1
SR08	5.8 ± 2.1	4	3.6 ± 1.5	3
SR11	32 ± 13	40	36 ± 14	29
SR12	6.0 ± 2.2	5	3.8 ± 1.4	5
SR13	17 ± 7	15	10 ± 4	6
SR14	10 ± 4	6	5.9 ± 2.2	2
SR15	13 ± 5	9	11 ± 4	11
SR16	5.5 ± 2.0	5	3.9 ± 1.5	2
SR17	4.2 ± 1.6	3	2.8 ± 1.1	3
SR18	6.8 ± 2.5	11	4.0 ± 1.5	7
SR21	7.6 ± 2.8	10	7.1 ± 2.5	12
SR22	1.5 ± 0.7	1	1.0 ± 0.5	1
SR23	7.1 ± 2.7	6	3.8 ± 1.4	3
SR24	4.4 ± 1.7	11	2.8 ± 1.2	7
SR25	2.8 ± 1.1	1	2.9 ± 1.1	4
SR26	1.3 ± 0.6	2	0.8 ± 0.5	1
SR27	1.8 ± 0.8	0	1.2 ± 0.6	0
SR28	3.4 ± 1.3	3	2.2 ± 1.0	2

Table 4.5: Event yields from the 8 TeV search

Process	Excluded Production Mass
T1tttt	1050 GeV
T2tt	1050 GeV
T1bbbb	525 GeV
T1ttbb	1050 GeV
T5qqqqWW	950 GeV

Table 4.6: Approximate excluded production mass in the 8 TeV analysis in the region with large mass splitting

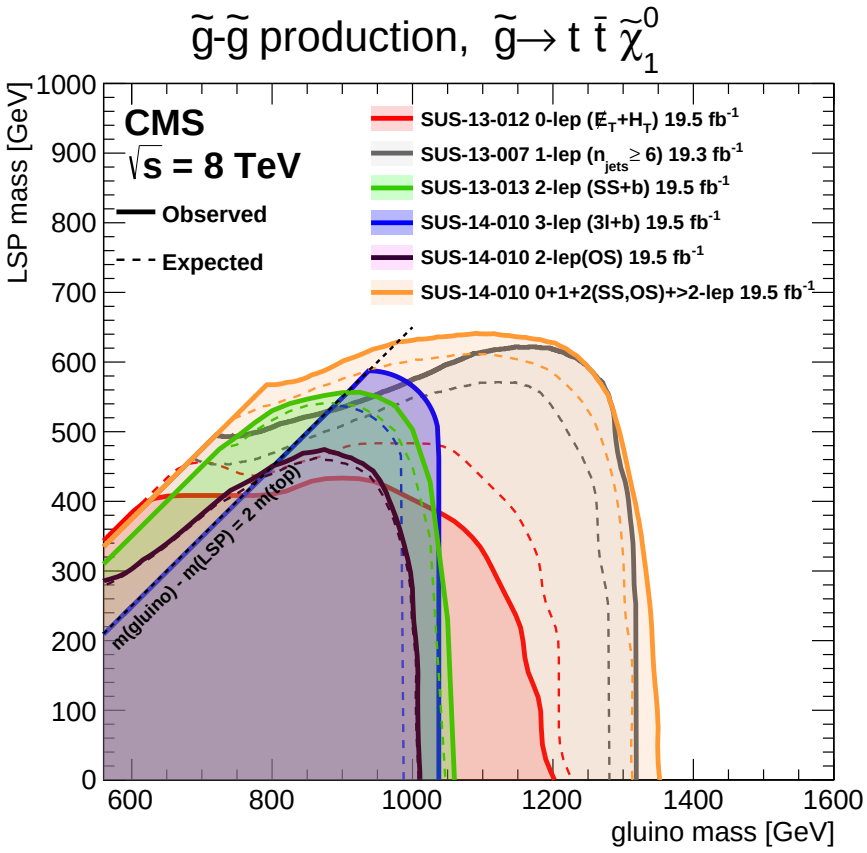

Figure 4.9: State-of-the-art exclusion limits (as of early 2015) on the T1tttt SMS model. Figure taken from [42].

Chapter 5

The 2015 Search: Strategy, Definitions and Commissioning

We have now completed our discussion of the motivation and general overview of this analysis, and so we are ready to turn to the details of the analysis at hand. This analysis is expected to be published in April 2016 and presented at the Moriond Conference.

We will begin by discussing the specific improvements with respect to the earlier versions of the analysis and then turn to the technical definitions of the objects and triggers. With these definitions, we can consider the commissioning plots in order to compare the agreement between data and simulation: this is a good cross-check that the Standard Model and simulation software are consistent with the experimental results under the object definitions chosen. Having validated our ability to make reasonable predictions from simulation, we conclude this chapter by defining the search regions to be used in this analysis.

5.1 Improvements to the Run-1 Method

In addition to the obvious (higher energy, eventually higher luminosity), the improvements to the run-1 method include the following:

- Use of the M_T min variable. As mentioned in 4.3, the M_T min variable offers considerable discrimination between signal and background. This variable was never deployed in run-1, but is used in the signal region definitions of run-2.

- Improved rare calculations. A new generation software "Madgraph5-aMC@NLO" was used during this analysis. This software allows processes to be generated at next-to-leading order precision, allowing more accurate cross-sections and modeling of the kinematical properties.

- Improved rare systematics. "Rare" SM processes make up significant backgrounds in this search, both in run-1 and run-2. The predicted backgrounds from these processes are taken from simulation. In run-1 the uncertainty on these processes was difficult to ascertain, so a conservative 50% on the total was assumed. In run-2, more conservative uncertainties were able to be calculated based on the renormalization, factorization, and PDF uncertainties.

- Improved fake rate calculations. The essential method of the fake rate calculation is unchanged, but a few improvements have been implemented. Further, a parallel *in situ* fake-rate measurement provides additional information.

- Improved isolation definition. This version of the analysis introduces several new isolation variables that offer considerably more sensitivity than the "relIso" used previously.

5.2 Trigger Definitions

All data events are required to fire one of our analysis triggers and all simulated events are required to fire one of our simulated triggers.[1] We then take a scale factor to account for the non-perfect data-simulation agreement.

Definitions

We use two sets of triggers: one for events with (offline) $H_T > 300$ GeV and another for events with (offline) $H_T < 300$ GeV. Both sets require a lepton pair meeting an asymmetric p_T requirement. To save bandwidth, three additional online cuts are imposed to reject events that would not be likely to pass online cuts. First, for triggers with (offline) $H_T > 300$ GeV requirement, the same requirement is also imposed online.[2] Second, events with $H_T < 300$ are required to pass an online-isolation cut for muons (electrons) of $I_{rel} < 0.4$ (0.2), where I_{rel} is defined by:

$$I_{\text{rel}} = \begin{cases} \frac{\sum_R p_T(\text{Tracker}) + \sum_R E_T(\text{calorimeter})}{p_T(\ell)} & \text{(electrons)} \\ \frac{\sum_R p_T(\text{Tracker})}{p_T(\ell)} & \text{(muons)} \end{cases} \tag{5.1}$$

Third, cuts on the the longitudinal impact parameter dZ and/or a requirement that the invariant mass be greater than 8 GeV (to reject low-mass resonances) were added to some triggers as listed in table 5.2. This table also lists the p_T thresholds for the two leptons.

[1] Except, for technical reasons, the signal samples, which get a scale factor and a larger systematic only.

[2] Note that in this case, the H_T is defined as for offline, except that jets are not cleaned for leptons: a lepton with $p_T > 40$ GeV will automatically be considered a jet. This leg of the trigger requirement is therefore not completely independent of the event's leptonic activity. Note that this effect is in the "good" direction; triggered events can fall out of the selection offline, but no events that failed the trigger due to this effect would have been selected offline.

H_T	Channel	Trigger Name
< 300 GeV	$\mu\mu$	HLT_Mu17_TrkIsoVVL_Mu8_TrkIsoVVL_DZ HLT_Mu17_TrkIsoVVL_TkMu8_TrkIsoVVL_DZ
	ee	HLT_Ele17_Ele12_CaloIdL_TrackIdL_isoVL_DZ
	eμ	HLT_Mu17_TrkIsoVVL_Ele12_CaloIdL_TrackIdL_IsoVL HLT_Mu8_TrkIsoVVL_Ele17_CaloIdL_TrackIdL_IsoVL
> 300 GeV	$\mu\mu$	HLT_DoubleMu8_Mass8_PFHT300
	ee	HLT_DoubleEle8_CaloIdM_TrackIdM_Mass8_PFHT300
	eμ	HLT_Mu8_Ele8_CaloIdM_TrackIdM_Mass8_PFHT300

Table 5.1: List of Trigger Names

Turn-On Curves

We quantify the efficiency of these triggers using the tag-and-probe method. As an example, we will here consider the low-H_T dielectron trigger (the result is shown in figure 5.1).[3] We first look in the single electron dataset for events that have two electrons. We require that:

- One lepton, the "probe" is the one that fired the unprescaled trigger allowing the event to enter the dataset (in our example, the Ele12_CaloIdL_IsoVL trigger). We further require that this lepton passes the full analysis selection and is matched to the trigger object (within $\Delta R < 0.4$).

- A second lepton, the "tag" must be found that also passes the full analysis selection, not including the p_T cut.

- For triggers with an online H_T cut, the event must have an offline H_T greater than the online H_T threshold and the two leptons must have an invariant mass greater than 10 GeV.

- For triggers with an online dZ cut, the offline dZ must be greater than the online

[3]For the other trigger turn-on curves, see [58].

dZ threshold. The efficiency of dZ trigger leg is measured separately from that of the leptonic legs.

Events passing the above cuts are entered into the denomintor of the efficiency. Our requirement that both leptons pass the full analysis ID reduces the fake rate to the sub-percent level, so it is not necessary to subtract off the fake contribution.

The numerator is then defined as events in which the probe fires one leg of the dilepton trigger being studied. Figure 5.1 shows the turn-on curve for the low-H_T dielectron trigger. The parameters p0, p1, and p2 at the top of the figure show the fit parameters to the error function given by:

$$\varepsilon(p_T) = p0 \text{ erf}\left(\frac{p_T - p1}{p2}\right) \tag{5.2}$$

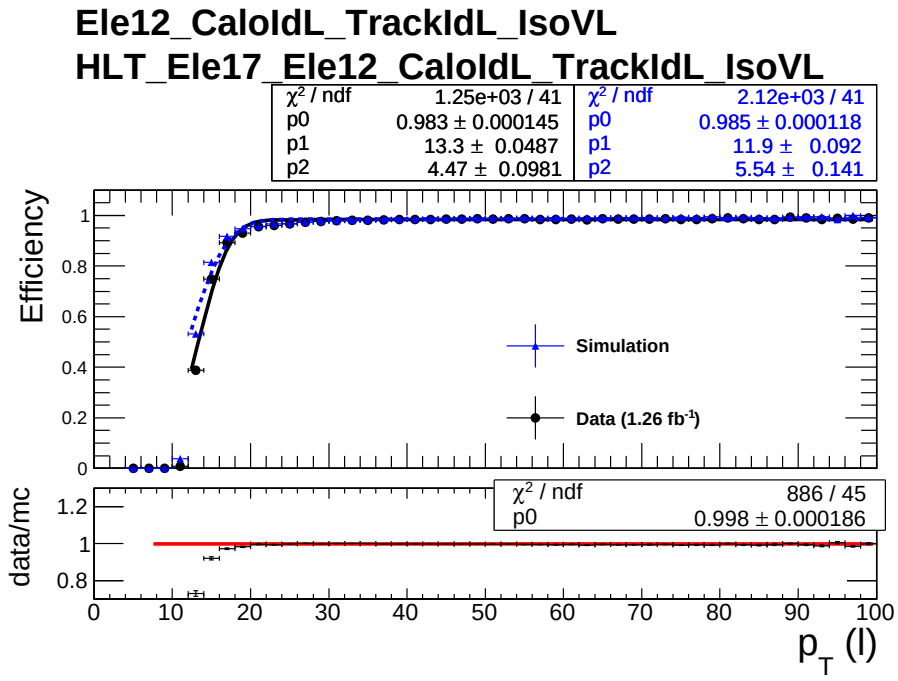

Figure 5.1: Trigger efficiency for the less energetic electron in dilepton pairs electron HLT_Ele17_Ele12_CaloIdL_TrackIdL_IsoVL.

5.3 Lepton Definitions

In addition to the online requirements (triggers), several offline requirements are also used to identify the leptons.

Electron MVA

The CMS Physics Object Group (POG) devoted to electrons and photons (EGamma) has trained a multivariate analyzer to identify electrons. The inputs to the MVA are the following.

Shower shape variables:

1. $\sigma_{i\eta i\eta}$: The width (in η) of 5x5 supercluster (in ECAL), corrected for gaps between crystals. Electrons have a characteristic shower shape that is narrow in η but wide in ϕ (due to Bremssstrahlung).

2. $\sigma_{i\phi i\phi}$: same as above, in ϕ

3. The supercluster η width (in the ECAL), uncorrected

4. The supercluster ϕ width (in the ECAL), uncorrected

5. Circularity: 1 minus the ratio of highest energy 1x5 block containing seed (in ECAL) vs. the total energy in 5x5 block (on seed). This is useful for jet rejection, since the jets tend to deposit energy in more crystals.

6. R9: the ratio of energy in 3x3 block containing seed vs. the total energy in 5x5 block containing seed, same reason as above

Tracking Variables:

7. N_{hits} in the tracker

8. χ^2 to quantify the agreement between the reconstructed tracks and the expected tracks for an electron with the given momentum (lower is better), normalized by number of degrees of freedom (hits). This is for CKF tracks (tracks using the Combinatorial Kalman Filter method of track reconstruction).

9. χ^2 as above, but using an alternative method of track reconstruction (GSF)

10. $\Delta\eta$ between the supercluster (in the ECAL) and at the beginning of the track (in the tracker)

11. $\Delta\phi$ between the supercluster (in the ECAL) and at the beginning of the track (in the tracker)

12. $\Delta\eta$ between the supercluster (in the ECAL) and at the end of the track (in the tracker)

Energy variables:

13. HE: Energy in the HCAL / energy in the ECAL. The ECAL is approximately 25 radiation lengths long, so this this should be quite low for electrons.

14. EP: Electron energy in ECAL divided by momentum at the beginning of the track. In principle $E/P = 1$ for electrons, but the products of Brehmssstrahlung will be invisible to the tracker, so P may be low, causing E/P to be slightly above unity.

15. EP out: As above, but using momentum at the end of the track

16. 1/E - 1/P, another permutation of E/P. This one is useful because momentum is not necessarily well-measured at high momentum, so E/P can be far from unity, while 1/E - 1/P will approach zero.

17. Energy in the Preshower / Energy in the Supercluster. This is useful to reject very forward neutral pions (in the endcap) that decay to two photons, which can give a shower shape similar to an electron: such events will have a very large energy deposit in the preshower.

18. Brem Fraction: the fraction of the electron's energy spent through Bremssstrahlung. Electrons are expected to lose significant energy by Bremssstrahlung, particularly at low energy.

Isolation

The charged leptons produced in decays of heavy particles are generally spatially isolated from the hadronic activity in the event, while the leptons produced in the decays of hadrons or misidentified leptons are usually embedded in jets. It is therefore advantageous to require isolation as an identification requirement for leptons. Here we consider four definitons of isolation.

- Relative Isolation (RelIso): the p_T of all objects wihin a cone of size ΔR around the lepton, divided by the p_T of the lepton itself. The cone size is typically taken to be $\Delta R = 0.4$.

- Mini-Isolation (MiniIso): same as relIso, but the cone size is defined as $0.05 \leq \Delta R = 10/p_T(\ell) \leq 0.2$. Further, an effective area correction is applied to offset the effect of pileup: the event's rho (average pileup energy per unit area in the transverse plane) is multiplied by the effective area of the lepton (taken as a function of $|\eta|$) and this quantity is subtracted from the sum of the objects inside the cone.[4]

[4]The effective areas were calculated by the appropriate POG, the values are available at [59].

- The p_T-Ratio (PtRatio): the p_T of the lepton divided by the p_T of the closest jet. Jets with $|\eta| > 3.0$ are not eligible for selection as the closest jet.

- The p_T-Rel (PtRel): same as PtRatio, but after lepton jet subtraction. Thus:

$$p_T^{rel} = \frac{[\vec{p}_T(jet) - \vec{p}_T(\text{lep})] \cdot \vec{p}_T(\text{lep})}{|\vec{p}_T(jet) - \vec{p}_T(\text{lep})|} \tag{5.3}$$

These three definitions are combined into one isolation cut (dubbed multi-isolation, or MultiIso), according to the formula:

$$\text{MultiIso} = \text{MiniIso} < A \;\&\&\; (\text{PtRatio} > B \;||\; \text{RelIso} > C) \tag{5.4}$$

Note that the definition of MultiIso is dominated by the miniIso requirement – it uses the same underlying concept as RelIso, but it also profits from the boostedness of objects with higher momentum. Such objects are therefore contained in a smaller cone size, reducing the chance that the isolation is artificially high because of other objects in the unused part of the cone. The drawback of this is the reduced ability to identify leptons that are inside jets. The second term in equation (5.4) addresses this: leptons inside jets will have a small PtRatio and PtRel, and will therefore fail the MultiIso definition.

Impact Parameter

Both leptons should be consistent with originating from the same collision vertex. Hence, we have requirements on the transverse impact parameter (dxy), the longitudinal impact parameter (dz), and the significance of three-dimensional impact parameter (SIP3D), where the three-dimensional impact parameter is defined as $\sqrt{dxy^2 + dz^2}$.

Conversion Veto

To protect against photon conversions, we reject electron candidates with more than one missing hit in the inner layers of the pixels. Further, a conversion veto filter, which looks for partner tracks (e^+, e^- coming from a common point, for example), is applied to all working points.

Three Charge Agreement

The charge of each electron is determined using three different track-fitting techniques; all three techniques must agree or the electron is rejected. This strongly reduces the rate of electrons reconstructed with the incorrect charge.

Offline Trigger Cuts

A number of trigger-safe cuts are applied to remove the ambiguity where an electron can pass the offline selection but fail the online selection in simulation. These are hard cuts on quantites taken in the MVA.[5] Further, all leptons must fire the appropriate (simulated) trigger in (simulated) data, as described in section 5.2.

Muon Reconstruction Filter

Muons are required to be either global muons (reconstructed in both muon system and tracker) or tracker muons (reconstructed in tracker only). In either case, events with a momentum uncertainty larger than 20% are rejected, as this indicates a lack of confidence in the reconstructed trajectory.

[5]See AN table 13 for a complete list.

Summary, Lepton Working Points

This analysis uses three different working points for the lepton definitions in different places. To avoid confusion with the working points (WPs) suggested by the POG, we will name our WPs veto, loose, and tight.

	electrons			muons		
	Veto	Loose	Tight	Veto	Loose	Tight
min MVA, $\|\eta\| < 0.8$	-0.70	0.87	0.87	-	-	-
min MVA, $0.8 < \|\eta\| < 1.479$	-0.83	0.60	0.60	-	-	-
min MVA, $\|\eta\| > 1.479$	-0.92	0.17	0.17	-	-	-
A	0.4	0.4	0.16	0.4	0.4	0.12
B	0	0	0.80	0	0	0.76
C	0	0	7.2	0	0	7.2
dxy (mm)	0.5	0.5	0.5	0.5	0.5	0.5
dz (mm)	1.0	1.0	1.0	1.0	1.0	1.0
min sip3d	-	4	4	-	4	4
min p_T (GeV)	7	7	15	5	5	10
max $\|\eta\|$	2.5	2.5	2.5	2.4	2.4	2.4
max nMissingHits	1	0	0	-	-	-
conv veto	yes	yes	yes	-	-	-
3-charge agreement	no	yes	yes	no	no	no
reco filter	no	no	no	no	yes	yes

Table 5.2: Summary of Lepton WP Definitions. A, B, and C are defined in equation (5.4).

The "tight" working points of table 5.2 are required for the leptons of events that enter the analysis control regions: these are therefore referred to as "tight," "good," or "selected" events interchangeably throughout this dissertation. The loose requirements are used in the fake rate method (see section 6.2), while the veto leptons are used in the dilepton pair selections described below.

Dilepton Pair Selections

Leptons selected according to the online and offline cuts described above are then grouped into pair candidates. Pair candidates must pass the following selections:

- The leptons in the pair must have the same electrical charge (hence the name of the analysis).
- Neither lepton in the candidate pair may form a secondary pair with any other veto lepton of the same flavor and opposite sign if this secondary pair would have an invariant mass less than 8 or between 76 and 106. This is designed to supress leptons resulting from the decay of a Z or γ^*.

In the case that more than one candidate pair meets these requirements in a given event, the preference is given first to $\mu\mu$ and secondly to μe events, due to the better detector performance for muons (as discussed in section 3.3). Any remaining ambiguity is resolved by choosing the pair with the largest magnitude of the scalar sum of the lepton momenta.

5.4 Jet and MET Definitions

Jets are quark or gluons that undergo hadronization and showering inside the detector. They are reconstructed by clustering the reconstructed particles ("particle flow candidates") into jets.[6]

Jet Energy Corrections

The four-momentum vectors for the jets are corrected according to the procedure described in [57].

[6]This is done using the anti-kt algorithm with a cone size of $\Delta R < 0.4$, see [54].

Jet ID

Only jets with $p_T > 40$ GeV and within $|\eta| < 2.4$ are considered. Further, the fraction of the jet's energy content provided by electrically-neutral (muonic) particles is required to be less that 99% (80%).

Jet Cleaning

To avoid double counting, jets within $\Delta R < 0.1$ of any loose lepton (as defined in table 5.2) are rejected.

B-tagging

Jets passing the above selection (with the p_T threshold reducted to 25 GeV) can be categorized as b-jets if the b-tagging discriminator returns a value higher than the threshold (0.890, per the recommendation from the appropriate POG). The b-tagging descriminator is described in [55]: it is a multi-variate analyzer that searches for the characteristic spatial difference between the proposed quark's production vertex and its decay vertex.

MET

The missing transverse energy is defined as the negative sum of the transverse momentum of all the particle flow candidates reconstructed in an event. The type-1 jet energy corrections are propogated to the MET following the procedure defined in [56].

5.5 Scale Factors

Trigger Scale Factors

Trigger scale factors are extracted from the turn-on curves presented in section 5.2. The trigger requirement is applied to both data events and simulated events. Then the scale factor corrects only for the difference between the trigger efficiency in data and simulation. This scale factor is extracted from the turn-on curves as the ratio of the plateau values (p_0, in equation (5.2)); for the example considered in section 5.2, the SF is 0.998.

The scale factors for the various trigger legs are given in table 5.3; each trigger will pick up a factor for each of the two lepton legs, and possibly an additional SF for any dZ or H_T legs as well. It has been verified that the "factorization hypothesis" – that product of the leg efficiencies gives the total trigger efficiency – holds to within 0.5% per leg.

Trigger	Leading Leg	Lagging Leg	dZ
Mu17_TrkIsoVVL_Mu8_TrkIsoVVL_DZ Mu17_TrkIsoVVL_TkMu8_TrkIsoVVL_DZ	0.982	0.99	0.973
Ele17_Ele12_CaloIdL_TrackIdL_isoVL_DZ	0.997	0.998	0.998
Mu17_TrkIsoVVL_Ele12_CaloIdL_TrackIdL_IsoVL	0.998	1.00	-
Mu8_TrkIsoVVL_Ele17_CaloIdL_TrackIdL_IsoVL	0.98	1.00	-
DoubleMu8_Mass8_PFHT300	0.985		-
DoubleEle8_CaloIdM_TrackIdM_Mass8_PFHT300	0.979		-
Mu8_Ele8_CaloIdM_TrackIdM_Mass8_PFHT300	0.981 (μ), 0.996 (e)		-

Table 5.3: Trigger efficiency per leg as measured by the tag-and-probe method. The H_T leg efficiency (where applicable) is 1.00, so this is omitted from the table. The leading HLT_ has been removed from the trigger names.

Trigger Scale Factors in Signal

The simulated signal events are produced in Fastsim, which does not contain the trigger information; therefore, signal samples are run without any trigger requirement, and the trigger efficiency is factored in as a scale factor. The efficiency is measured in fullsim ttbar samples and parameterized in H_T, p_T and $|\eta|$; the topology of ttbar is sufficiently similar to the signal that this is thought to be an accurate approximation of the signal trigger efficiency after parameterizing.

To calculate the efficiency, we take into the denominator all events that pass our baseline selection and contain two tight leptons. The numerator of course consists of denominator events that successfully fire the trigger. The trigger maps are shown in [60]; the only feature of note is that a significant loss of efficiency is noted for events with $H_T > 1$ TeV: most notably in the dielectron channel, where the efficiency decreases from 0.935 ($800 \leq H_T \leq 1200$ GeV to 0.680 ($H_T > 2500$) GeV.

Lepton Scale Factors

The lepton efficiencies are measured with a tag-and-probe method similar to the one described previously for the triggers. In this case, $Z \to \ell^+\ell^-$ decay events are used in both data and simulation. We define the tag as one lepton passing the analysis ID, and the probe as a second lepton passing a looser ID but with a 4-momentum such that the invariant mass of the tag and the probe are consistent with a Z decay (a subtraction is made for non-Z events that happen to be consistent with the Z-mass). Then the data/simulation efficiencies are compared in various bins of p_T and $|\eta|$; the results are

given in tables 5.4 and 5.5.[7]

		$\|\eta\| \in [0, 0.8]$	$\|\eta\| \in [0.8, 1.44]$	$\|\eta\| \in [1.44, 1.56]$	$\|\eta\| \in [1.56, 2]$	$\|\eta\| \in [2, 2.5]$
$H_T > 300$	$10 \leq p_T < 20$	0.800833	1.09259	1.38004	1.06353	1.01303
	$20 \leq p_T < 30$	0.951939	0.978131	1.00001	0.944541	0.958243
	$30 \leq p_T < 40$	0.974265	0.979292	0.978247	0.973954	0.982194
	$40 \leq p_T < 50$	0.979367	0.984915	0.989583	1.00021	0.995648
	$p_T > 50$	0.980086	0.980024	0.986589	0.984587	0.995184
$H_T < 300$	$10 \leq p_T < 20$	0.81309	1.09402	1.38969	1.05715	1.01151
	$20 \leq p_T < 30$	0.952485	0.978021	0.999009	0.947156	0.957892
	$30 \leq p_T < 40$	0.974451	0.978913	0.979384	0.973866	0.981911
	$40 \leq p_T < 50$	0.979478	0.984782	0.990569	1.00085	0.996501
	$p_T > 50$	0.980182	0.979994	0.988436	0.984572	0.995253

Table 5.4: Electron SFs. Units for p_T and H_T are GeV.

	$\|\eta\| \in [0, 0.9]$	$\|\eta\| \in [0.9, 1.2]$	$\|\eta\| \in [1.2, 2.1]$	$\|\eta\| \in [2.1, 2.4]$
$10 \leq p_T < 20$	0.950673	0.959971	0.96344	0.97954
$20 \leq p_T < 25$	0.968778	0.985696	0.986646	0.961432
$25 \leq p_T < 30$	0.986112	0.982328	0.981606	0.964637
$30 \leq p_T < 40$	0.989584	0.990363	0.989629	0.954459
$40 \leq p_T < 50$	0.990997	0.990606	0.991023	0.951617
$50 \leq p_T < 60$	0.987545	0.989335	0.99151	0.94982
$p_T \geq 60$	0.992751	0.9878	0.988131	0.958638

Table 5.5: Muon SFs. Units for p_T are GeV

Pile-Up Reweighting

We further apply a scale factor to align the number of pileup vertices in the simulation to that observed in data.

B-tag Scale Factor

The b-tagging efficiency is calculated in data and simulation using three different techniques, which are then statistically combined to give the overall efficiency in both simulation and data. This procedure and the results, are described in section 5 of [61]. We then

[7]The SFs for the signals are actually measured separately since they were produced with a different reconstruction algorithm ("Fastsim"); the scale factors used for signals are omitted here.

take the ratio of the data efficiency to the simulation efficiency to obtain the b-tagging SF.

5.6 Data vs. Simulation Commissioning Plots

In section 3.3 we studied the lepton and jet efficiencies using the definitions just discussed as well as looser (POG-recommended) definitions. Those studies were performed in simulation only; it now remains to use our dataset to study the data and simulation agreement in a control region. This will be a good cross-check that the data (including all the experimental software and hardware) matches the Standard Model prediction (including our simulation software). Note that these simulation plots will use "straight simulation"; we will not use any of the data-driven techniques discussed in the following chapter.

Figure 5.2 shows the invariant mass of the lepton pair. There are a few notable features of this plot:

- The peak at 91 GeV – we have rediscovered the Z boson!
- The data-simulation non-agreement (underprediction) at low values; our simulation considered does not have values at very low invariant dilepton mass. The same feature can be observed at low MET values in figure 5.3.
- The W+Jets sample used has poor statistics, resulting in spikes in some bins and a zero prediction in others.
- In general (not at low values), the simulation seems to model the shape correctly but slightly overpredicts.

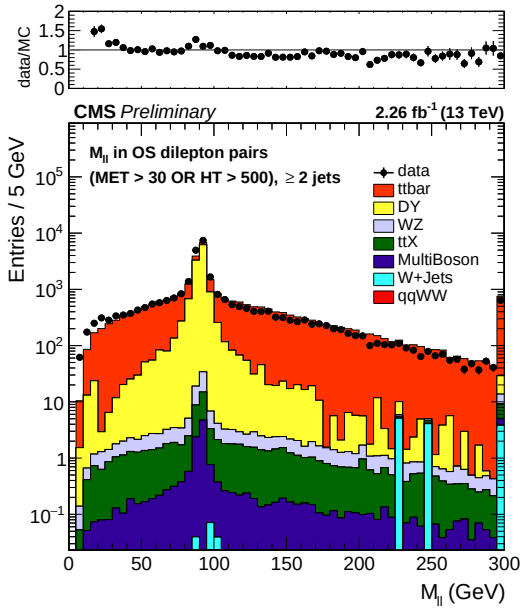

Figure 5.2: Invariant dilepton mass data vs. simulation commissioning plot in OS control region. The event selections are the same as for the analysis ("tight"), except (a) no Z-veto, (b) OS selection instead of SS, and (c) lepton $p_T > 25$ only. The last bin shows the overflow.

These observations (or a subset of them) are also clear in figures 5.3 and 5.4. These figures show that the simulation is successful in calculating the shape of the kinematic variables, but the normalization is not perfect. We quantify this by calculating the total predicted yield in this region, shown in table 5.6. To avoid the problem noted before at low invariant mass, table 5.6 requires that $M_{\ell\ell} > 30$ GeV.

category	total	ee	em	mm	total
ttbar	ttbar	2992.52	7949.04	4982.11	15923.80
	ST	136.63	318.96	192.34	647.93
DY	DY	4804.82	52.89	7732.79	12590.52
WZ	WZ	21.66	20.77	35.67	78.09
ttX	ttH	3.22	8.43	5.57	17.22
	ttZ	9.95	9.81	18.78	38.54
	ttW	2.10	5.39	3.54	11.03
W+Jets	W+Jets	8.17	4.95	0.00	13.12
MultiBoson	WWZ	1.83	1.89	2.96	6.67
	WZZ	0.94	0.31	1.32	2.57
	ZZ	2.33	1.48	3.38	7.19
qqWW	qqWW	0.00	0.01	0.00	0.01
total simulation		7984.15	8373.92	12978.46	29336.68
data		8026	6998	14856	29880

Table 5.6: Yields for data and simulation in the commissioning control region with an additional requirement that $M_{\ell\ell} > 30$ GeV.

We conclude that with all corrections applied, the data/simulation discrepency in this control region is approximately 2% (it turns out to be 3% if the region at low invariant mass is not removed). The systematic on the luminosity alone (see section 6.4) is 2.7%, so the simulation and data clearly agree within the uncertainty.

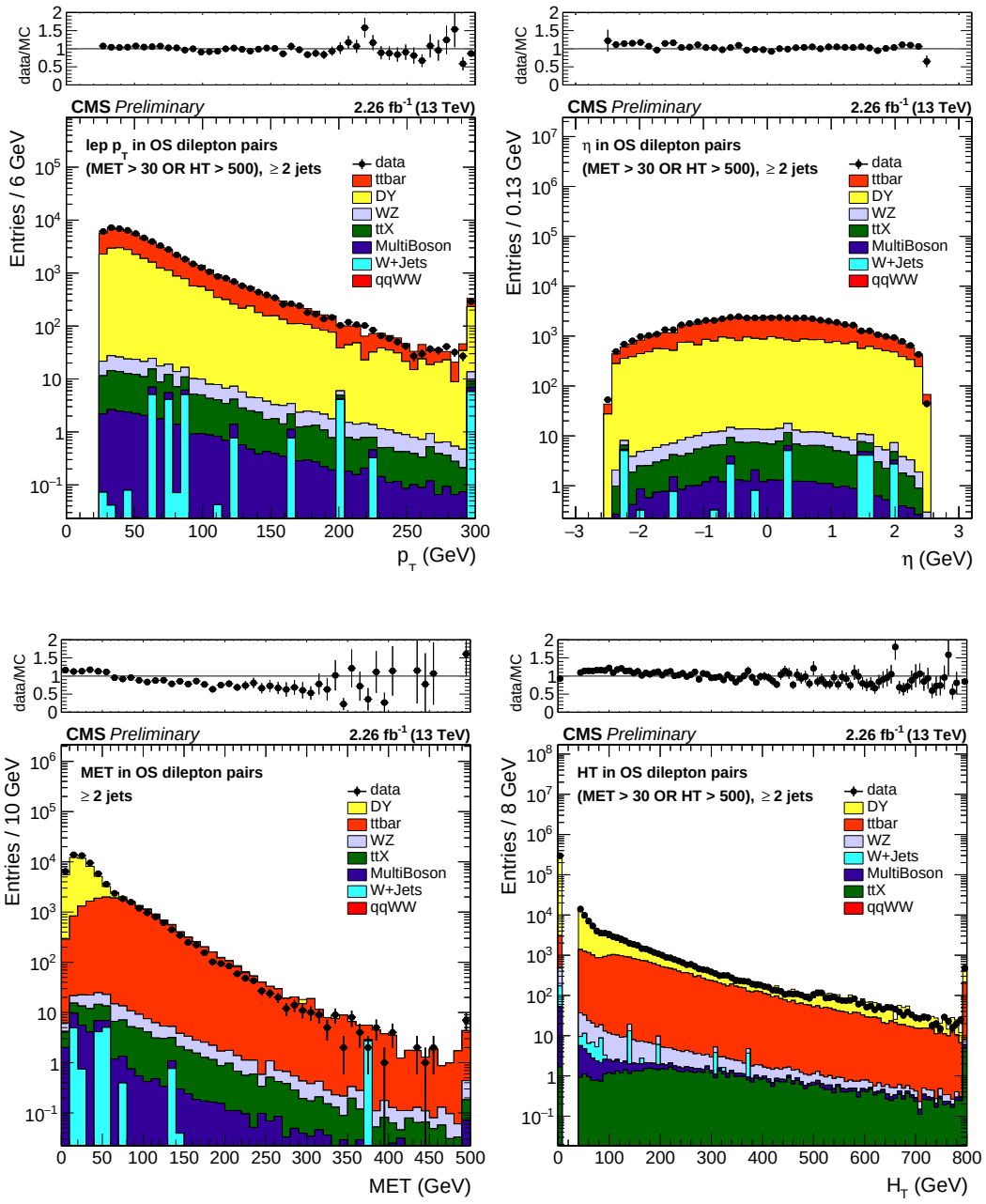

Figure 5.3: Data vs. simulation commissioning plots in OS control region. The event selections are the same as for the analysis ("tight"), except (a) no Z-veto, (b) OS selection instead of SS, and (c) lepton $p_T > 25$ only. The last bin of all plots shows the overflow. From left to right, the plots show: lepton p_T, pseudorapidity, MET, and H_T.

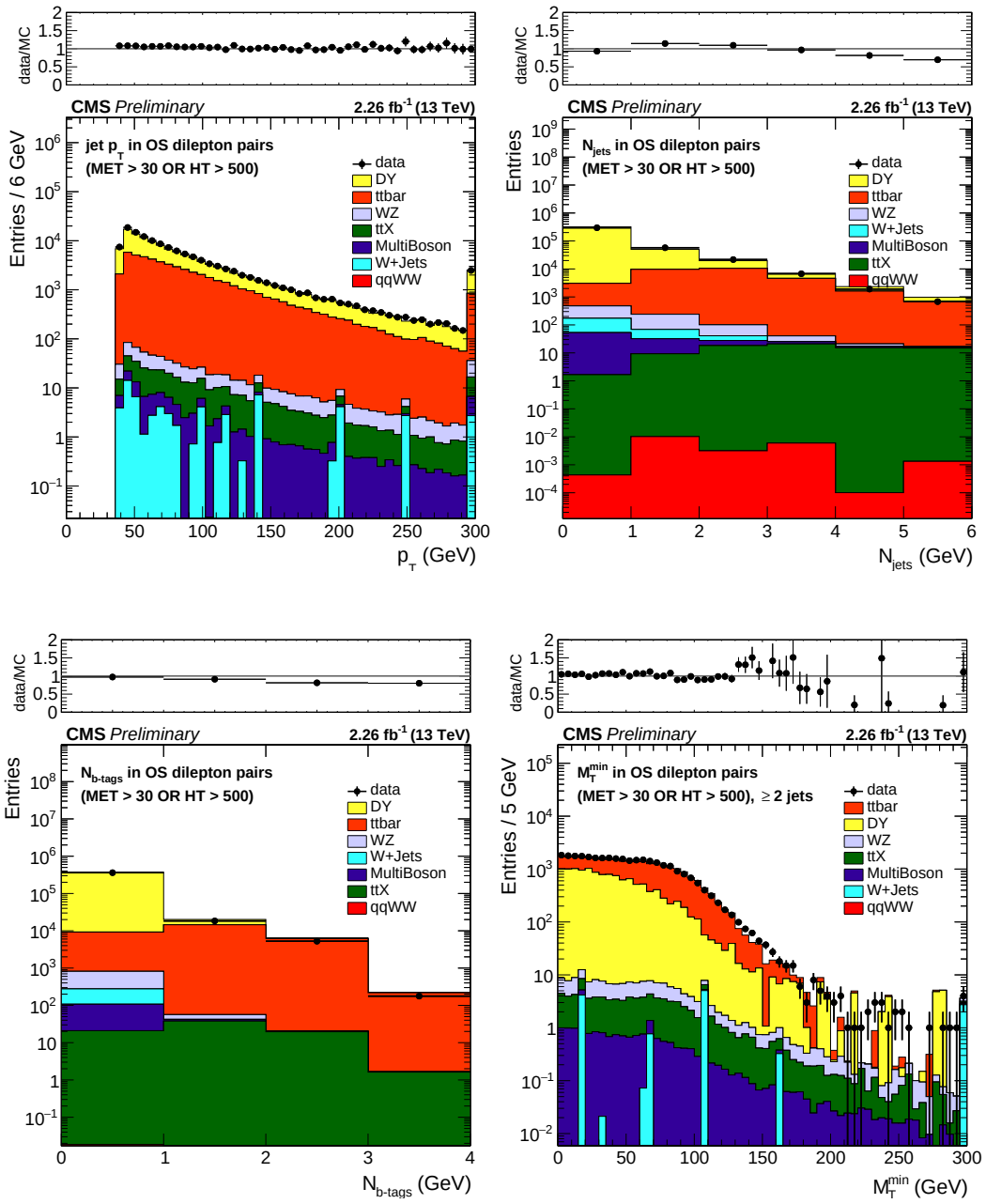

Figure 5.4: Data vs. simulation commissioning plots in OS control region. The event selections are the same as for the analysis ("tight"), except (a) no Z-veto, (b) OS selection instead of SS, and (c) lepton $p_T > 25$ only. The last bin of all plots shows the overflow. From left to right, the plots show jet p_T, nJets, nBtags, and $M_T^{\min}$.

5.7 Signal Region Definitions

To design the signal regions for this analysis, we use the following principles:

- Classes of signal regions are defined by the p_T of the dilepton pair. The classes are defined as:
  - High-High (HH): both leptons have $p_T > 25$ GeV. This targets models producing energetic leptons, and profits from the relatively low number of non-prompt leptons in this region.
  - High-Low (HL): one lepton has $p_T > 25$ GeV, the other has $10 \leq p_T \leq 25$ GeV. This provides sensitivity to models producing lower-energy leptons; however, the non-prompt leptons are a more significant background.
  - Low-Low (LL): both leptons have $10 < p_T < 25$ GeV. This provides further sensitivity to models producing lower-energy leptons; further, the background in this region is quite low.
- In each class of SRs, we draw a sharp distinction between the regions with $H_T \leq 300$ GeV and those with $H_T > 300$ GeV, because these two regions use different triggers.
- We define four "ultra" regions, two for HH and two for HL. Each ultra region has an ultra-high requirement on either $\mathrm{H_T}$ or MET, defined to have approximately one background event in 2.5 fb^{-1} of data.[8]
- Different regions are considered for different numbers of b-jets.

After dividing the regions according to the above principles, we divide additional regions based on MET, nJets, and M_T^{min} by considering the kinematic distributions of these vari-

[8] This is just an approximation as the simulation samples have changed more recently than the signal region definitions.

ables, shown in figure 5.5. Note that figure 5.5 also shows two T1tttt signal points just beyond the exclusion of the 8 TeV analysis (one with large mass splitting and one with small mass splitting); however, it is important not to overly optimize with respect to these signal points as we would like to have sensitivity to any possible signal.

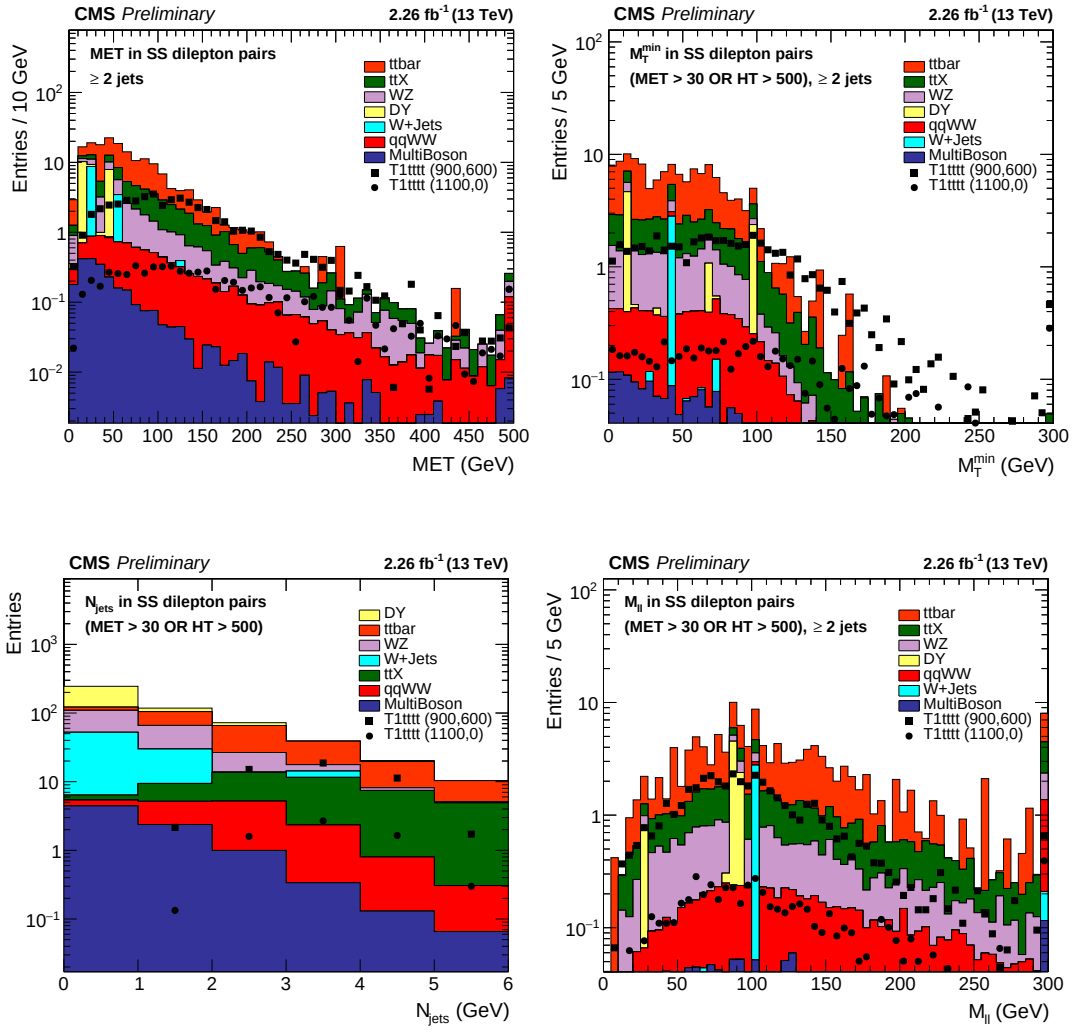

Figure 5.5: Simulated background and signal prediction plots in SS baseline region. The event selections are the same as for the HH analysis ("tight"). The last bin of all plots shows the overflow. From left to right, the plots show MET, $M_T^{\min}$, nJets, $M_{\ell\ell}$.

Having now divided the SRs according to all the relevant variables, we now combine underpopulated regions (considering also additional signal models not shown here). The resulting SRs are shown in figures 5.7, 5.8, and 5.9. Note that these SRs are mutually orthogonal and fully span the space[9], providing some sensitivity to all possible models of new physics.

[9]Technically, the space is fully spanned except for the "ultra" MET region with $H_T < 300$ GeV, and MET > 300; such events are rejected for simplicity. The alternative would be to either (a) merge with SR 31HH, which would involve mixing events with different trigger requirements, or (b) define an additional "ultra" SR with a bizarre topology.

<table>
<tr><td></td><td></td><td colspan="2"></td><td>$H_T < 300$</td><td>$300 < H_T < 1125$</td><td>$H_T > 1125$</td></tr>
<tr><td rowspan="16">0 b-tags</td><td rowspan="8">$M_T^{\min} < 120$</td><td rowspan="2">$50 < \text{MET} < 200$</td><td>2-4 jets</td><td>SR1HH</td><td>SR2HH</td><td rowspan="32">SR32HH</td></tr>
<tr><td>5+ jets</td><td rowspan="8">SR3HH</td><td>SR4HH</td></tr>
<tr><td rowspan="2">$200 < \text{MET} < 300$</td><td>2-4 jets</td><td>SR5HH</td></tr>
<tr><td>5+ jets</td><td>SR6HH</td></tr>
<tr><td rowspan="8">$M_T^{\min} > 120$</td><td rowspan="2">$50 < \text{MET} < 200$</td><td>2-4 jets</td><td>SR7HH</td></tr>
<tr><td>5+ jets</td><td rowspan="4">SR8HH</td></tr>
<tr><td rowspan="2">$200 < \text{MET} < 300$</td><td>2-4 jets</td></tr>
<tr><td>5+ jets</td></tr>
<tr><td rowspan="16">1 b-tags</td><td rowspan="8">$M_T^{\min} < 120$</td><td rowspan="2">$50 < \text{MET} < 200$</td><td>2-4 jets</td><td>SR9HH</td><td>SR10HH</td></tr>
<tr><td>5+ jets</td><td rowspan="8">SR11HH</td><td>SR12HH</td></tr>
<tr><td rowspan="2">$200 < \text{MET} < 300$</td><td>2-4 jets</td><td>SR13HH</td></tr>
<tr><td>5+ jets</td><td>SR14HH</td></tr>
<tr><td rowspan="8">$M_T^{\min} > 120$</td><td rowspan="2">$50 < \text{MET} < 200$</td><td>2-4 jets</td><td>SR15HH</td></tr>
<tr><td>5+ jets</td><td rowspan="4">SR16HH</td></tr>
<tr><td rowspan="2">$200 < \text{MET} < 300$</td><td>2-4 jets</td></tr>
<tr><td>5+ jets</td></tr>
<tr><td rowspan="16">2 b-tags</td><td rowspan="8">$M_T^{\min} < 120$</td><td rowspan="2">$50 < \text{MET} < 200$</td><td>2-4 jets</td><td>SR17HH</td><td>SR18HH</td></tr>
<tr><td>5+ jets</td><td rowspan="8">SR19HH</td><td>SR20HH</td></tr>
<tr><td rowspan="2">$200 < \text{MET} < 300$</td><td>2-4 jets</td><td>SR21HH</td></tr>
<tr><td>5+ jets</td><td>SR22HH</td></tr>
<tr><td rowspan="8">$M_T^{\min} > 120$</td><td rowspan="2">$50 < \text{MET} < 200$</td><td>2-4 jets</td><td>SR23HH</td></tr>
<tr><td>5+ jets</td><td rowspan="4">SR24HH</td></tr>
<tr><td rowspan="2">$200 < \text{MET} < 300$</td><td>2-4 jets</td></tr>
<tr><td>5+ jets</td></tr>
<tr><td rowspan="4">3+ b-tags</td><td rowspan="2">$M_T^{\min} < 120$</td><td>$50 < \text{MET} < 200$</td><td>2+ jets</td><td>SR25HH</td><td>SR26HH</td></tr>
<tr><td>$200 < \text{MET} < 300$</td><td>2+ jets</td><td>SR27HH</td><td>SR28HH</td></tr>
<tr><td rowspan="2">$M_T^{\min} > 120$</td><td>$50 < \text{MET} < 200$</td><td>2+ jets</td><td rowspan="2">SR29HH</td><td rowspan="2">SR30HH</td></tr>
<tr><td>$200 < \text{MET} < 300$</td><td>2+ jets</td></tr>
<tr><td>inclusive</td><td>inclusive</td><td>MET > 300</td><td>2+ jets</td><td></td><td colspan="2">SR31HH</td></tr>
</table>

Table 5.7: HH SRs

				$H_T < 300$	$300 < H_T < 1125$	$H_T > 1125$
0 b-tags	$M_T^{\min} < 120$	$50 < \text{MET} < 200$	2-4 jets	SR1HL	SR2HL	SR26HL
			5+ jets	SR3HL	SR4HL	
		$200 < \text{MET} < 300$	2-4 jets		SR5HL	
			5+ jets		SR6HL	
1 b-tags	$M_T^{\min} < 120$	$50 < \text{MET} < 200$	2-4 jets	SR7HL	SR8HL	
			5+ jets	SR9HL	SR10HL	
		$200 < \text{MET} < 300$	2-4 jets		SR11HL	
			5+ jets		SR12HL	
2 b-tags	$M_T^{\min} < 120$	$50 < \text{MET} < 200$	2-4 jets	SR13HL	SR14HL	
			5+ jets	SR15HL	SR16HL	
		$200 < \text{MET} < 300$	2-4 jets		SR17HL	
			5+ jets		SR18HL	
3+ b-tags	$M_T^{\min} < 120$	$50 < \text{MET} < 200$	2+ jets	SR19HL	SR20HL	
		$200 < \text{MET} < 300$	2+ jets	SR21HL	SR22HL	
inclusive	$M_T^{\min} > 120$	$50 < \text{MET} < 300$	2+ jets	SR23HL	SR24HL	
inclusive	inclusive	$\text{MET} > 300$	2+ jets		SR25HL	

Table 5.8: HL SRs

		$50 < \text{MET} < 200$	$\text{MET} > 200$
0 b-tags	$M_T^{\min} < 120$	SR1LL	SR2LL
1 b-tag	$M_T^{\min} < 120$	SR3LL	SR4LL
2 b-tags	$M_T^{\min} < 120$	SR5LL	SR6LL
3+ b-tags	$M_T^{\min} < 120$	SR7LL	
inclusive	$M_T^{\min} > 120$	SR8LL	

Table 5.9: LL SRs ($H_T > 300$ GeV and nJets ≥ 2)

Chapter 6

Background Estimation and Systematics

With our objects and signal regions defined, we are ready to estimate the background in each search region. To decrease our systematic uncertainty (and, hopefully, increase our accuracy), we use data-driven method to estimate most of the key backgrounds, using the "out-of-the-box" simulation results for only the less common rare processes. We will also consider other sources of uncertainty before closing the chapter.

6.1 Rares

In most SRs, our most significant rare background were from the ttW, ttZ, qqWW, and WZ backgrounds. We have developed some data-driven techniques to get a better handle on these four key backgrounds.

WZ

We define a WZ-enriched region according to the following cuts:

- One lepton with $p_T > 25$ GeV and $p_T > 20$ GeV passing the tight isolation cuts.
- A third lepton with $p_T > 10$ GeV forming an opposite-sign, same-flavor pair with $|M_{\ell\ell} - M_Z| < 15$ GeV. This third lepton is required to pass the tight ID requirement so as to avoid double-counting fake events (as described below).
- $H_T > 80$ GeV
- $2 \leq N_{\text{jets}} \leq 4$
- $N_{\text{b-jets}} = 0$
- MET > 30 GeV

The WZ purity in this region is 70%; for example, figure 6.1 shows the MET distribution in this region. We then calculate the WZ scale factor (WZSF) according to equation (6.1).

$$\text{WZSF} = \frac{\text{WZ data}}{\text{WZ Sim}} = \frac{\text{data - non-WZ Sim}}{\text{WZ Sim}} \tag{6.1}$$

Further, we identify the following systematics on the scale factor:

- Data: There are only 35 data events which results in a statistical error of about 17%
- Non-WZ Simulation: with a 70% purity, 30 of every 100 events are not from WZ. We assume a 50% error on these, for a total uncertainty of 15 events for every 70 events of WZ, or about 21% error. In addition, we take the usual statistical uncertainty.
- WZ Simulation: we take the usual statistical uncertainty, multiplied by the SF itself.

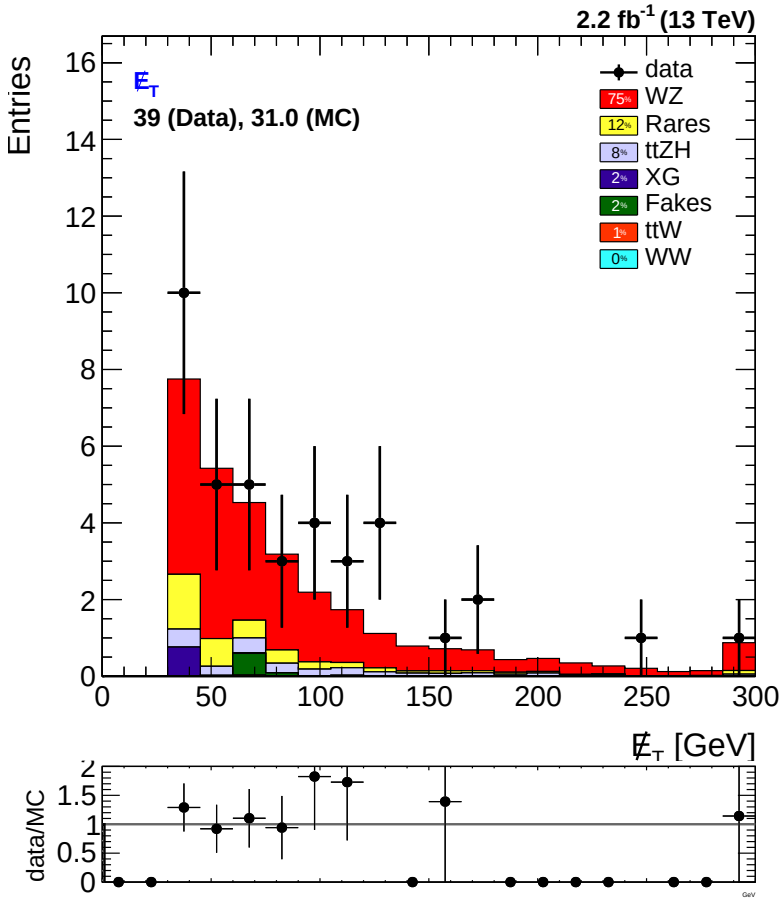

Figure 6.1: MET distribution as an example of the data/simulation agreement in the WZ-enriched control region.

Equation (6.1) therefore provides the following scale factor:

$$\text{WZSF} = 1.22 \pm 0.35 \tag{6.2}$$

This is a 28.6% uncertainty from the normalization and statistics, which we will round to 30%. The other uncertainties on this background (for example, signal migration caused by the jet energy scale) will be treated along with those from the other backgrounds in section 6.4; however, since the WZ is normalized in data, these systematics will affect only the shape and not the normalization of the signal region distribution plot.

ttW, ttZ, ttH, qqWW

For the ttW, ttZ, ttH, and qqWW samples, we attempted to quantify the simulation error. The sources of error in simulation can be broken down into four components.

The most significant effect comes from the renormalization and factorization scales, μ_R and μ_F. We have stated previously that the simulation software calculates cross-sections perturbatively, by evaluating the Feynman Rules for diagrams with increasing numbers of vertices. The three processes considered here are evaluated at NLO level: the first two terms in the expansion are considered. Now when evaluating the diagrams, two arbitrary scales must be chosen: the renormalization scale, which can be approximately described as the energy scale at which the interaction occurs, and the factorization scale, which can be approximately described as the energy scale below which the "soft" ISR and FSR processes are non-negligible, leading to the breakdown of the perturbation. A non-perturbative calculation's result would be independent of these scales, but since we consider only the first two terms, our result will have some dependence on both scales. In the processes considered here, both scales are set to $H_T/2$.

Secondary effects come from the uncertainty on the PDF collection and the strong coupling constant α_S. The PDF collection has many (100, in our case) associated parameters that can be varied, so the details of the PDF uncertainty can be rather opaque. We use the NNPDF 3.0 PDF collection which provides accuracy at up to the two-loop level, and we choose the coupling constant as $\alpha(m_Z) = 0.118$.

To estimate the uncertainties on the scales, the prediction in each search region is re-calculated after doubling and halving the factorization and renormalization scales. For

the PDF uncertainty, we follow the prescription of calculating the observable in each search region with all 100 PDF weights and assign an uncertainty equal to the standard deviation of the results. Similarly, we calculate the α_S uncertainty by recalculating the observable in each search region with α_S varied up or down by a factor of its uncertainty.[1]

The results for the ttW$^{\pm}$ sample are shown in table 6.1. We notice that the fiducial cross-section has a total systematic error of approximately 13%, so we apply this systematic error to all ttW search regions. We additionally merge all the high-H_T and low-H_T regions to quantify the error on the acceptance while minimizing the statistical fluctuation. We conclude to take a 3% (8%) systematic on the acceptance for the low-H_T (high-H_T) categories.

[1]The prescriptions are discussed more in [62] and the details of the PDF collection are discussed in [63].

SR	yield	stat (%)	scale (%)	pdf (%)	α_s (%)	syst (%)
fid c-s	329.28	0.99	12.97/13.65	1.29	2.17/1.84	13.88
HH SR1	2.18	11.7	13.5/12.8	1.55	2.08/2.10	13.8
HH SR2	2.62	10.7	21.8/18.5	14.38	3.95/3.47	26.4
HH SR3	0.42	27.0	21.8/17.4	3.65	2.14/1.75	22.2
HH SR4	0.45	33.3	-0.6/9.2	3.18	1.76/1.96	9.9
HH SR5	0.45	30.7	5.2/11.0	3.85	1.89/0.47	11.8
HH SR6	0.09	47.1	32.1/23.7	6.79	0.49/2.39	32.9
HH SR7	0.31	31.6	18.5/17.7	1.53	2.14/1.87	18.7
HH SR8	0.14	43.0	24.5/19.1	5.16	3.77/1.15	25.3
HH SR9	5.54	7.4	7.2/9.8	1.51	2.07/1.81	10.1
HH SR10	8.65	6.0	16.0/15.5	1.68	2.15/1.58	16.2
HH SR11	0.65	24.0	-0.60/7.0	3.10	1.17/1.59	7.8
HH SR12	2.65	11.7	19.4/18.0	1.33	2.57/2.33	19.6
HH SR13	1.95	11.3	10.0/13.7	1.49	2.44/1.84	13.9
HH SR14	0.25	47.6	-2.7/8.9	1.72	1.47/1.50	9.2
HH SR15	0.67	23.1	19.1/17.9	1.93	2.08/1.48	19.3
HH SR16	0.34	41.2	7.1/12.7	2.14	1.95/1.97	13.0
HH SR17	3.51	9.2	9.9/10.5	1.76	1.98/1.70	10.9
HH SR18	6.35	7.2	8.8/12.3	1.35	2.12/1.76	12.5
HH SR19	0.53	23.2	5.7/9.1	2.74	2.13/1.43	9.7
HH SR20	3.22	10.0	9.8/14.3	1.10	2.30/2.05	14.5
HH SR21	0.99	18.0	11.1/12.8	1.82	2.16/1.88	13.1
HH SR22	0.34	37.5	-7.4/8.3	2.27	2.40/2.34	9.0
HH SR23	0.74	17.4	22.4/18.3	1.86	2.27/1.55	22.6
HH SR24	0.45	24.6	26.7/20.9	3.16	1.57/2.62	27.0
HH SR25	0.28	34.3	-1.4/4.4	2.91	2.47/1.44	5.8
HH SR26	1.72	14.3	12.2/14.0	1.43	2.23/1.82	14.3
HH SR27	-0.03	-100.0	83.5/46.7	-0.00	3.98/1.57	83.6
HH SR28	0.08	121.7	-15.9/1.9	4.89	0.81/1.54	5.7
HH SR29	0.05	57.7	4.9/7.2	4.93	1.70/0.59	8.90
HH SR30	0.15	44.7	8.1/9.8	2.00	1.69/1.22	10.2
HH SR31	2.48	12.2	4.0/11.8	5.78	3.00/0.19	13.5
HH SR32	1.22	17.4	18.3/18.5	3.06	2.49/2.40	19.0

Table 6.1: Systematic errors for $ttW^{\pm}$ in the high-high regions.

For the ttZ, ttH, and qqWW backgrounds, we perform the same procedure as for the ttW; the one caveat is that for the qqWW, we perform the procedure on a privately-produced sample at LO with a different PDF set (MSTW 2008), and so we take a more

	c-s	acc, $H_T < 300$ GeV	acc, $H_T > 300$ GeV
ttW	13%	3%	8%
ttZ, ttH	11%	3%	8%
qqWW	30%		

Table 6.2: Systematic uncertainties for dominant rare backgrounds. The qqWW errors are not factorized and are presented as the total only.

conservative error approximation. The results are shown in table 6.2.

Other

Other rare processes are taken directly from simulation. We assume a 50% error on the total of these, identical to the run-1 prescription.

6.2 Fakes

The fake background is estimated from a data-driven method. We measure the fake rate in a fake-enriched control region where we can perform closure tests. Then we multiply every selected loose lepton in data by a factor of the fake rate, which provides the estimate fake background estimate. We then use an alternative "in-situ" measurement to cross-check this result and constrain the systematic uncertainty.

QCD FR

Derivation

We begin by defining a control-region that will be enriched in QCD events: such events will have many jets and therefore many non-prompt leptons, but no prompt leptons. Such events need to pass the following requirements:

- Pass a specific auxiliary trigger:

  - HLT_Mu8 or HLT_Mu17 (for muons in events with $H_T \geq 300$ GeV)
  - HLT_Mu8_TrkIsoVVL or HLT_Mu17_TrkIsoVVL (for muons in events with $H_T < 300$ GeV)
  - HLT_Ele12_CaloIdM_TrackIdM_PFJet30 (for electrons in events with $H_T \geq 300$ GeV)
  - HLT_Ele12_CaloIdL_TrackIdL_IsoVL_PFJet30 (for electrons in events with $H_T < 300$ GeV)

- exactly one lepton passing the loose ID requirements (the "fakeable object", or FO)
- at least one jet with ΔR(jet, FO) > 1
- MET < 20 GeV (to reject non-QCD events, particularly leptonic W-decays)
- $M_T < 20$ GeV

To remove the remaining prompt leptons, we use the Z-decay and W+Jets Simulation (expected to be the two leading backgrounds in this control region), normalize them in the region with MET > 20 GeV and $70 < M_T < 120$ GeV, and subtract the result from the fake rate. This procedure is called the electroweak subtraction.

We then simply take the number of leptons passing the tight ID requirement and divide it by the number of leptons passing the loose ID requirement – since our control region by construction contains a negligible amount of fakes, this ratio represents our fake rate. The fake rate is binned in p_T and $|\eta|$.

In order to reduce the non-universality of the fake rate as a function of the mother parton p_T, the p_T-parameterization of the fake rate is slightly modified. This "cone-correction"

to the p_T is defined in equation (6.3):

$$\begin{aligned} p_T &\to p_T \cdot (1 + \max(0, I_m - A)) \quad (p_T^{\text{rel}} > C) \\ pt &\to \max(p_T, p_T(\text{jet}) \cdot B) \qquad (\text{otherwise}) \end{aligned} \tag{6.3}$$

where A, B, C, and I_m (the mini-isolation) are defined in section 5.3. We shall show the efficacy of this reparameterization via a closure test at the end of this section (see figure 6.6).

Results

The derived fake rates are shown in figure 6.2 for the triggers corresponding to $H_T > 300$ GeV. The fake rates in the region corresponding to $H_T < 300$ GeV are similar and are not shown.

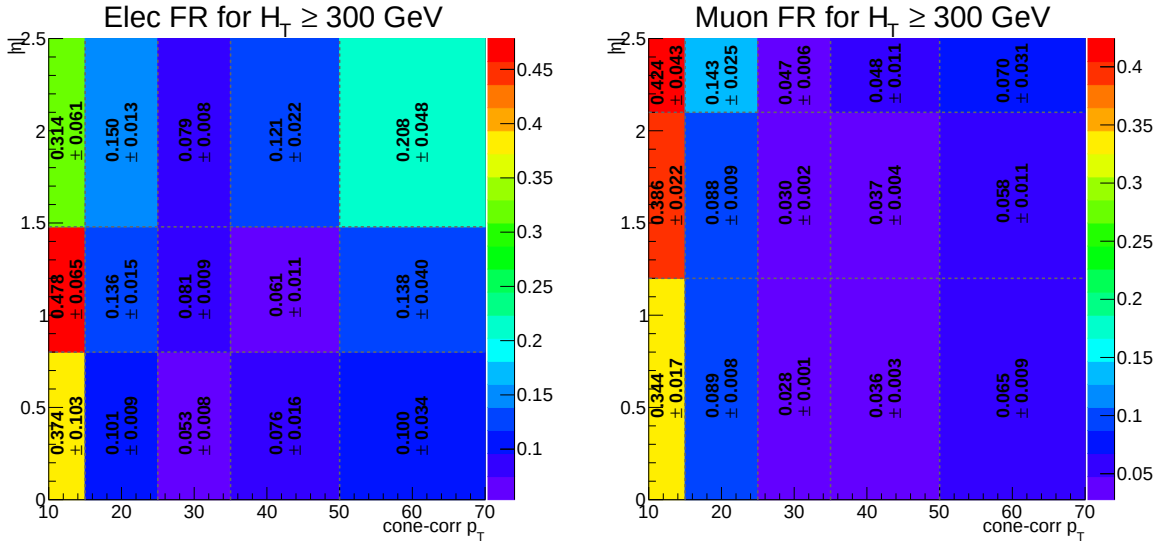

Figure 6.2: Fake rate in electrons and muons (for events with $H_T > 300$ GeV), parameterized by p_T and $|\eta|$.

We then use this to estimate our fake background by adding a factor of $\frac{FR}{1-FR}$ for each lepton in a selected tight-loose pair. The denominator is necessary because we do not add

any factor for selected tight-tight pairs (due to the potential for signal contamination).

in Situ Fake Rate

As a cross-check on the fake rate method, we have developed an alternative "*in situ*" method, which derives a fake rate using the events passing all analysis cuts except for the requirement that SIP3D ≥ 4: this provides a fake-enriched control region.[2] This rate is then applied to those events with the normal SIP3D cut to estimate the fake background.

Measurement

Like the QCD fake rate, the *in situ* fake rate is calculated as a ratio of tight leptons over loose leptons. The tight lepton definition is exactly the same as the analysis, except that the SIP3D cut is inverted. The loose lepton definition is identical to the tight lepton requirement except in the isolation: the MiniIso requirement inside equation (5.4) is loosened to $I_{\text{mini}} < 0.4$, and the p_T^{ratio} cut is relaxed to $\frac{1}{p_T^{\text{ratio}}} < \frac{1}{B} + I_{\text{mini}}$. Since the p_T^{ratio} variable is only loosely correlated with the SIP3D (see figure 6.3), the rate derived in this control region can be applied to the signal region.

The *in situ* fake rate is in principle measured in exactly the same region as the data except for the inverted SIP3D cut as described above. However, the statistics are so limited that we actually define the measurement region in a slightly broader way. We require:

- exactly two same-sign dileptons
- one lepton must pass the full tight ID selection; the second must pass all requirements except for the following:

[2]SIP3D was defined in section 5.3 as the significance of the quantity $\sqrt{dxy^2 + dz^2}$.

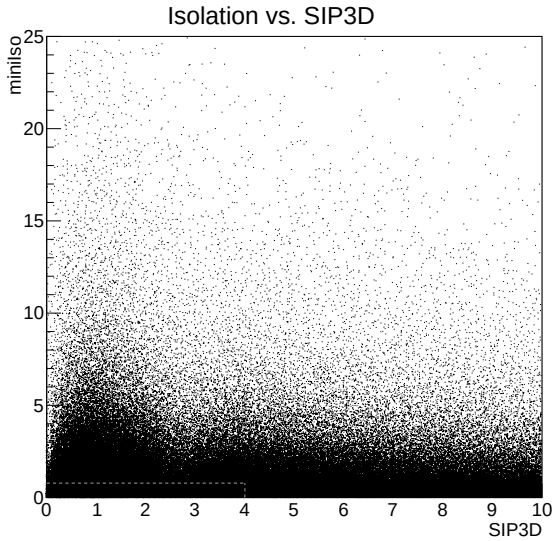

Figure 6.3: Plot showing only loose correlation between SIP3D and MiniIso. The dashes show the signal region.

  - SIP3D cut is inverted
  - dz cut is removed
  - the electron MVA thresholds are taken at the "loose" WP.

- No requirements are imposed on H_T, N_{jets}, and MET.
- For events with $H_T < 300$ GeV, the normal data sets and trigger requirements are imposed. For events with $H_T > 300$ GeV, the single electron and single muon datasets are used to select eμ events; the fake rate is then measured for the opposite-flavor lepton with no additional trigger requirement.

Results

The measured *in situ* fake rates are shown in figure 6.4. Due to the low statistics, we consider only one bin in $|\eta|$. Note that it is not necessary to derive separate *in situ* fake rates for the different triggers.

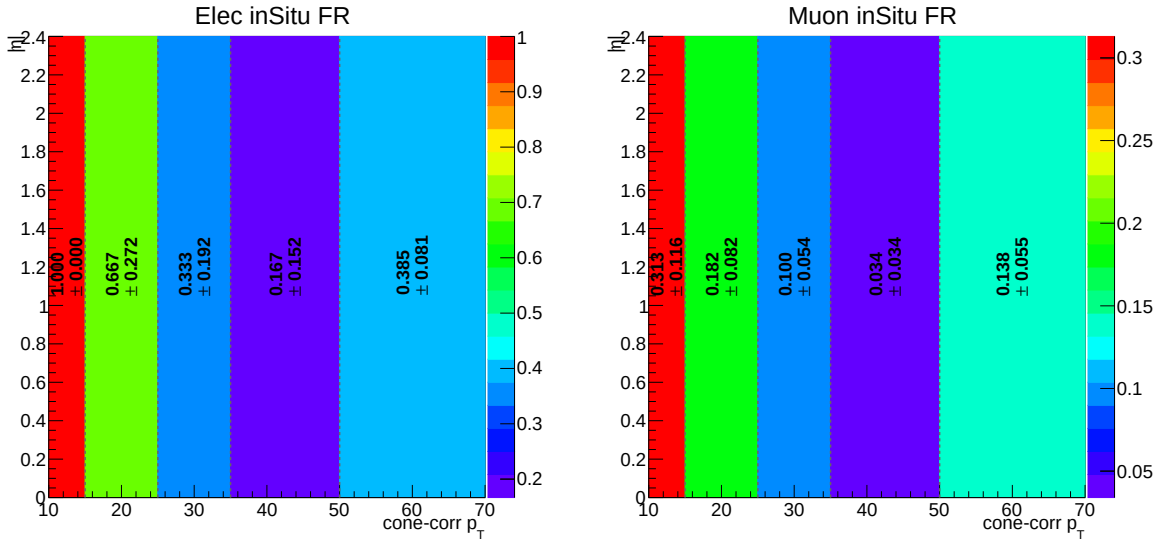

Figure 6.4: Fake rate from *in situ* method for electrons and muons, parameterized by cone-corr p_T and $|\eta|$.

Validation and Systematic

To validate our method for estimating the fake rate, we perform a closure test, applying our fake rate to the simulated samples most likely to yield fakes. Figure 6.5 shows our data-driven prediction in each signal region compared to the actual number of same-sign events in the simulataion that pass the selection criteria.[3]

[3]One technical note. The QCD fake rate was derived in simulation as it should be for a closure test in simulation; however the inSitu Fake Rate shown was derived in data. This allows us to see the statistical limitations of the method; however, we would expect the centeral values to be slightly closer to the observed if we had derived the rate in simulation.

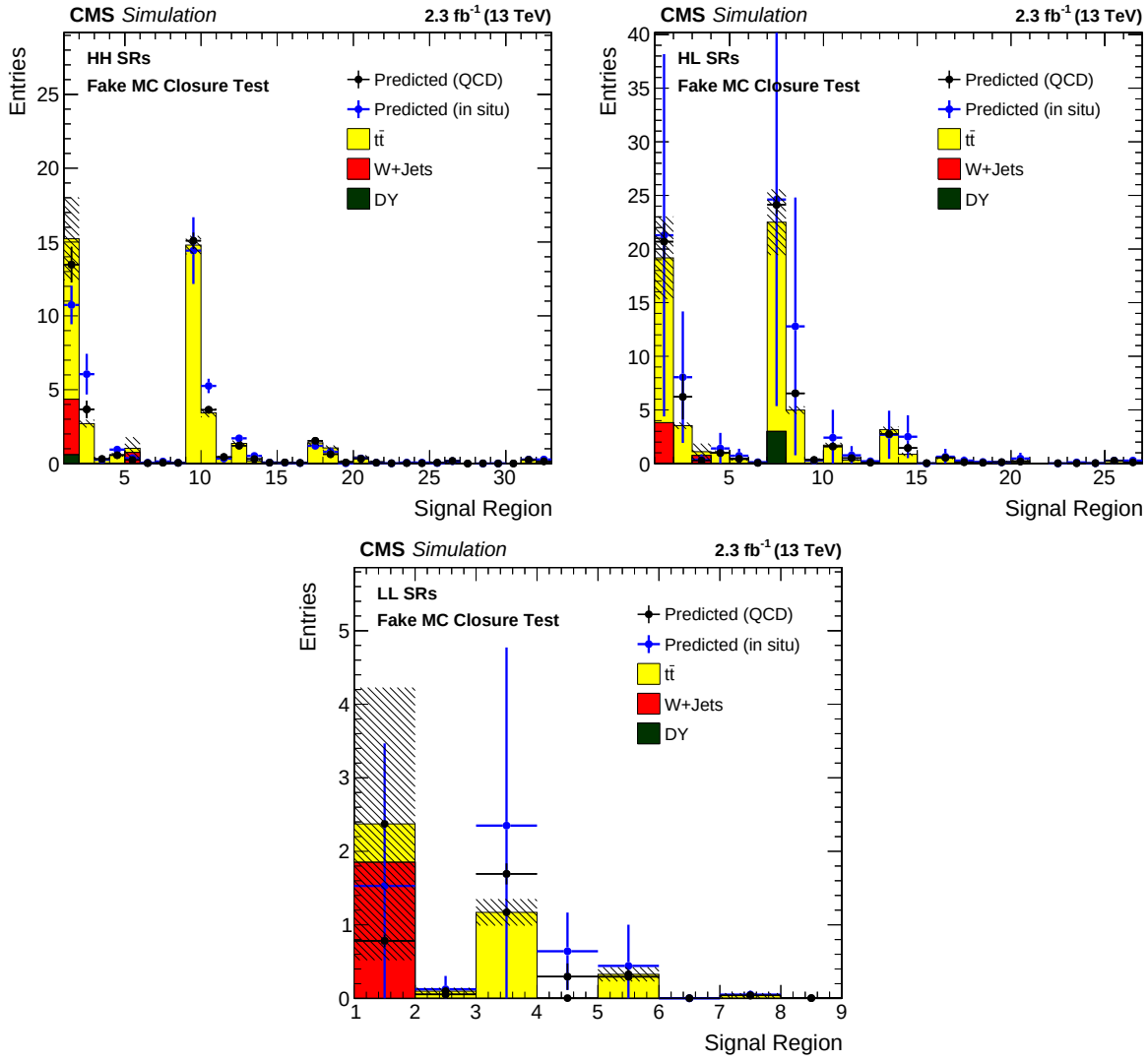

Figure 6.5: Fake rate closure results in electrons and muons in each SR, performed in simulation. Errors shown are statistical only, including the statistical error in the fake rate (for prediction).

Figure 6.5 shows that the QCD method works quite well, generally giving closure to within 20%. Further, the inSitu method also generally agrees, though it has considerable statistical error. We adopt a 30% systematic to cover the discrepencies between the three results.

We also take this opportunity to validate our claim that the cone-corrected p_T gives

better results: figure 6.6 shows the prediction (black) as well as the prediction without the cone-correction (blue); the cone-corrected result is clearly better by at least a factor of 2.

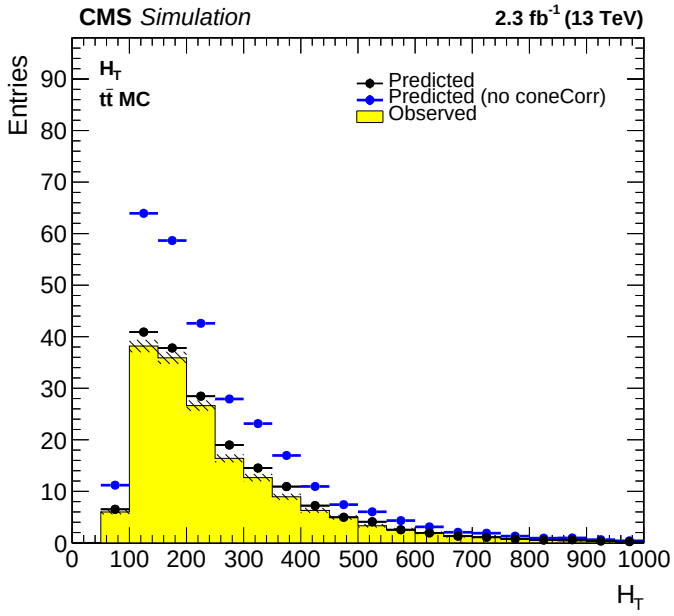

Figure 6.6: Closure results as a function of H_T with and without cone correction in the $t\bar{t}$ sample.

6.3 Flips

The charge misidentification background is also estimated via a data-driven method. First, the flip rate per lepton is calculated in simulation as a function of p_T and $|\eta|$. Second, the procedure is validated in a data control region in which the expected flip value can be determined, and a correction factor to the flip rate is calculated. Finally, every electron in a selected OS pair is multiplied by a factor of the flip rate; this provides the flip background estimate.

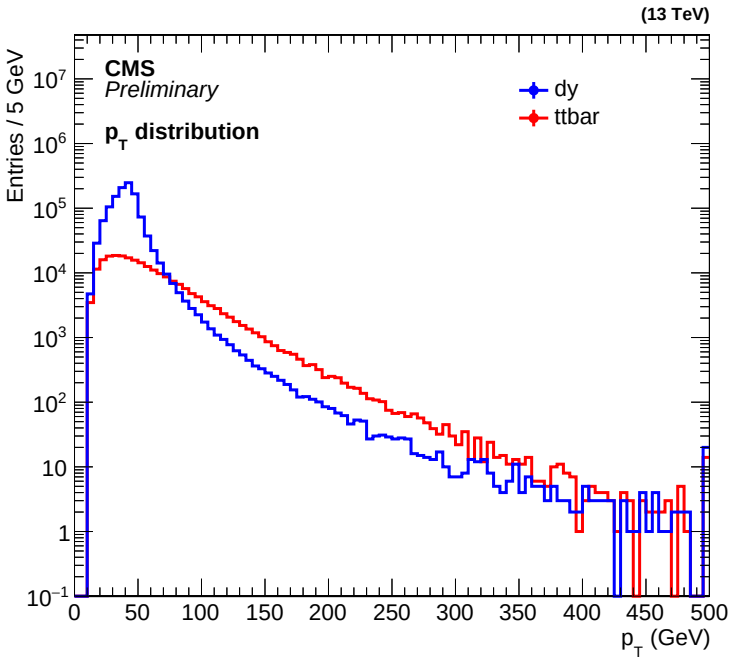

Figure 6.7: Number of events as a function of selected electron p_T (OS or SS) to be used for flip rate derivation.

Derivation

The $pp \to \ell^+\ell^-$ (Drell-Yan, or DY) sample obviously provides an excellent source of electrons, but the statistics are minimal at $p_T > M_Z$. For this reason, the rate is calculated in a "soup" of ttbar+DY simulation. The statistics as a function of p_T are shown in figure 6.7. As we showed in the commissioning plots, the lepton p_T is rarely greater than 300 GeV, so we are not concerned by our lack of statistics in that region. The flip rate derivation itself is performed on this simulation as a function of p_T and $|\eta|$, according to the definition:

$$\text{flip rate} = \frac{\text{selected reco electrons truth-matched to opposite-sign electron}}{\text{selected reco electrons truth-matched to electron}} \tag{6.4}$$

where truth-matching is defined in the same way as for the fake rate.

The resulting flip rate is given in figure 6.8:

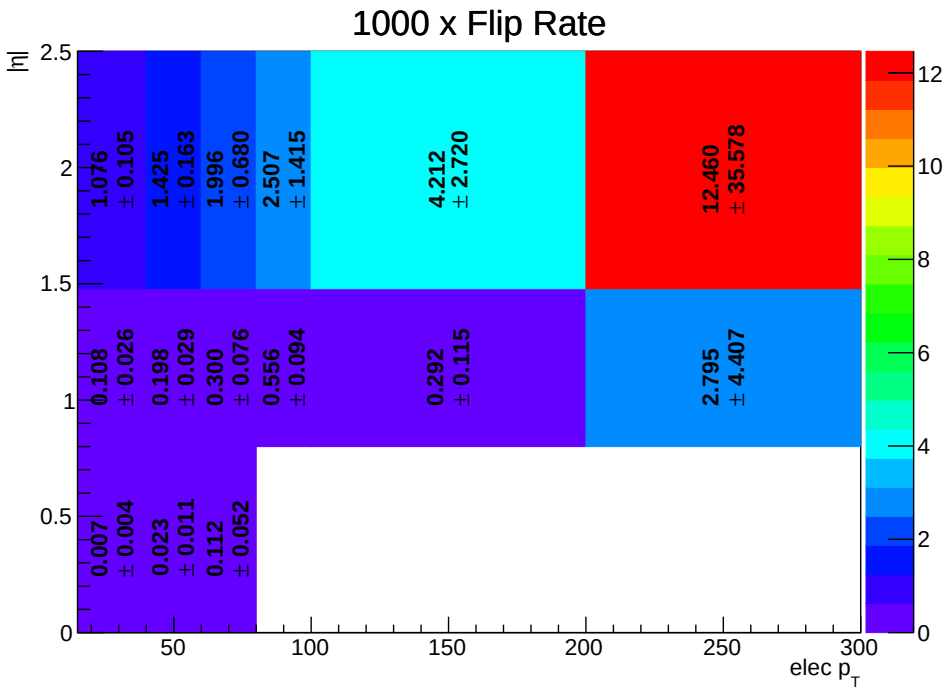

Figure 6.8: Number of expected charge flips per 1000 electrons.

As expected, the flip rate is higher at higher p_T and also at higher $|\eta|$, due to the lower material budget. The blank regions show a measured flip rate of zero. Due to the very small proportion of flips and the relatively limited statistics at a p_T far from $M_Z/2$, the statistical error is very significant in almost all bins, despite the considerable size of the simulated samples as presented in figure 6.7.

Validation

Now we validate our method in a control region which we define as follows:

- Two selected electrons passing our tight ID.

- MET < 50 GeV
- $80 \leq M_{\ell\ell} \leq 100$ GeV

This control region is designed to suppress signal and to target a composition of $Z \to \ell^+\ell^-$ events. In this region we expect no SS dileptons, so any observed SS dileptons are taken to be flips.

In this region, we can calculate the flip rate using three different methods:

- Observation: the number of selected SS pairs in data
- Prediction: the number of selected SS pairs in simulation
- Data-Driven prediction: for each selected OS pair, we add a factor of $\frac{FR}{1-FR}$ for each of the two electrons. The flip rate (FR) is determined from figure 6.8 and the denominator is necessary because we do not add any factor for selected SS events (as we hope that these are contaminated by signal!).

The results are shown in figure 6.9. From this plot, a scale factor of 1.35 is taken to the data-driven method so as to better align it to the observed data.

Application and Systematic

The flip rates of figure 6.8, multiplied by the scale factor of 1.35 found above, is then applied to the data samples in the same way as in the validation step above. The result is a predicted SS yield for flips.

For the systematic, we consider a closure test: in the same soup of DY+ttbar that we used to derive the sample, we estimate the number of flips using our method and

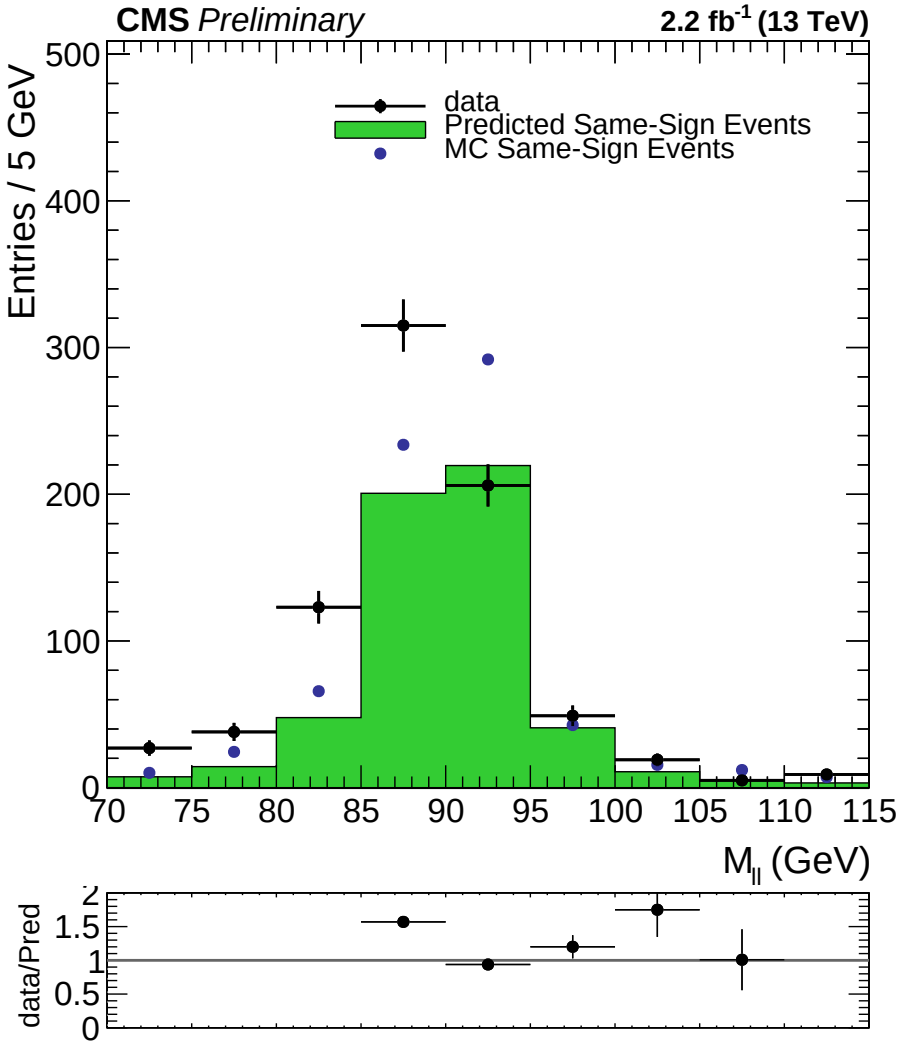

Figure 6.9: Simulation (dots) and data-driven (green) prediction of the number of charge flips in $Z \to e^+e^-$ data as a function of $M_{\ell\ell}$, compared with the data result.

compare this to the number of observed flips (neglecting the scale factor) in the same simulation sample. The non-closure is 26%, which we take as our systematic uncertainty.

6.4 Systematics

We have already discussed several systematics:

- The WZ background is assigned a 30% uncertainty.
- The data-driven flip calculation is assigned a 26% uncertainty.
- The data-driven fake calculation is assigned a 30% uncertainty.
- The ttW and ttZ/ttH backgrounds are assigned:
  - an uncertainty of 13% and 11% respectively, for the cross-sections (this includes the very small PDF and α_s contributions)
  - an uncertainty of 3% in the regions with $H_T < 300$ GeV and 8% elsewhere, for the acceptance. These are taken to be uncorrelated between low- and high-H_T regions but correlated between HH and HL regions.
- The qqWW background is assigned a 30% total uncertainty.
- The aggregate of other rare backgrounds is assigned an uncertainty of 50%.

Several additional uncertainties have not yet been discussed, and are listed below.

Luminosity

The uncertainty on the luminosity is assigned at 2.7%, per the relevant POG. This is applied to all backgrounds that are not taken from simulation (everything except fakes, flips, and WZ).

Pileup

The pile-up distribution in simulation is reweighted to match the measured pileup in data. The uncertainty on the cross-section caused by the uncertainty on this pileup procedure is assigned at 5%.

Jet Energy Scale

The p_T of each jet is varied up and down by 1σ, and the effects are propagated through to the nJets, nBtags, and H_T variables. The uncertainty on the jet energy scale is then assigned as the resulting change in the prediction for each SR. This varies in each SR, but is generally on the order of 2-8%.

Lepton SF Uncertainty

Based on the average deviation from unity in the scale factor, we take a 4% uncertainty in the lepton identification and a 2% uncertainty in the lepton trigger requirement.

Trigger Uncertainties

We take an additional 2% uncertainty for the regions with $H_T > 300$ since these triggers have an additional requirement on the H_T.

Beam Spot Uncertainty

A technical problem led to a small number of runs recording the incorrect beamspot; a 2% uncertainty in the $H_T < 300$ GeV regions has been recommended by the relevant POG to cover this effects.

B-tag SF

We vary the weight of events with b-tags up and down by 1σ and the change in each region as an error.

EWK Subtraction

We calculate the fake rate without performing the electroweak subtraction and generate the prediction with this alternative fake rate. The difference in the prediction is taken as an uncertainty.

Summary of Systematics

Source	type	Magnitude	Applied to
luminosity	flat	4.6%	everything except fakes, flips, and WZ
pileup	shape	5%	everything except fakes, flips, and WZ
JES	migr	2-8%	everything except fakes, flips, and WZ
B-tag SF	shape	5-10%	everything except fakes, flips, and WZ
Fakes	flat	30%	fakes
Cross-section	flat	13%	ttW
	flat	30%	qqWW
	flat	11%	ttZ, ttH
	regional	3%	ttW,ttZ,ttH
	regional	8%	ttW,ttZ,ttH
	flat	50%	other rares
Flips	flat	26%	flips
WZ SF norm & stat	flat	30%	WZ
Statistical	shape	1-30%	all
lepton id eff	flat	4%	everything except fakes, flips, and WZ
lepton trig eff	flat	2%	everything except fakes, flips, and WZ
trigger H_T	regional	2%	everything except fakes, flips, and WZ
EWK subtraction	shape	1-20%	fakes

Table 6.3: Table of Systematics. "Flat" systematics are applied uniformly, "shape" systematics are determined bin-by-bin, "migr" are determined bin-by-bin and including event migration, and "regional" systematics have flat systematics applied differently in different regions, as explained above.

Systematics for Signal Samples

The signal samples (used for exclusion plots) receive the systematics for statistics, luminosity, pileup, jes, b-tag SF, beam-spot correction, trigger H_T, and lepton trigger eff in the same way as the backgrounds. The fastsim samples receive the same lepton efficiency uncertainty as the backgrounds: additionally, they receive a factor for the fullsim-fastsim difference with is taken at 8%, 15%, and 20% for the HH, HL, and LL regions, respectively. Similarly, the lepton trigger efficiency is supplemented by a 5% factor for the fullsim-fastsim difference in the triggers.

When the invariant p_T of the gluino pair is high, we assign a large uncertainty to the fastsim yield due to known issues in the software (following the recommendation of the SUSY PAG). This is taken to be 15% for $M_{\tilde{g}\tilde{g}} > 400$ and 30% for $M_{\tilde{g}\tilde{g}} > 600$.

In the same way as the ttW/ttZ/ttH backgrounds, the scale error is determined from the simulation software. Unlike in the backgrounds, we do not round off similar signal regions; we simply apply the scale error as calculated in each SR. The α_s and PDF errors are taken to be negligible.

Chapter 7

Results and Interpretations

We have now completed describing the method for taking the data and calculating the expected backgrounds, so we are ready to look at the results!

7.1 Results

The yields for each SR are shown in figures 7.1 and 7.2. Further, tables 7.1, 7.2, and 7.3 show the same results numerically, broken down only into the rare/fake/flip categories.

Clearly there is no statistically-significant excess. The largest excesses are in SR10HH and SR8HL; while it is a bit curious that these correspond to the same area of phase space, the two $\sim 1\sigma$ results are certainly not enough to claim any significant deviation from the background.

One final observation we can make is to cross-check our predictions from the data-driven methods against those from straight simulation. Comparing the HH SR predictions from figure 7.1 with those in figure 7.3 shows that the two methods give similar predictions.

SR	Rare	Fake	Flip	Total	Data
1	19.06 ± 3.51	14.40 ± 5.76	2.08 ± 0.62	35.53 ± 6.77	39
2	8.27 ± 1.32	3.64 ± 1.46	0.70 ± 0.21	12.61 ± 1.98	16
3	0.90 ± 0.13	0.00 ± 0.00	0.14 ± 0.04	1.04 ± 0.14	2
4	1.10 ± 0.21	0.29 ± 0.12	0.05 ± 0.02	1.44 ± 0.24	0
5	1.73 ± 0.27	0.49 ± 0.20	0.02 ± 0.01	2.25 ± 0.34	4
6	0.10 ± 0.01	0.00 ± 0.00	0.00 ± 0.00	0.10 ± 0.01	0
7	0.47 ± 0.07	0.33 ± 0.13	0.10 ± 0.03	0.89 ± 0.15	0
8	0.14 ± 0.02	0.00 ± 0.00	0.00 ± 0.00	0.14 ± 0.02	0
9	6.31 ± 0.76	13.13 ± 5.25	1.96 ± 0.59	21.40 ± 5.34	26
10	4.51 ± 0.55	3.27 ± 1.31	0.67 ± 0.20	8.45 ± 1.43	15
11	0.66 ± 0.09	1.27 ± 0.51	0.15 ± 0.04	2.08 ± 0.52	3
12	1.52 ± 0.20	0.62 ± 0.25	0.06 ± 0.02	2.20 ± 0.32	1
13	0.77 ± 0.09	0.26 ± 0.11	0.04 ± 0.01	1.07 ± 0.14	3
14	0.13 ± 0.02	0.12 ± 0.05	0.00 ± 0.00	0.26 ± 0.05	0
15	0.28 ± 0.04	0.00 ± 0.00	0.08 ± 0.03	0.36 ± 0.05	0
16	0.17 ± 0.02	0.00 ± 0.00	0.01 ± 0.00	0.18 ± 0.02	0
17	2.29 ± 0.31	1.58 ± 0.63	0.94 ± 0.28	4.81 ± 0.76	4
18	2.02 ± 0.27	0.63 ± 0.25	0.20 ± 0.06	2.84 ± 0.37	1
19	0.38 ± 0.06	0.00 ± 0.00	0.07 ± 0.02	0.46 ± 0.06	0
20	1.11 ± 0.15	0.28 ± 0.11	0.03 ± 0.01	1.42 ± 0.18	3
21	0.32 ± 0.05	0.05 ± 0.02	0.01 ± 0.00	0.39 ± 0.05	0
22	0.07 ± 0.01	0.00 ± 0.00	0.00 ± 0.00	0.08 ± 0.01	0
23	0.15 ± 0.02	0.00 ± 0.00	0.03 ± 0.01	0.17 ± 0.02	0
24	0.13 ± 0.02	0.00 ± 0.00	0.00 ± 0.00	0.14 ± 0.02	1
25	0.17 ± 0.02	0.00 ± 0.00	0.04 ± 0.01	0.20 ± 0.03	0
26	0.36 ± 0.06	0.05 ± 0.02	0.02 ± 0.01	0.44 ± 0.07	1
27	0.00 ± 0.00	0.00 ± 0.00	0.00 ± 0.00	0.00 ± 0.00	0
28	0.02 ± 0.01	0.00 ± 0.00	0.00 ± 0.00	0.03 ± 0.01	0
29	0.01 ± 0.00	0.00 ± 0.00	0.00 ± 0.00	0.02 ± 0.00	0
30	0.02 ± 0.01	0.00 ± 0.00	0.00 ± 0.00	0.02 ± 0.01	0
31	1.65 ± 0.26	0.17 ± 0.07	0.05 ± 0.01	1.87 ± 0.27	1
32	0.71 ± 0.09	0.10 ± 0.04	0.02 ± 0.01	0.83 ± 0.10	1

Table 7.1: Results for HH SRs

SR	Rare	Fake	Flip	Total	Data
1	12.88 ± 2.74	30.15 ± 9.04	0.71 ± 0.21	43.74 ± 9.45	40
2	2.83 ± 0.49	5.39 ± 1.62	0.17 ± 0.05	8.39 ± 1.69	9
3	0.34 ± 0.07	0.26 ± 0.08	0.01 ± 0.00	0.61 ± 0.10	0
4	0.40 ± 0.05	0.60 ± 0.18	0.01 ± 0.00	1.01 ± 0.19	3
5	0.79 ± 0.14	0.58 ± 0.18	0.01 ± 0.00	1.39 ± 0.23	0
6	0.08 ± 0.02	0.00 ± 0.00	0.00 ± 0.00	0.08 ± 0.02	0
7	3.68 ± 0.58	21.86 ± 6.56	0.71 ± 0.21	26.25 ± 6.59	24
8	1.72 ± 0.21	3.57 ± 1.07	0.08 ± 0.02	5.38 ± 1.09	13
9	0.08 ± 0.01	0.25 ± 0.08	0.01 ± 0.00	0.34 ± 0.08	0
10	0.70 ± 0.10	1.65 ± 0.49	0.01 ± 0.00	2.36 ± 0.50	2
11	0.25 ± 0.03	1.01 ± 0.30	0.01 ± 0.00	1.27 ± 0.31	0
12	0.03 ± 0.01	0.02 ± 0.01	0.00 ± 0.00	0.05 ± 0.01	0
13	1.26 ± 0.17	2.59 ± 0.78	0.36 ± 0.11	4.21 ± 0.80	3
14	0.93 ± 0.13	1.07 ± 0.32	0.06 ± 0.02	2.06 ± 0.35	1
15	0.05 ± 0.01	0.00 ± 0.00	0.01 ± 0.00	0.05 ± 0.01	0
16	0.37 ± 0.05	0.02 ± 0.01	0.01 ± 0.00	0.40 ± 0.05	1
17	0.09 ± 0.01	0.19 ± 0.06	0.00 ± 0.00	0.28 ± 0.06	0
18	0.09 ± 0.02	0.00 ± 0.00	0.00 ± 0.00	0.09 ± 0.02	0
19	0.10 ± 0.01	0.00 ± 0.00	0.00 ± 0.00	0.11 ± 0.01	0
20	0.15 ± 0.03	0.00 ± 0.00	0.01 ± 0.00	0.16 ± 0.03	0
21	0.00 ± 0.00	0.00 ± 0.00	0.00 ± 0.00	0.00 ± 0.00	0
22	0.04 ± 0.01	0.00 ± 0.00	0.00 ± 0.00	0.04 ± 0.01	0
23	0.03 ± 0.00	0.00 ± 0.00	0.00 ± 0.00	0.03 ± 0.00	0
24	0.05 ± 0.01	0.16 ± 0.05	0.00 ± 0.00	0.21 ± 0.05	0
25	0.85 ± 0.23	0.35 ± 0.10	0.02 ± 0.01	1.22 ± 0.25	1
26	0.13 ± 0.02	0.11 ± 0.03	0.00 ± 0.00	0.24 ± 0.04	0

Table 7.2: Results for HL SRs

	Rare	Fake	Flip	Total	Data
1	0.25 ± 0.04	1.74 ± 0.52	0.00 ± 0.00	1.99 ± 0.52	1
2	0.13 ± 0.02	0.00 ± 0.00	0.01 ± 0.00	0.14 ± 0.02	0
3	0.13 ± 0.02	3.25 ± 0.98	0.01 ± 0.00	3.39 ± 0.98	2
4	0.04 ± 0.01	0.00 ± 0.00	0.00 ± 0.00	0.04 ± 0.01	0
5	0.14 ± 0.02	0.00 ± 0.00	0.00 ± 0.00	0.14 ± 0.02	0
6	0.02 ± 0.00	0.00 ± 0.00	0.00 ± 0.00	0.02 ± 0.00	0
7	0.03 ± 0.00	0.00 ± 0.00	0.00 ± 0.00	0.03 ± 0.00	0
8	0.00 ± 0.00	0.10 ± 0.03	0.00 ± 0.00	0.10 ± 0.03	0

Table 7.3: Results for LL SRs

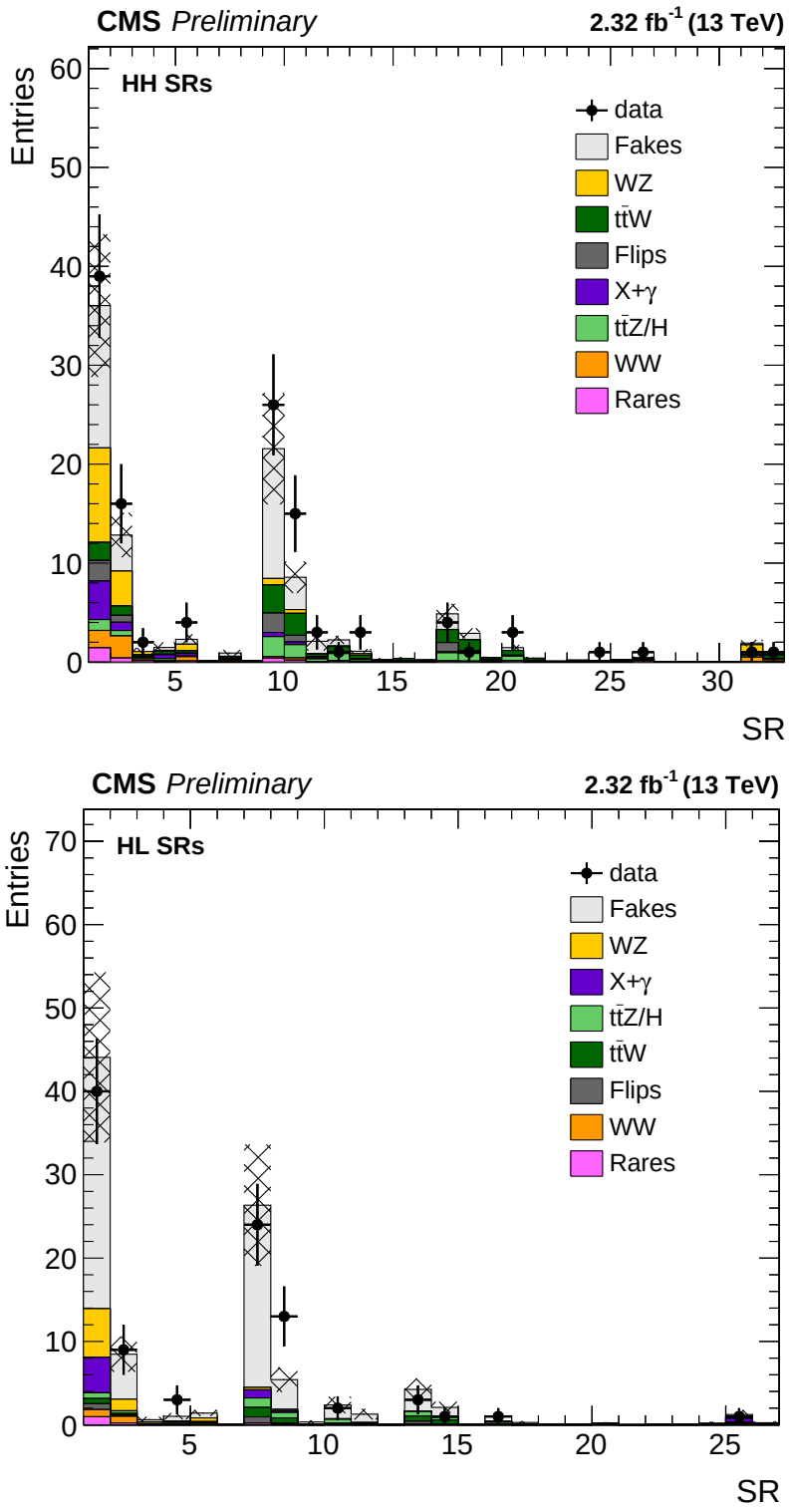

Figure 7.1: Prediction and data results in HH and HL SRs.

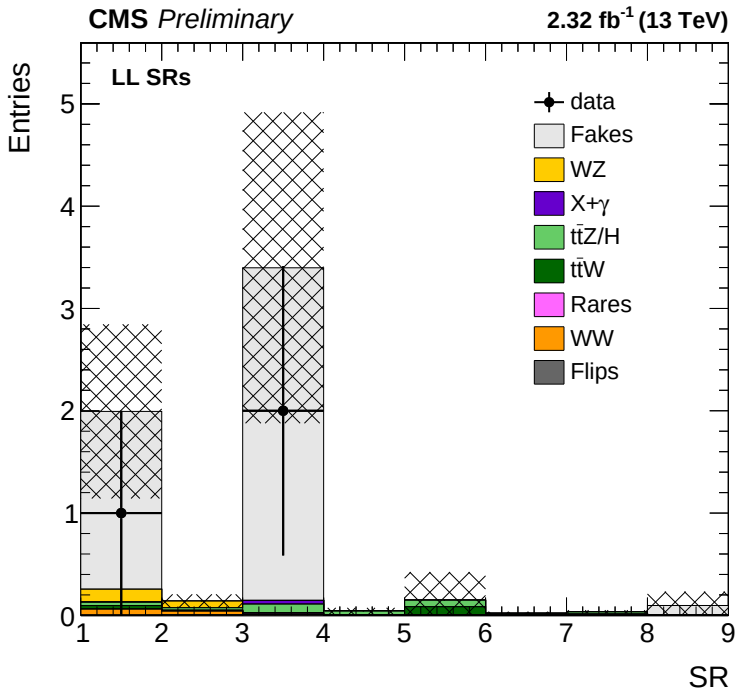

Figure 7.2: Prediction and data results in LL SRs.

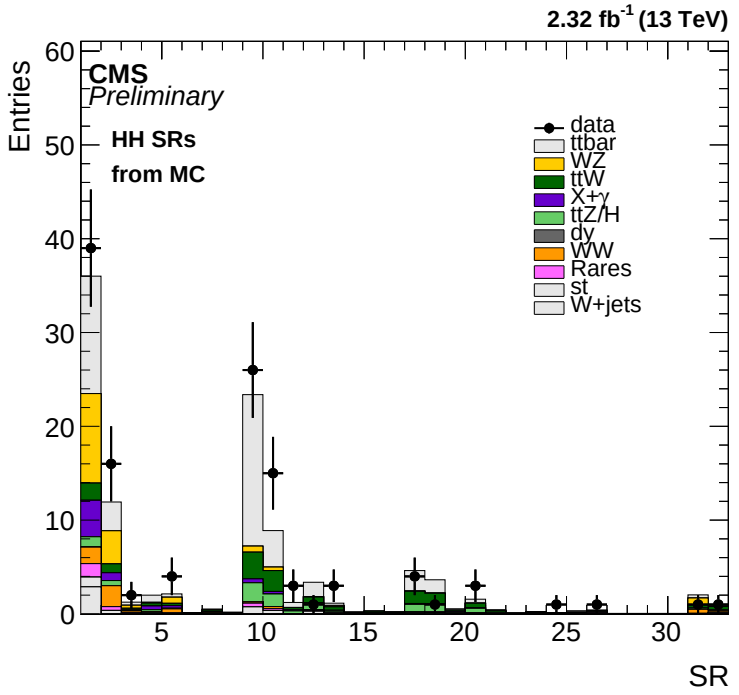

Figure 7.3: Prediction and data results in HH SRs without data-driven methods. Errors on simulation are omitted.

7.2 SUSY Interpretations

Having failed to find an excess, we now proceed to set limits on the allowed masses in the SMS models introduced earlier using standard statistical methods. All limits are at 95% confidence.

As an example of the sensitivity, consider the T1tttt model introduced previously. In table 4.6, we mentioned that the 8 TeV analysis was able to exclude the T1tttt model for gluino masses below 1050 GeV in the region with large mass splitting. Figure 7.5 shows the exclusion plot for the this analysis; the new limit in the region with large mass splitting is approximately 1300 GeV.

T1tttt

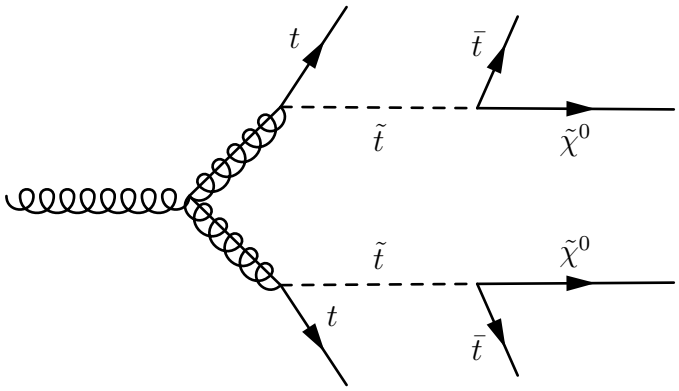

Figure 7.4: T1tttt Model. Note that the stop is off-shell, so it is a three-body decay.

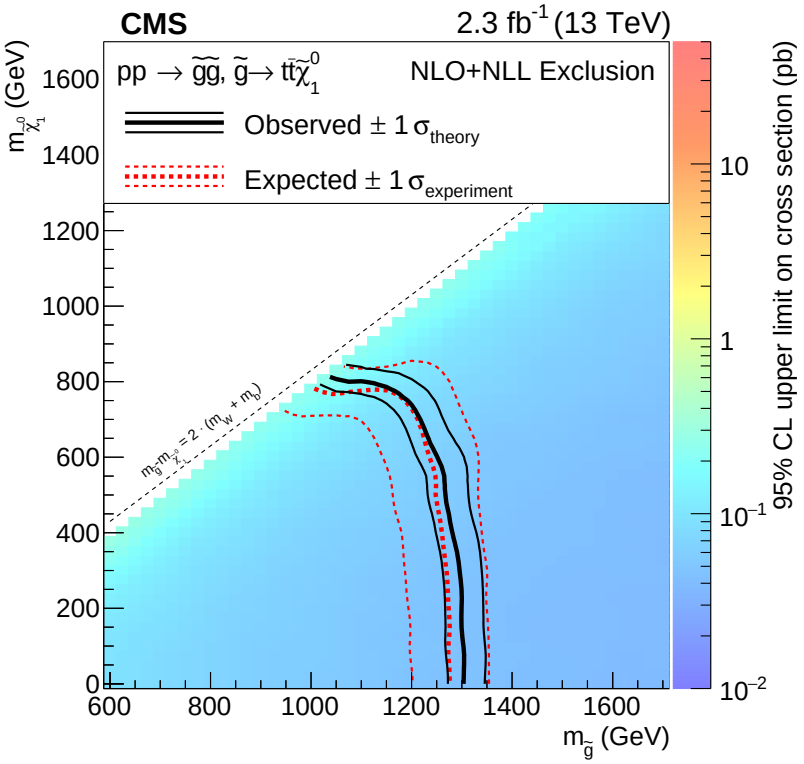

Figure 7.5: Exclusion Plot for T1tttt model.

T1ttbb

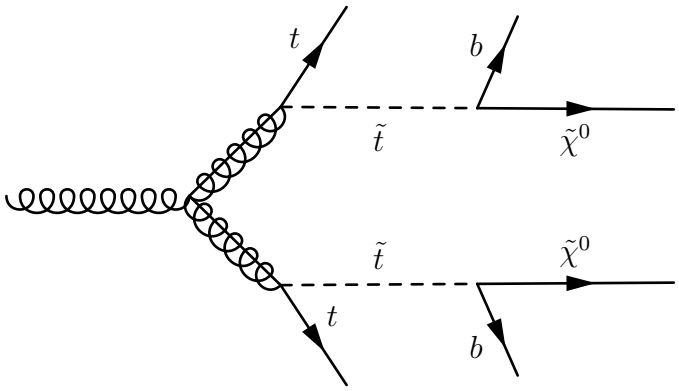

Figure 7.6: T1ttbb Model. Note that the stop is off-shell, so it is a three-body decay.

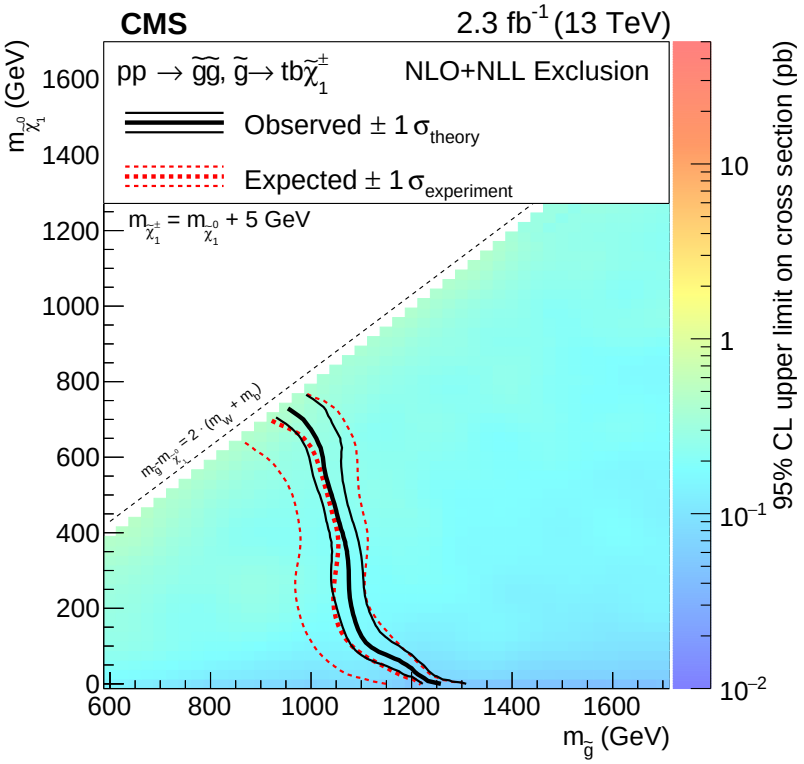

Figure 7.7: Exclusion Plot for T1ttbb model.

T5tttt

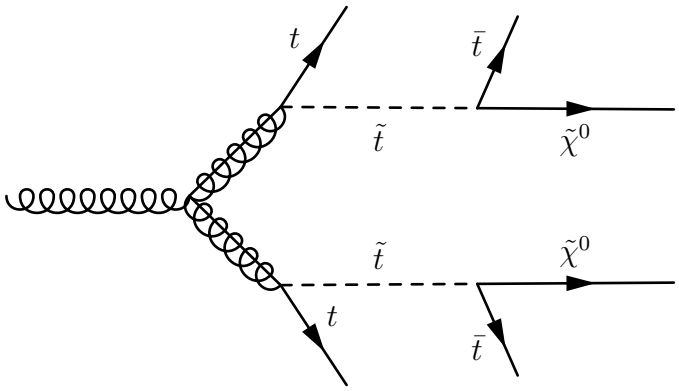

Figure 7.8: T5tttt Model. Note that the stop is on-shell, so it is a sequence of two-body decays.

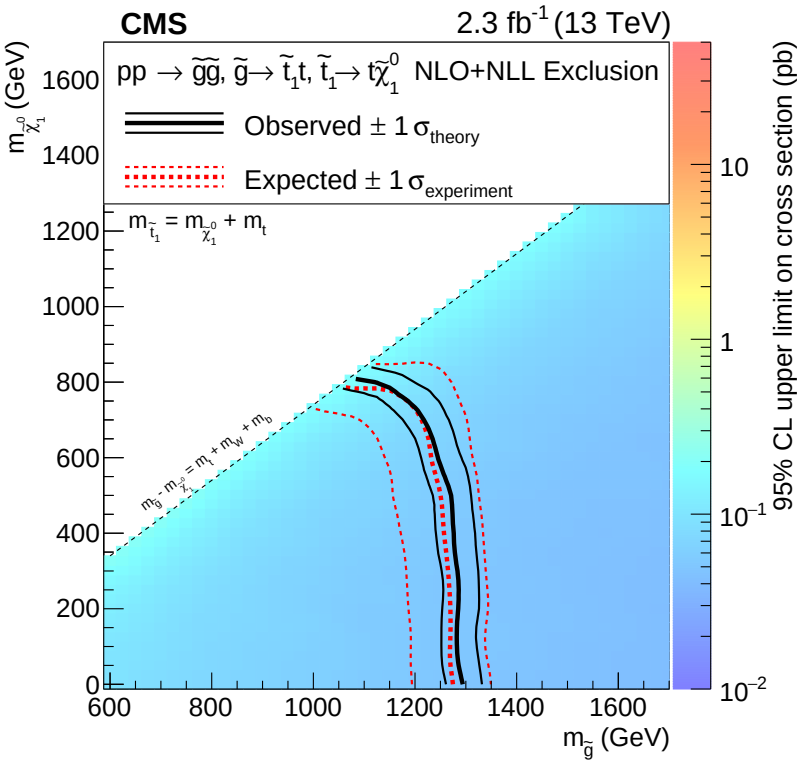

Figure 7.9: Exclusion Plot for T5tttt model with the LSP mass lower than the stop mass by 175 GeV.

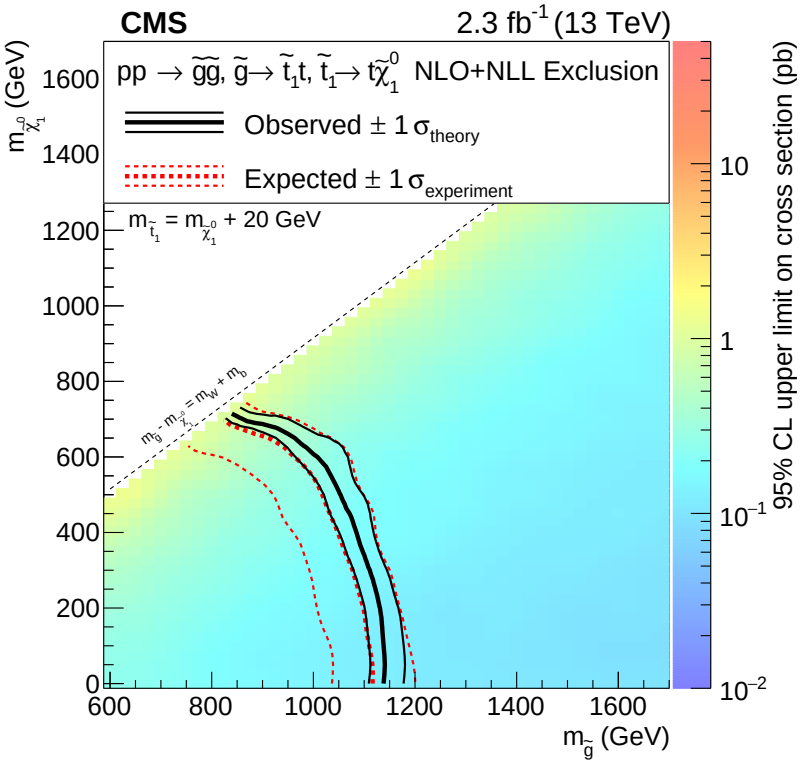

Figure 7.10: Exclusion Plot for T5tttt model with the LSP mass lower than the stop mass by 20 GeV.

T5ttcc

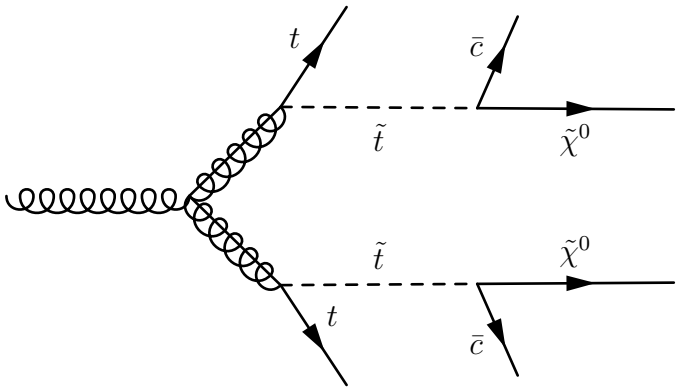

Figure 7.11: T5ttcc Model

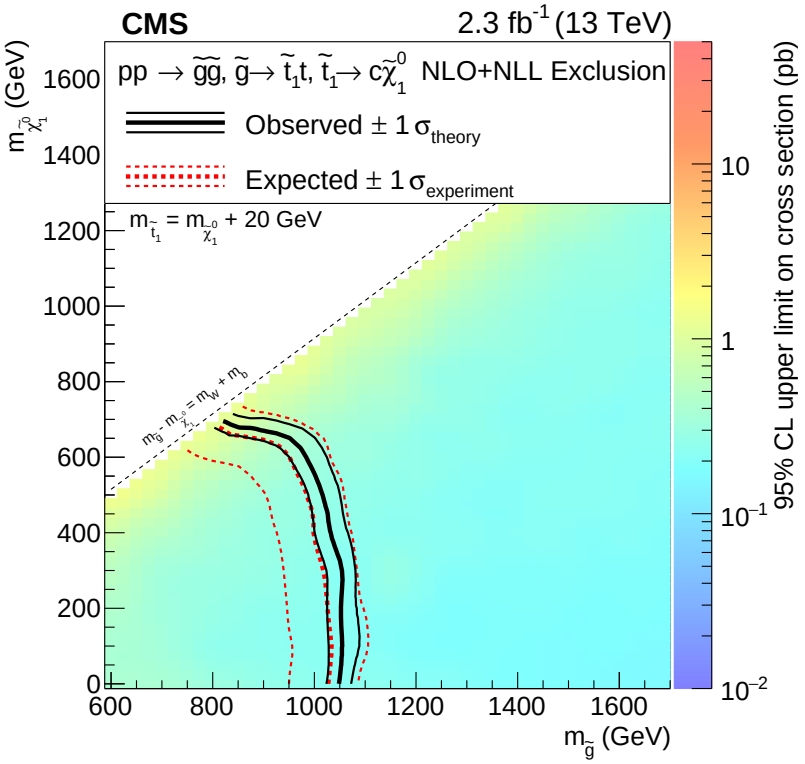

Figure 7.12: Exclusion Plot for T5ttcc model.

T5qqqqWW

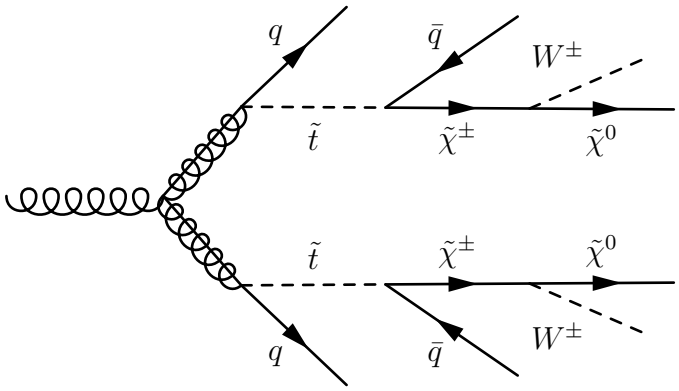

Figure 7.13: T5qqqqWW Model. Note that the final top quarks (designated as t^*) are off-shell and will immediately decay to bW.

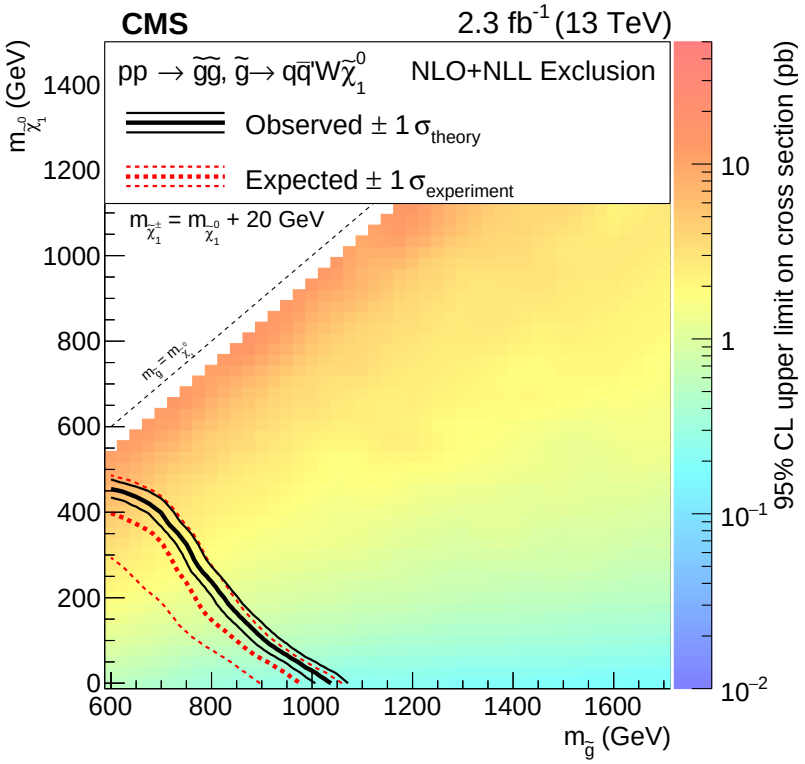

Figure 7.14: Exclusion Plot for T5qqqqWW model with chargino mass set to 20 GeV above LSP mass.

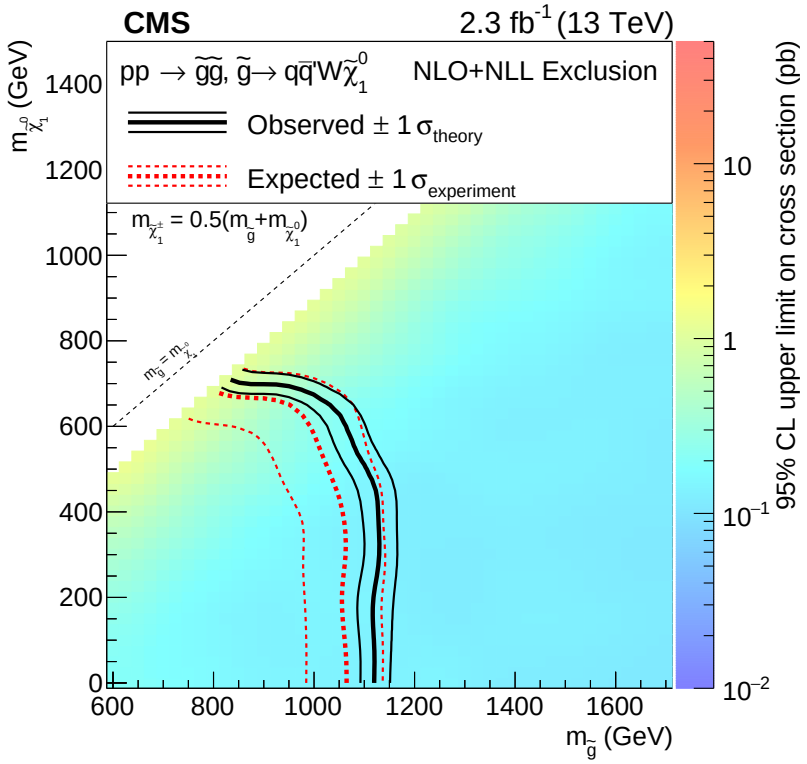

Figure 7.15: Exclusion Plot for T5qqqqWW model with chargino mass set to the average of the gluino and LSP mass.

T6ttWW

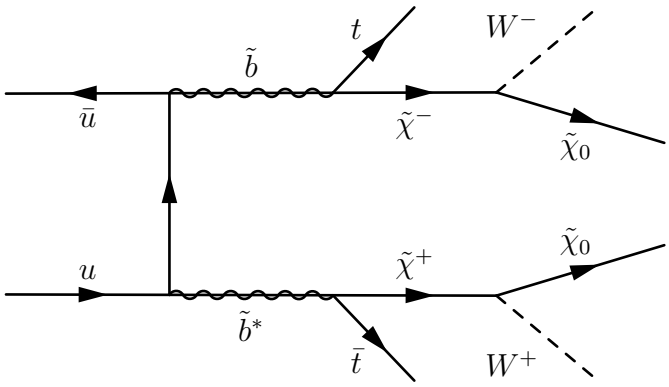

Figure 7.16: T6ttWW model.

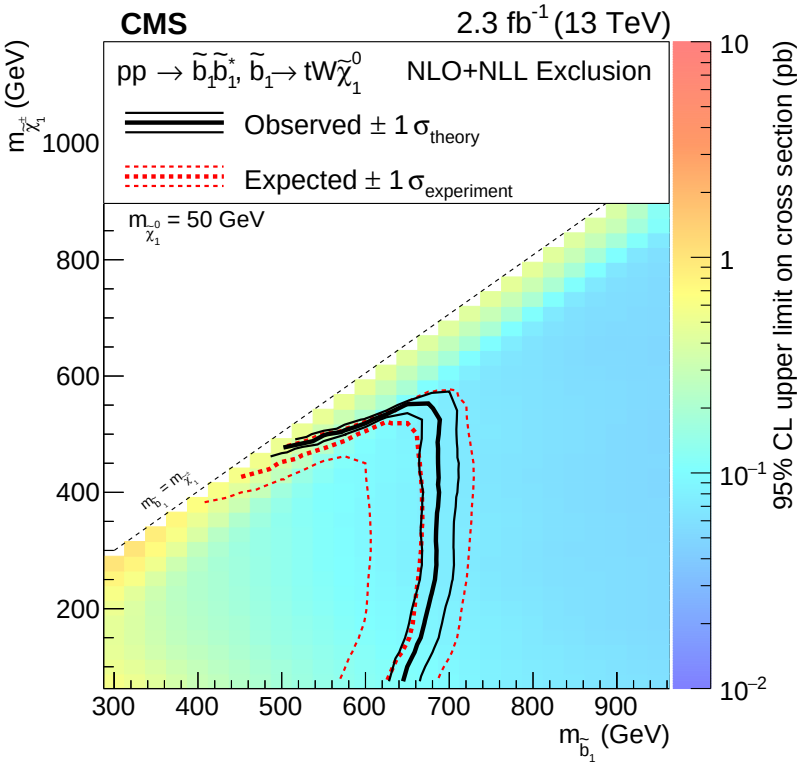

Figure 7.17: Exclusion Plot for T6ttWW model.

Chapter 8

Summary and Conclusions

We have performed a search for any signal beyond the Standard Model with a signature of two leptons of the same electrical charge. This is the fourth generation of such an analysis, this time at the unprecedented energy of $\sqrt{s} = 13$ TeV and with several technical improvements over the previous iterations. We found no statistically-significant excess above the Standard Model background. We have therefore set exclusion limits on several simplified SUSY models; these limits are the most competitive limits set by a same-sign search to date.

We noted previously that the SUSY hypothesis becomes much less convincing when the lightest squark mass is more than "a few" TeV, as such models could not solve the naturalness problem. The exclusion limits for many simplified SUSY models – including most of those studied in this analysis – are rapidly approaching this limit. The LHC will resume taking data in Summer 2016, and it is expected that this analysis will yield either an excess or a still more significant set of exclusions with the increased luminosity.

Despite the negative result in the same-sign channel (and other channels not discussed

here), there is one possible bright spot from the 2015 dataset: both CMS and ATLAS have reported an excess in the diphoton channel around $M_{\gamma\gamma} \sim 750$ GeV with a confidence of $2 - 3\sigma$ each (see [64], [65]). Although these excesses are considerably lower after the look-elsewhere effect is accounted for, it is possible that we are on the cusp of a discovery.[1]

[1] I will, however, go on record as being pessimistic about the endurance of this diphoton excess.

Bibliography

Chapter 1

Derivation of the Standard Model

[1] Griffiths, David. *Introduction to Elementary Particles*. Weinheim: Wiley-VCH Verlag GmbH & Co., 2008.

[2] Halzen, Francis and Martin, Alan. *Quarks & Leptons: An Introductory Course in Modern Particle Physics*. Upper Saddle Ridge, NJ: John Wiley & Sons, Inc., 1984.

[3] Srednicki, Mark. *Quantum Field Theory*. Cambridge: Cambridge University Press, 2007.

Tests of the SM

[4] Hanneke, D. et al. *Cavity Control of a single-electron quantum cyclotron: Measuring the electron magnetic moment*. Phys. Rev. A **83**, 052122 (2011).

[5] The ALEPH, DELPHI, L3, OPAL collaborations, the LEP Electroweak Working Group. *Electroweak Measurements in Electron-Positron Collisions at W-Boson-Pair Energies at LEP*. Phys. Rept. 532 2013 119.

[6] Bevan, A.J. *et al. The Physics of the B Factories*. Eur. JPhys. J. C74 (2014) 3026.

[7] CMS Collaboration. *Physics Results SMP*. August 2015, accessed 17 December 2015. https://twiki.cern.ch/twiki/bin/view/CMSPublic/PhysicsResultsSMP

Chapter 2

Problems with the SM

[8] Freese, Katherine. *Review of Observational Evidence for Dark Matter in the Universe and in upcoming searches for Dark Stars.* Conference Proceeding for "Dark Matter and Dark Energy", Lyon, France, July 2008.

[9] Albada, T.S. *et al. Distribution of Dark Matter in the Spiral Galaxy NGC 3198.* The Astrophysical Journal 295:305-313, August 1985.

[10] Peter, Annika H.G. *Dark Matter: A Brief Review.* Proceedings from the Frank N. Bash Symposium, 2011.

[11] Garrett, Katherine and Duda, Gintaras. *Dark Matter: A Primer.* Adv.Astron.2011:968283, 2011.

[12] Mannel, Thomas. *Theory and Phenomenology of CP Violation.* Talk at BEACH, July 2006. https://indico.cern.ch/event/427023/session/6/contribution/43/attachments/912026/1288208/Lancester-Mannel-Proc.pdf

[13] K.A. Olive et al. (PDG), Chin. Phys. C38, 090001 (2014) (http://pdg.lbl.gov, Revoiew on the Muon Anomalous Magnetic Moment.)

[14] BaBaR Collaboration. *Evidence for an Excess of* $\bar{B} \to D^{(*)}\tau^-\bar{\nu}_\tau$ *Decays.* PRL 109, 101802 (2012).

[15] Frenk, Carlos and White, Simon D.M. *Dark Matter and Cosmic Structure.* Annalen der Physik (2012).

[16] Dar, Arnon. *Dark Matter and Big Bang Nucleosynthesis.* Astrophysics J. 449 (1995) 550.

Supersymmetry

[17] Martin, Stephen. *A Supersymmetry Primer.* http://arxiv.org/pdf/hep-ph/9709356v6.pdf

[18] CMS Collaboration. *Interpretation of searches for supersymmetry with simplified models.* Phys. Rev. D 88 (2013) 052017.

[19] Papucci, Michele *et al. Natural SUSY Endures.* JHEP 09 (2012) 035.

Alternatives to Supersymmetry

[20] Appelquist, Thomas *et al.* *Bounds on Universal Extra Dimensions.* Phys.Rev.D64:035002, 2001.

[21] Siringo, Fabio. *A Truly Minimal Left-Right Symmetric Extension of the Standard Model.* Eur.Phys.J.C32:555, 2004.

[22] Gunion, J.F. *et al. Higgs triplets in the Standard Model.* Phys.Rev.D42:5, 1990.

[23] Arkani-Hamed, N. *et al. The Littlest Higgs.* JHEP 0207:034 (2002).

[24] Lane, Kenneth. *Two Lectures on Technicolor.* FERMILAB-PUB-02/040-T.

Searches for New Physics

[25] US Department of Energy. *Cosmic Frontier Experiments.* 2015, retrieved 17 December 2015. http://science.energy.gov/hep/research/cosmic-frontier/experiments/

[26] US Department of Energy. *Intensity Frontier Experiments.* 2015, retrieved 17 December 2015. http://science.energy.gov/hep/research/intensity-frontier/experiments/

[27] US Department of Energy. *Energy Frontier Experiments.* 2015, retrieved 17 December 2015. http://science.energy.gov/hep/research/energy-frontier/experiments/

[28] CERN. *Experiments.* 2015, retrieved 17 December 2015. http://home.cern/about/experiments

Chapter 3

Description of the LHC

[29] Holmes, Jeff *et al. Transverse Beam Optics, Part 1.* January 2009, retrieved 17 December 2015. https://uspas.fnal.gov/materials/09VU/Lecture6.pdf

[30] Zimmermann, Frank. *LHC: The Machine.* 26 July 2012, retrieved 17 December 2015. http://www-conf.slac.stanford.edu/ssi/2012/Presentations/Zimmermann.pdf

[31] CERN. Engineering. 2015, retrieved 17 December 2015. http://home.web.cern.ch/about/engineering

[32] Burkhardt, Helmut. *High-Luminosity LHC*. 14th LNF Mini-Workshop Series. https://agenda.infn.it/getFile.py/access?contribId=1&resId=0&materialId=slides&confId=6985

[33] Ball, Richard *et al*. *Neural Network Parton Distribution Functions*. NNPDF Collaboration. https://nnpdf.hepforge.org/.

[34] Deile, M, for the TOTEM collaboration. *First Measurements of Proton-Proton elastic scattering and total cross-section at the LHC by totem*, available at http://totem.web.cern.ch/Totem/docs/eds11deile.pdf (retrieved 20 January 2016).

[35] ATLAS Collaboration. *Measurement of the Inelastic Proton-Proton Cross Section at $\sqrt{s}$ = 13 TeV with the ATLAS Detector at the LHC*. 2015, available at https://cds.cern.ch/record/2045064/files/ATLAS-CONF-2015-038.pdf (retrieved 20 January 2016).

Description of CMS

[36] K. Nakamura et al.(PDG), JP G 37, 075021 (2010) and 2011 partial update for the 2012 edition (pdg.lbl.gov, chapter 28)

[37] CERN. *Detector Overview*. 2011, accessed 18 December 2015. http://cms.web.cern.ch/news/detector-overview

[38] CMS Collaboration. *The CMS experiment at the CERN LHC*. J. Instrum. 3 (2008) S08004.

[39] Bloch, I. *The CMS Muon System*. June 2008, accessed 18 December 2015. http://vmsstreamer1.fnal.gov/VMS_Site_03/Lectures/CMS/presentations/080618Bloch.pdf

[40] CMS Collaboration. *The performance of the CMS muon detector in proton-proton collisions at sqrt(s) = 7 TeV at the LHC*. JINST 8 (2013) P11002.

[41] Gutsche, Oliver. *Computing Support Facilities*. Fermilab. https://indico.fnal.gov/getFile.py/access?contribId=33&sessionId=7&resId=0&materialId=2&confId=6589

Early Results

[42] CMS Collaboration. *CMS Supersymmetry Physics Results*. 2015, accessed 18 December 2015. https://twiki.cern.ch/twiki/bin/view/CMSPublic/PhysicsResultsSUS

[43] CMS Collaboration. *Observation of a new boson with mass near 125 GeV in pp collisions at sqrt(s) = 7 and 8 TeV*. JHEP 06 (2013) 081.

[44] CMS Collaboration. *Measurement of the X(3872) production cross-section via decays to J/psi pi pi in pp collisions at sqrt(s)=7 TeV*. JHEP 04 (2013) 154.

[45] CMS Collaboration. *Evidence for Collective Multiparticle Correlations in p-Pb Collisions*. PRL 115, 012301 (2015).

Chapter 4

Searches with SS Dileptons

[46] Borschensky, Christoph *et al. Squark and gluino production cross sections in pp collisions at* $\sqrt{s}$ *= 13, 14, 33, and 100 TeV*. CERN-PH-TH-2014-137.

[47] S. Heinemeyer *et al. Handbook of LHC Higgs cross sections: 3. Higgs Properties.* CERN-2013-004. 29 July 2013. http://arxiv.org/pdf/1307.1347v2.pdf.

[48] J. Beringer *et al.* (Particle Data Group). PR D86, 010001 (2012) (URL: http://pdg.lbl.gov).

[49] K.A. Olive et al. (PDG), Chin. Phys. C38, 090001 (2014) (http://pdg.lbl.gov, chapter 32)

8 TeV SS Search

[50] CMS Collaboration. *Search for new physics in events with same-sign dileptons and jets in pp collisions at sqrt(s) = 8 TeV*. JHEP 01 (2014) 163.

[51] CMS Collaboration. Internal Document AN-2013/120.

[52] Barnett, R. *et al. Discovering supersymmetry with like-sign dileptons*. Phys.Lett. B315 (1993) 349-354.

[53] CDF Collaboration. *Inclusive search for new physics with like-sign dilepton events in* $\bar{p}p$ *collisions at* $\sqrt{s} = 1.96$*-TeV*. Phys.Rev.Lett. 98 (2007) 221803.

Chapters 4-8 – 13 TeV SS Search

[54] CMS Collaboration. *The anti-k_t jet clustering algorithm*. JHEP 0804:063, 2008.

[55] CMS Collaboration. *Identification of b-quark jets with the CMS experiment*. JINST 8 (2013) P04013.

[56] CMS Collaboration. *Performance of the CMS missing transverse energy reconstruction in pp data at sqrt(s) = 8 TeV*. JINST 10 (2015) P02006.

[57] CMS Collaboration. *Determination of Jet Energy Calibration and Transverse Momentum Resolution in CMS*. JINST 6 (2011) 11022.

[58] CMS Collaboration. *Search for SUSY in same-sign dilepton events at 13 TeV*. Analysis Note (in production) 15/031.

[59] CMS Collaboration. SUS Data/MC Lepton Scale Factors. https://twiki.cern.ch/twiki/bin/view/CMS/SUSLeptonSF (internal twiki).

[60] CMS Collaboration. Efficiencies of the lepton selection and triggers in $\bar{t}t$ and signal samples. https://indico.cern.ch/event/459796/contribution/3/attachments/1181560/1710852/leptonandtriggeffcy.pdf (internal slideshow).

[61] CMS Collaboration. *Performance of b-tagging Algorithms in 25 ns Data at 13 TeV*. Analysis Note 15/282.

[62] Alekhin, Sergey *et al. The PDF4LHC Working Group Interim Report*. arXiv:1101.0536.

[63] NNPDF Collaboration. *Parton Distributions for the LHC Run II*. JHEP 04 (2015) 040.

[64] CMS Collaboration. *Search for New Physics in high mass diphoton events in proton-proton collisions at* $\sqrt{s} = 13$ *TeV*. CMS PAS EXO-15-004.

[65] ATLAS Collaboration. *Search for resonances decaying to photon pairs in* 3.2 fb^{-1} *of pp collisions at* $\sqrt{s} = 13$ *TeV with the ATLAS detector*. ATLAS-CONF-2015-081.